NORTHWESTERN UNIVERSITY

Photoinduced Energy, Charge, and Spin Transfer in Organic Molecular Materials

A DISSERTATION

SUBMITTED TO THE GRADUATE SCHOOL

IN PARTIAL FULFILLMENT OF THE REQUIREMENTS

for the degree

DOCTOR OF PHILOSOPHY

Field of Chemistry

By

Zachary Esburn Xavier Dance

EVANSTON, IL

December 2007

ABSTRACT

Photoinduced Energy, Charge, and Spin Transfer in Organic Molecular Materials

Zachary Esburn Xavier Dance

This thesis presents results and analysis on a series of donor-bridge-acceptor (D-B-A) charge transfer systems in which we use time-resolved spectroscopy and magnetic resonance techniques to study the relationship of molecular structure to energy, charge, and spin transfer dynamics. We find that the sequence of events following the initial charge separation within these systems indicates the considerable level of structurally and energetically dependent mechanistic complexity responsible for these processes in organic materials.

We first examine a series of D-B-A molecules where a phenothiazine donor and a perylene-3,4:9,10-bis(dicarboximide) acceptor are linked by an oligo-p-phenylene$_n$ bridge, n = 1-5. Photoexcitation results in rapid electron transfer to produce $^1(D^{+\bullet}\text{-B-A}^{-\bullet})$. Above 150 K, when n = 2-5, the radical pair intersystem crossing mechanism produces spin-correlated radical ion pairs. Charge recombination in the radical pairs generates D-B-^{3*}A, which exhibits a spin-polarized signal similar to that observed in photosynthetic reaction-center proteins and some biomimetic systems. At low temperatures and/or at shorter donor-acceptor distances, D-B-^{3*}A is also formed from a competitive spin-orbit intersystem crossing (SO-ISC) mechanism.

The second series also employs an oligo-p-phenylene$_n$ bridge, n = 1-4, to link a 3,5-dimethyl-4-(9-anthracenyl)julolidine donor to a naphthalene-1,8:4,5-bis(dicarboximide) acceptor. Similarly, charge separation produces a singlet radical pair state which undergoes intersystem crossing to the triplet radical pair state. Our results show directly that charge

recombination of the radical pair initially produces a spin-polarized triplet state, D-B-^{3*}A, that can *only* be produced by hole transfer involving the HOMOs of the D-B-A system. After the initial formation of D-B-^{3*}A, triplet-triplet energy transfer occurs to produce ^{3*}D-B-A. We also find that a SO-ISC mechanism becomes prevalent at shorter bridge lengths.

Lastly, we examine the unusual SO-ISC mechanism that is operative in both of the D-B-A systems above. We use simple D-A systems linked by a single bond to compare how changes in a single degree of freedom affect photophysical behavior. Our studies show that the unusual SO-ISC mechanism depends on the degree of charge separation, the relative orientation of the orbitals involved in the charge transfer, and the magnitude of the electronic coupling between the donor and acceptor.

ACKNOWLEDGEMENTS

Wilson has helped me out on numerous occasions, thank you. I thank all of the synthetic people in the lab Emilie Giacobbe, Sarah Mickley, Annie Butler, and Joseph Bullock for making me things. I thank the newest students, Mike Colvin, Sheela Ramanan, and Vickie Gunderson, for reminding me to be excited even when I feel a bit burned out. I have enjoyed working Mike Colvin in the EPR laboratory over the past year.

I thank my committee members, Profs. Tamar Seideman and George Schatz, who have given me constructive comments and general direction on numerous occasions. In addition, they have been exceptionally patient when it comes to scheduling my various requirements.

I also thank my Uncle Charlie who has been a constant source of positive encouragement. You are a wonderful friend, and I always feel better after a conversation with you.

I want to thank my family (Mom, Dad, Gabe, Caleb, and Cate) for their love and support. Mom and Dad, you are people who I respect and love immensely, and I always appreciate your guidance. Mom, your encouragement and constant care have made even the hardest things bearable . Dad, you are a source of wisdom and entertainment, and I know when I need to talk, you will always listen. Gabe, I truly admire your ambition and drive. I respect that you are forthright and honest with me even when we disagree. Caleb, I always enjoy talking about anything and everything in your company. Your tolerance and acceptance of different views is a remarkable trait. Cate, you are funny and passionate. I thank you for always reminding me of the importance of friendship. Each of you impresses me and I am a better person because of all of you are part of my life.

Lastly, I thank Smruti Amin. You have been a wonderful companion during this entire experience. In your company I have learned my strengths and weaknesses. I have learned how

to really work for something and how to be focused. I respect your unwavering loyalty and heartfelt generosity. Your constant support was critical and I am indebted to you. We have shared many, many laughs together, and I look forward to many more.

Dedication

For Smruti and the Dance Zak-Dance Family

Table of Contents

List of Figures

List of Tables

Chapter 1

Introduction

If John Donne were a chemist, he would certainly agree that no molecule is an island. Indeed, it is safe to say that we may only gain a greater understanding of the world we live in by interacting with it. As such, a physical chemist has much to be excited about, for certainly measurement is a form of interaction. However measurement alone is not inherently useful. We must additionally incorporate analysis to understand what we have measured and whether it was even what we intended to measure. Only through thoughtful repetition of these steps do we arrive at a greater understanding of both the topic of interest and its significance in the larger context.

Very generally, in this work the topics of interest are energy, charge, and spin transfer processes in organic materials. What then is the larger context? The answer, though suitably vague, is rather straightforward – The context is only limited by our imagination and creativity. In other words, these processes arise in some form or another in essentially every aspect of our lives. From biological systems to technological systems and much in between, these fundamental processes are at work.

It is perhaps more useful to reduce the scope and briefly look at several specific topics that are more immediately approachable. For example, fossil fuels are the primary source of usable energy in modern life. However, a variety of concerns have arisen regarding their long-term impact on the environment.[1, 2] These questions have motivated a quest for alternative, renewable energy sources. Solar energy is certainly one of the viable options because it has the potential to deliver enormous quantities of clean energy.[2, 3] Thus, systems to capture, convert, and store this solar energy are required. The caveat is that current inorganic photovoltaic materials are prohibitively expensive for practical widespread adoption of the technology. An attractive approach to this problem is to design next-generation photovoltaic systems that use

organic molecular materials instead. Organic photovoltaics have the potential for comparatively inexpensive manufacturing costs.[4] At the core of their operation, photovoltaic devices employ energy, change, and spin transport. Developing a fundamental understanding of these processes in chemical systems is important for designing systems capable of sustainable energy utilization.

Another example involves using organic molecular materials to replace or augment conventional silicon integrated circuits, i.e., molecular electronics. Aviram and Ratner[5] initiated a new direction for molecular design with their description of single molecule rectification in 1974. In this vision, molecules perform basic tasks such as switching, logic, information storage, and signal transport.[6-8] However, the potential for molecular electronics to yield practical and reliable devices has yet to be realized, in large part because the underlying processes involved are still being investigated.

In both of these examples, very tangible, real-world applications depend critically on learning, understanding, and applying basic physical processes. Hence, it is clear that controlling energy, charge, and spin transfer through molecular components is essential in designing and implementing functional organic materials for use in a variety of relevant technological contexts. Organic materials allow extreme modulation of their physical properties arising from the rich synthetic flexibility of organic chemistry and the capacity for complex behavior. As such, these materials are particularly attractive to areas including (but not limited to) solar energy conversion or storage and molecular electronics. Furthermore, from a fundamental scientific view, they offer fascinating systems with unique new phenomena.

This thesis presents results and analysis of a series of donor-bridge-acceptor (D-B-A) charge transfer systems in which we use time-resolved spectroscopy to study the relationship of molecular structure to energy, charge, and spin transfer dynamics. Magnetic resonance techniques are particularly well suited for investigating these systems because the charge and spin transfer events involve paramagnetic states. Furthermore, with sufficient time resolution it is possible to observe the non-Boltzmann population of the magnetic sublevels during a physical process. This so-called electron spin polarization (ESP) is highly sensitive to electronic and structural parameters and is indicative of the mechanisms involved. The primary methods of characterization used in this work can be broadly classified as time-resolved electron paramagnetic resonance (TREPR) spectroscopy techniques.[9-15] In actuality, there are many different TREPR spectroscopy techniques, two of which were primarily employed in these studies. The first, Transient Continuous Wave (TCW) EPR, is useful for examining the behavior of radical pair states. It has a ~30-40 ns time resolution and is a relatively simple experiment to perform. However, as implied by the name, the magnetic states are probed with continuous microwave irradiation. This creates the situation where one must use enough microwave power to observe the signals, but as the power is increased, there is a significant impact on the evolution of the signal decay. This can severely complicate the analysis, but it is usually possible to find a suitable balance. The second technique, electron spin echo (ESE) EPR, is more closely related to conventional FT-NMR techniques. Because ESE is a pulsed technique, the measured signal is an impulse response and is similar to a free induction decay. Specifically, following the microwave pulses, the spin system evolves freely and pure kinetic information is collected directly. Moreover, the signal to noise ratio is generally higher for ESE than TCW. However, as a result of changes in the longitudinal and transverse relaxation times, ESE displays much stronger

temperature dependence than TCW. In general, these techniques are complementary and both provide useful physical information.

The studies presented in this thesis show that photoexcitation of the D-B-A systems results in charge separation to produce a singlet radical ion pair (^{1}RP). The sequence of events following the initial charge separation is found to be dependent on temperature and donor and acceptor energy levels. In addition, the magnitude of the electronic coupling and relative orientation between the donor and acceptor play critical roles in the behavior of the systems.

In Chapter 2 we examine a series of donor-bridge-acceptor (D-B-A) systems, where D = phenothiazine (PTZ), B= p-phenylene (Ph$_n$), n = 1-5, and A = perylene-3,4:9,10-bis(dicarboximide) (PDI), Figure 2.1. Photoexcitation of these systems results in rapid electron transfer to produce ^{1}(PTZ$^{+\bullet}$-Ph$_n$-PDI$^{\bullet}$). The TREPR studies of the photogenerated radical pairs show that above 150 K, when n = 2-5, the radical pair intersystem crossing mechanism (RP-ISC) produces spin-correlated radical ion pairs. This mechanism results from the different local magnetic environments of the radical cation and radical anion and is discussed in depth in the chapter introduction. The spin-correlated radical pairs have electron spin polarization patterns indicating that the spin-spin exchange interaction in the radical ion pair is positive, $2J > 0$, and is temperature dependent. This temperature dependence is most likely due to structural changes of the p-phenylene bridge. Charge recombination in the radical pairs generates PTZ-Ph$_n$-^{3*}PDI, which exhibits a spin-polarized signal similar to that observed in photosynthetic reaction-center proteins and some biomimetic systems. At temperatures below 150 K and/or at shorter donor-acceptor distances, e.g. when n = 1, PTZ-Ph$_n$-^{3*}PDI is also formed from a competitive spin-orbit intersystem crossing (SO-ISC) mechanism that is a result of direct charge recombination: ^{1}(PTZ$^{+\bullet}$-Ph$_n$-PDI$^{\bullet}$) $\rightarrow$ PTZ-Ph$_n$-^{3*}PDI. It is found that this SO-ISC mechanism requires the

initial RP intermediate and depends strongly on the orientation of the molecular orbitals involved in the charge recombination as well as the magnitude of *2J*. It is discussed in further detail in Chapter 4.

PDI   Ph$_n$ PTZ
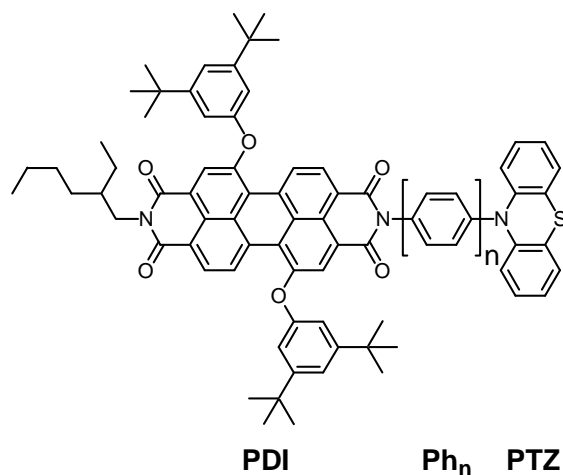
Figure 1.1. Chemical structure of PTZ-Ph$_n$-PDI, where $n = 1$ for compound **1**, $n = 2$ for compound **2**, etc.

As has been discussed, understanding how the electronic structures of electron donor-bridge-acceptor (D-B-A) molecules influence the lifetimes of photogenerated radical ion pairs (D$^{+\bullet}$-B-A$^{\bullet}$) is critical to designing and developing molecular systems for solar energy conversion. A general question that often arises is whether the HOMOs or LUMOs of D, B, and A within D$^{+\bullet}$-B-A$^{\bullet}$ are primarily involved in charge recombination. In Chapter 3, we develop a new series of D-B-A molecules consisting of the same oligo-*p*-phenylene bridge, where $n = 1$-4, connecting a 3,5-dimethyl-4-(9-anthracenyl)julolidine (DMJ-An) electron donor to a naphthalene-1,8:4,5-bis(dicarboximide) (NI) acceptor to give DMJ-An-Ph$_n$-NI, Figure 1.2. The photoexcited charge transfer state of DMJ-An acts as a high-potential photoreductant to rapidly and nearly quantitatively transfer an electron across the Ph$_n$ bridge to produce a spin-coherent singlet RP ^{1}(DMJ$^{+\bullet}$-An-Ph$_n$-NI$^{\bullet}$). Subsequent radical pair intersystem crossing yields ^{3}(DMJ$^{+\bullet}$-An-Ph$_n$-NI$^{\bullet}$). Charge recombination within the triplet RP then gives the neutral triplet state.

TREPR spectroscopy shows directly that charge recombination of the RP initially produces a spin-polarized triplet state, DMJ-An-Ph$_n$-^{3*}NI, that can *only* be produced by hole transfer involving the HOMOs of D, B, and A within the D-B-A system. After the initial formation of DMJ-An-Ph$_n$-^{3*}NI, triplet-triplet energy transfer occurs to produce DMJ-^{3*}An-Ph$_n$-NI with rate constants that show distance dependence consistent with those determined for charge separation and recombination. Just as in the previous chapter, a SO-ISC mechanism becomes prevalent at shorter bridge lengths.
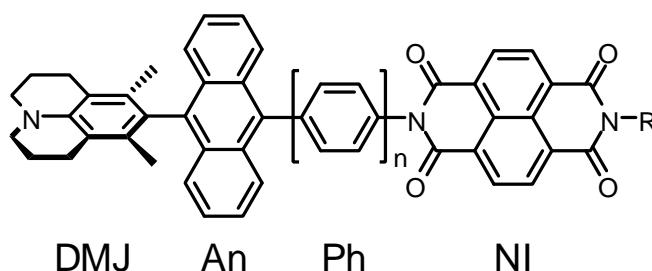
DMJ   An   Ph   NI

Figure 1.2. Chemical structure of DMJ-An-Ph$_n$-NI where $n = 1$ for compound 1, $n = 2$ for compound 2, etc.

Finally, in Chapter 4, we examine the unusual SO-ISC mechanism that is operative in both the PTZ-Ph$_n$-PDI and DMJ-An-Ph$_n$-NI systems. The DMJ-An molecule which serves as the donor for the DMJ-An-Ph$_n$-NI molecules in Chapter 3, is in fact an independent D-A system on its own where the donor and acceptor are formally linked by a single bond. These systems usually display CT absorption and emission bands and exhibit large excited state dipole moments which imply that significant electron density is transferred from the donor to the acceptor. In order to better understand the SO-ISC mechanism, we compare DMJ-An with J-An, Figure 1.3, where the presence of methyl groups at the 3- and 5- positions of the phenyl group serves to change the torsional angle (θ_1) between the π system of the anthracene and the nitrogen lone pair of the amine. Important to this work, we are able to compare systems where changes in a single

degree of freedom dramatically affect their photophysical behavior. TREPR studies show that

the primary mechanism of triplet formation in DMJ-An following photoexcitation is a spin-orbit

coupling mechanism which is similar to an n-π^* electronic transition within a single

chromophore. The SO-ISC mechanism depends on the degree of charge separation, the relative

orientation of the orbitals involved in the charge transfer, and the magnitude of the electronic

coupling between the donor and acceptor. Despite its similar structure, J-An does not display a

measurable triplet spectrum following photoexcitation. This result is a function of a decrease in

θ_1 due which serves to diminish the SO-ISC contribution in two distinct ways. As θ_1 deviates

from 90°, the degree of charge transfer decreases and the change in orbital angular momentum

which drives SO-ISC decreases. Given that the requirements for this mechanism to occur are

quite general, it is expected that it will be operative in a variety of systems.
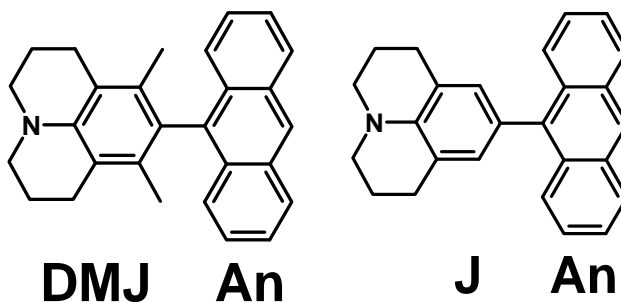
Figure 1.3. Chemical structures of **DMJ-An** and **J-An**.

In Chapter 5, the relevant experimental methods used in the above studies are described, including TREPR, time-resolved fluorescence anisotropy, temperature dependent nanosecond and femtosecond transient absorption, magnetic field effect experiments, and computational methods.

In closing, we find that the spin dynamics that accompany the energy and charge transfer events within these systems indicate the considerable level of structurally and energetically dependent mechanistic complexity responsible for energy, charge and spin transfer in organic materials. Furthermore, these results provide insights into how these structures may be controlled to enhance properties of interest in basic science or technology.

Chapter 2

Time-Resolved EPR Studies of Photogenerated Radical Ion Pairs

Separated by *p*-Phenylene Oligomers and of

Triplet States Resulting from Charge Recombination

2.1 Introduction

Developing a fundamental understanding of energy, charge, and spin transport in chemical systems for solar energy conversion is important for sustainable energy utilization. A major challenge lies in finding molecules that exhibit long distance charge transport mechanisms operating with the high efficiencies found in Nature.[16] In assembling electron donor-bridge-acceptor (D-B-A) systems optimized for the photoconversion of solar energy, the system must be designed to adopt the most efficient charge transport mechanism possible, one which maintains this efficiency as the bridge is lengthened.[17] The ability to achieve distance independent, or "wire-like", charge transport in artificial photosynthetic systems requires a thorough understanding of the three basic mechanisms involved in molecular non-resonant charge transfer processes. The first is superexchange, where an electron or hole is transferred in a single step from donor to acceptor and the bridge is used as a medium for electronic coupling.[18, 19] In superexchange, the redox state of the bridge does not change, and the probability of transferring an electron/hole between donor and acceptor generally decreases exponentially with distance. The second mechanism is incoherent tunneling, where an electron or hole tunnels under successive energy barriers from one site to the next until it reaches a charge trap.[20-22] The third mechanism is thermally-activated hopping, where the energy barrier between sites is lowered by nuclear rearrangement to such an extent that the electron or hole surmounts the barrier.[20] Because the length dependence of incoherent charge transfer mechanisms is weak, systems that utilize them are sometimes said to display molecular wire-like behavior.[23] Most often, charge transfer within complex systems is due to some mixture of these three mechanisms,[24-26] with the proportion of each determined by electronic energy level matching and electronic coupling,

which are in turn determined primarily by bridge length, conformational rigidity, temperature, and the electronic properties of the redox centers.[27-31]

In the superexchange mechanism the bridge orbitals are energetically well-separated from those of the donor and acceptor and the electronic coupling matrix element, V_{DA}, gives the effective interaction energy between the relevant orbitals on the donor and acceptor.[32-34] Importantly, the rate of electron transfer is proportional to V_{DA}^2, which is a strong function of D-B-A structure.[35, 36] Moreover, when the charge transport process originates from a state in which the redox centers are also paramagnetic, e.g. charge recombination from a radical ion pair (RP) state $D^{+\bullet}$-B-$A^{-\bullet}$, the superexchange coupling, V_{DA}, which dictates charge transfer is the same coupling that determines the magnetic interaction between the unpaired spins in the RP. Therefore, the magnitude of the magnetic spin-spin exchange interaction, i.e. the singlet-triplet splitting, between the two radicals, *2J*, and its dependence on molecular structure mirror that of V_{DA}.[32-34, 37-42] We have demonstrated earlier that 2*J* is proportional to V_{DA}^2, and is highly sensitive to both the RP distance and the structure of the intervening bridge system.[29, 30, 43-46]

PDI   **Ph_n**   **PTZ**

Figure 2.1. Chemical structure of PTZ-Ph$_n$-PDI, where n = 1 for compound **1**, n = 2 for compound **2**, etc.

In this study, we use time-resolved EPR (TREPR) spectroscopy to explore the spin dynamics in a series of D-B-A molecules, which have been studied earlier using transient optical absorption spectroscopy and optically-detected magnetic field effects (MFEs) on charge recombination.[29, 30] The D-B-A system consists of a series of *p*-phenylene (Ph$_n$) oligomers, where n = 1-5, that link a phenothiazine (PTZ) electron donor to a perylene-3,4:9,10-bis(dicarboximide) (PDI)[47] electron acceptor, Figure 2.1. Previous work has shown that selective photoexcitation of PDI within PTZ-Ph$_n$-PDI results in charge separation to produce a spin-coherent singlet radical ion pair (RP), ^{1}(PTZ$^{+\bullet}$-Ph$_n$-PDI$^{-\bullet}$).[29, 30] The subsequent RP recombination dynamics depend on temperature and the magnitude of *2J*, both of which reflect structural changes within the RP.

2.1.1 Radical Pair Intersystem Crossing and Triplet States from Charge

Recombination.

The mechanistic details of the radical pair intersystem crossing mechanism (RP-ISC) and the theory behind magnetic field effects on electron transfer reactions have been researched extensively[48-51] and have been applied to many donor-acceptor systems[29, 43, 44, 52-57] including biological systems.[49, 58-61] Following charge separation, an initially formed singlet RP will undergo electron-nuclear hyperfine coupling-induced RP-ISC to produce the triplet RP, k_{ST}^{RP}, Figure 2.2A, provided that the hyperfine interactions are comparable to or larger than *2J* and the dipolar interaction (*D*) between the two radicals. Since the hyperfine interactions within each radical are usually small, this implies that *2J* and *D* must be small as well. The subsequent charge recombination process is spin selective; i.e. the singlet RP $^1(D^{+\bullet}\text{-B-A}^{-\bullet})$ recombines to the singlet ground state D-B-A with a rate constant k_{SS}^{CR}, while the triplet RP $^3(D^{+\bullet}\text{-B-A}^{-\bullet})$ recombines to yield the neutral local triplet $^{3*}(D\text{-B-A})$ with a rate constant k_{TT}^{CR}. Application of a magnetic field results in Zeeman splitting of the RP triplet sublevels, which at low fields are best described by the zero-field eigenstates, T_X, T_Y, and T_Z that are quantized in the molecular framework, and at high fields are best described by the T_{+1}, T_0, and T_{-1} eigenstates that are quantized along the applied magnetic field, Figure 2.2B. If *2J* > 0, the singlet energy level is above that of the triplet sublevels, Figure 2.2B, so that when the Zeeman energy from the applied field equals that of the singlet-triplet splitting, the highest energy triplet sublevel crosses the singlet level, and the RP-ISC rate is maximized. This mixing populates the triplet manifold which, following spin-selective recombination, should produce a resonance in the triplet yield at B_{2J}, directly yielding *2J*.[32, 62] If *2J* < 0, the singlet energy level, S, is below that of the triplet

sublevels, and the lowest energy triplet sublevel crosses S yielding the same information. The appearance of a distinct resonance depends critically on having a RP in which the two radicals have a relatively narrow distribution of distances and orientations between them, as in **1**-**5**, where there is a linear donor-acceptor geometry with donor-acceptor distances of 12.8, 17.1, 21.4, 25.7, and 30.0 Å, respectively. Consequently, the observed resonances are extremely sensitive to small changes in molecular structure. We have previously used magnetic field effects (MFEs) on RP and triplet recombination product yields to measure the values of *2J* for **2**-**5** at room temperature,[29] and the temperature dependence of *2J* for **2**-**4**.[30]
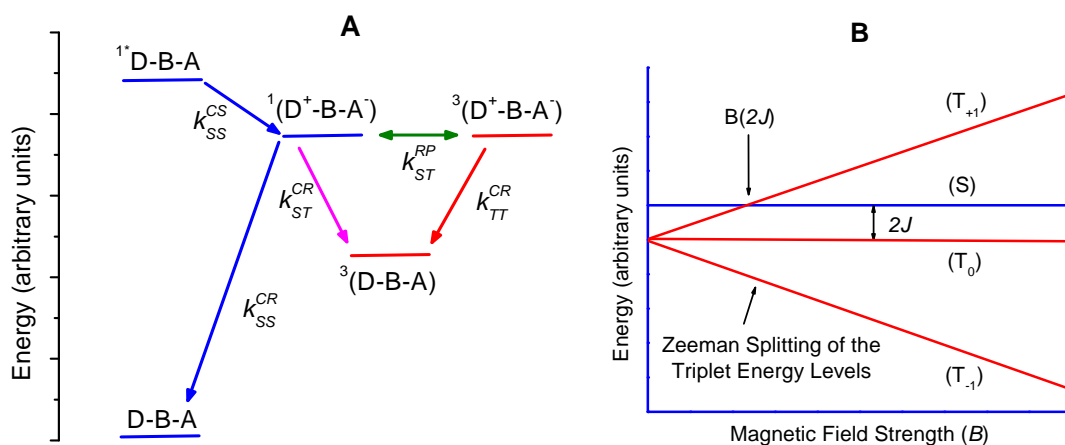
Figure 2.2. A) Electron transfer and intersystem crossing pathways in a D-B-A system; B) Radical ion pair energy levels as a function of magnetic field for *2J* > 0.

The magnitude of *2J* depends exponentially on the RP distance,

$$2J = 2J_0 e^{-\alpha(r-r_0)} \tag{1}$$

where *r* is the defined RP distance, α is a constant, and *2J_0* is the value of spin-spin exchange interaction at *r_0*, the minimum RP separation. In the high field limit at long RP distances, typically $\geq$ 15-20 Å, population of the RP triplet state occurs exclusively by S-T_0 mixing,

provided that *2J* and *D* are small relative to the Zeeman splitting $g\beta\mathbf{B}$, where *g* is the electronic *g*-factor, β is the Bohr magneton, and **B** is the applied magnetic field. At shorter RP distances, where $|2J|$ is large, two additional intersystem crossing mechanisms that also depend on the formation of the singlet radical pair precursor can operate. First, if $|2J| \sim g\beta\mathbf{B}$ and $|2J|$ is large enough so that S-T$_0$ mixing is inefficient, S-T$_{+1}$ (*2J* > 0) or S-T$_{-1}$ (*2J* < 0) mixing may occur. Second, if $|2J| \gg g\beta\mathbf{B}$, S-T$_0$, S-T$_{+1}$, and S-T$_{-1}$ mixing are all inefficient. Nevertheless, rapid intersystem crossing from the singlet radical pair may take place via a spin-orbit coupling mechanism to produce ^{3*}(D-B-A) directly by charge recombination, k_{ST}^{CR}, Figure 2.2A, provided that the symmetries of the orbitals involved in the electron transfer are such that the spin flip is accompanied by a significant change in orbital angular momentum.[63-67] The first alternative mechanism will be discussed briefly later in this section, while the second mechanism will be discussed at length in the Discussion section.

Optically-detected MFE measurements on reactant or product yields do not show how the spin polarization of the radicals within the RP evolves with time, how the structure of radicals may be changing, or how the dynamics of the medium couple with the spin dynamics of the RP. Fortunately, TREPR measurements can yield this information directly.[50, 68, 69] If *2J* and/or *D* are small, yet nonzero, S-T$_0$ mixing within D$^{+\bullet}$-B-A$^{\bullet}$ will result in formation of so-called spin-correlated radical pair (SCRP) states that can be identified through the unique polarization of the EPR transitions that occur between them.[50, 68, 70-77] If *2J* is larger, as may be the case when the D$^{+\bullet}$-B-A$^{\bullet}$ distance is shorter, mixing of the S state of the radical pair with either T$_{+1}$ (*2J* > 0) or T$_{-1}$ (*2J* < 0) may also occur, which results in different polarization of the EPR transitions relative to those that result from S-T$_0$ mixing.[77]

Without taking into account hyperfine interactions, the SCRP spectrum consists of two anti-phase doublets, centered at the g-factors of the individual radicals that comprise the pair. The splitting in each doublet is determined by 2J and D. Resolved hyperfine interactions lead to further splitting of the doublet for each radical. The experimentally observed SCRP spectrum is a superposition of the four-line spectra for all possible nuclear states of the RP, as well as all orientations with respect to the external magnetic field, B. The positions (ω_{ij}) of the four EPR transitions for a SCRP are[50, 71, 72]

$$\omega_{12} = \omega_0 - \Omega - J + D_{ZZ} \; ; \; \omega_{34} = \omega_0 - \Omega + J - D_{ZZ} \tag{2a,b}$$

$$\omega_{13} = \omega_0 + \Omega - J + D_{ZZ} \; ; \; \omega_{24} = \omega_0 + \Omega + J - D_{ZZ} \tag{2c,d}$$

where $\omega_0 = \frac{1}{2}(\omega_{PDI} + \omega_{PTZ})$ is the center of the spectrum,

$$\Omega^2 = (J + D_{ZZ}/2)^2 + Q^2 \tag{3}$$

and $D_{zz} = D[3\cos^2(\xi) - 1]$ \hfill (4)

where ξ is the angle between the dipolar axis of the radical pair and the direction of the magnetic field **B**. The mixing term Q between singlet and triplet states is

$$Q = \frac{1}{2}(g_1 - g_2)\,\beta\mathbf{B}/\,\hbar + \frac{1}{2}(\sum a_{1i}m_{1i} - \sum a_{2j}m_{2j}) \tag{5}$$

where g_1 and g_2 are the g-factors of radicals 1 and 2, a_{1i} and a_{2j} are the hyperfine coupling constants of radicals 1 and 2. The intensities of the transitions are

$$-I_{12} = -I_{13} = I_{24} = I_{34} = Q^2/(4\Omega^2) \tag{6}$$

The electron spin polarization (ESP) pattern of the EPR signal, i.e. which transitions are in enhanced absorption (A) or emission (E), is determined by the SCRP sign rule,

$$\Gamma = \mu \cdot \text{sign}[J - D(3 \cos^2 (\xi) -1)] = (-) \text{ gives E/A or } = (+) \text{ gives A/E} \tag{7}$$

where μ is -1 or +1 for a singlet or triplet excited state precursor, respectively. The model outlined above implicitly assumes that the decay rate constant from the singlet RP, k_{SS}^{CR}, is equal to the decay rate from the triplet RP, k_{TT}^{CR}, Figure 2.2A. However, the singlet and triplet RP generally recombine with different rates, i.e., $k_{SS}^{CR} \neq k_{TT}^{CR}$. Till and Hore[50] have extended the SCRP model to describe a non-diffusing, exchange and/or dipolar coupled radical pair in a strong static magnetic field incorporating the ability to assign different values to k_{SS}^{CR} and k_{TT}^{CR}.

The non-Boltzmann spin populations within the SCRP are transferred to the neutral triplet state ^{3*}(D-B-A) that results from radical ion pair recombination within ^{3}(D$^{+\bullet}$-B-A$^{-\bullet}$).[68, 78] The main features of the EPR spectrum of ^{3*}(D-B-A) arise from zero-field splitting (ZFS), which is a result of the magnetic dipole-dipole interaction between the two unpaired electrons in the triplet state. The Hamiltonian that describes this interaction is:[79-82]

$$\mathcal{H}_{\text{dipolar}} = D(\mathbf{S_z}^2 -\mathbf{S}^2/3) + E(\mathbf{S_x}^2-\mathbf{S_y}^2) \tag{8}$$

where D and E are the zero-field-splitting parameters and $\mathbf{S_{x,y,z}}$ are the components of the total spin angular momentum operator ($\mathbf{S}$) for the triplet state. The effect of this term is to lift the degeneracy of the triplet manifold in the absence of an external magnetic field as a function of the symmetry of the molecule. The polarization of the EPR transitions exhibited by ^{3*}(D-B-A) formed by a spin-orbit intersystem crossing (SO-ISC) mechanism can be differentiated from the RP-ISC mechanism by the ESP pattern of the six EPR transitions, i.e. the two transitions at each canonical (x, y, z) orientation.[78] In SO-ISC, the three zero-field levels T$'_X$, T$'_Y$, and T$'_Z$ of ^{3*}(D-B-A) are selectively populated and this selectivity is carried over to the high field energy levels.

For example, assuming selective population of the T'_Y zero-field level and $D > 0$, Figure 2.3A shows that the six EPR transitions from low to high field yield an (e,a,e,a,e,a) polarization pattern, where a = enhanced absorption and e = emission. In contrast, RP-ISC acts directly on the high-field triplet sublevels of the RP via S-T_0 (or S-$T_{\pm 1}$) mixing, Figure 2.3B. Spin polarization is preserved upon recombination so that an (a,e,e,a,a,e) polarization pattern exhibited by ^{3*}(D-B-A) is the unique signature of the RP-ISC mechanism within $D^{+\bullet}$-B-$A^{-\bullet}$.
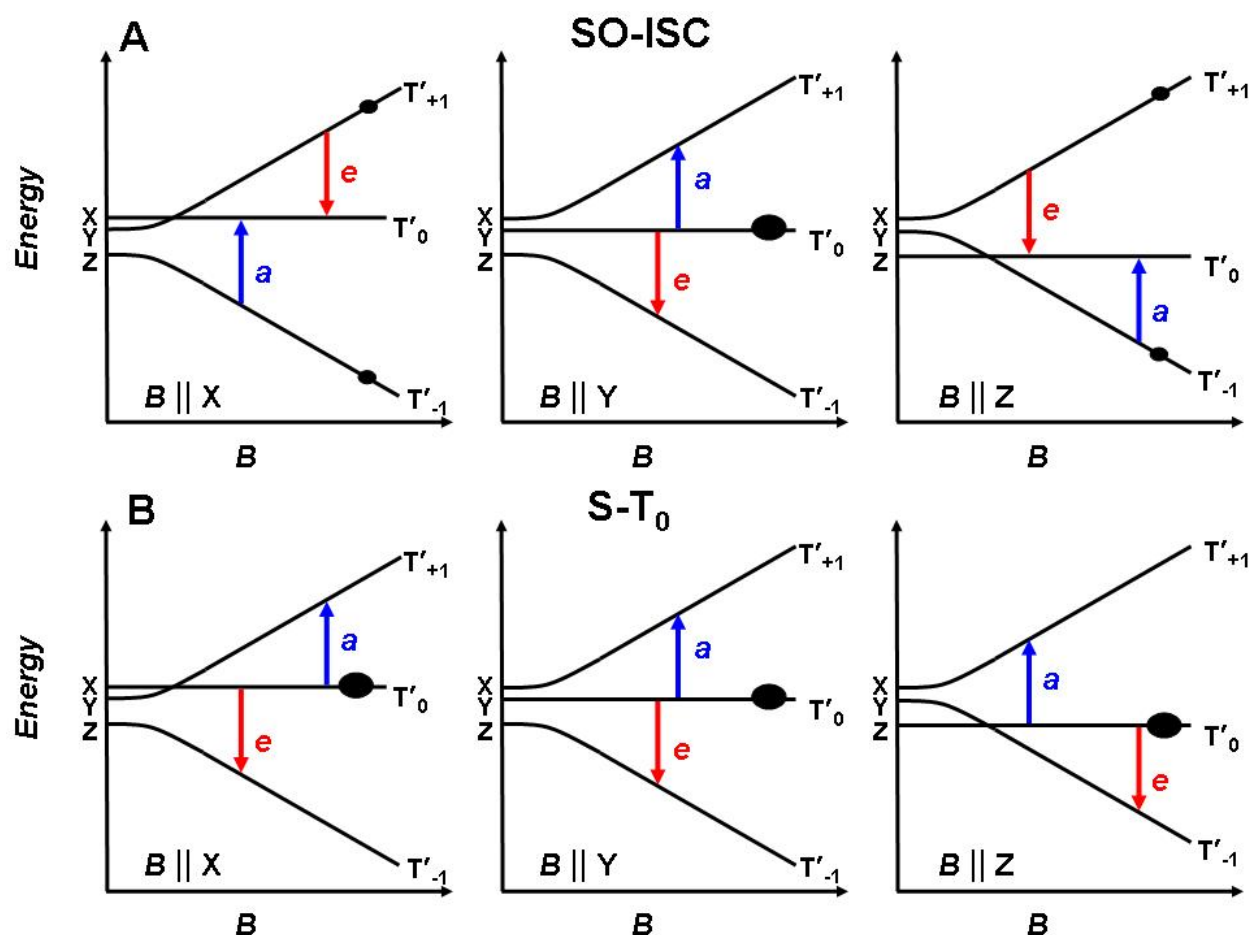
Figure 2.3. Energy levels of ^{3*}(D-B-A) formed by (A) SO-ISC with selective population of T'_Y ($D > 0$) and (B) S-T_0 mixing within a RP precursor. The arrows indicate the direction of the transition and are labeled a = enhanced absorption, e = emission.

2.2 Results

2.2.1 Synthesis

The synthesis and characterization of compounds **1-5** has been reported previously.[29] For TREPR, compounds **1-5** were purified by preparative TLC. Samples (~1 mM in toluene) were loaded in 4-mm OD × 2-mm ID quartz tubes and subjected to several freeze-pump-thaw degassing cycles on a vacuum line (10^{-4} Torr). The tubes were then sealed with a hydrogen torch. All samples were prepared in freshly distilled ACS grade toluene.

2.2.2 Radical Pair TREPR Spectra.

Femtosecond transient absorption experiments have shown that photoexcitation of PDI in **1**–**5** produces ^{1*}PDI exclusively, followed by rapid, nonadiabatic electron transfer from PTZ to ^{1*}PDI to give ^{1}(PTZ$^{+\bullet}$-Ph$_{1-5}$-PDI$^{\bullet}$).[29] The approximate energy levels for the relevant electronic states are given in Figure 2.4.[29] Following photoexcitation, spin-polarized RP signals were observed for both **4** and **5**, Figure 2.5, while a very weak signal was observed for **3** only at low temperatures (shown below in Figure 2.6C), and no signals were observed for **1** or **2**. The RP spectra of **4** and **5** were simulated with the SCRP mechanism using the model of Till and Hore.[50] The best fits to the data are given in Figure 2.5, while the fitting parameters are summarized in Table 2.1. Due to the weak nature and poor signal-to-noise ratio of the RP signal from **3**, no attempt was made to simulate it, while the fits for **4** are only approximate due to the same limitations. The measured *g*-factors and hyperfine coupling constants of PDI$^{\bullet}$,[83] and PTZ$^{+\bullet}$,[84] were used in the simulations. These quantities were assumed to be temperature independent. Following from Equation 7, 2*J* is positive for the RPs in both **4** and **5**, given that photoexcitation of PDI initially produces a singlet RP,[29] and that the experimentally determined absolute phases

of the RP spectra are E/A.[85, 86] The dipolar interaction between the electron spins in both **4**

and **5** is ≤ 0.3 mT due to the long RP distances.[77]
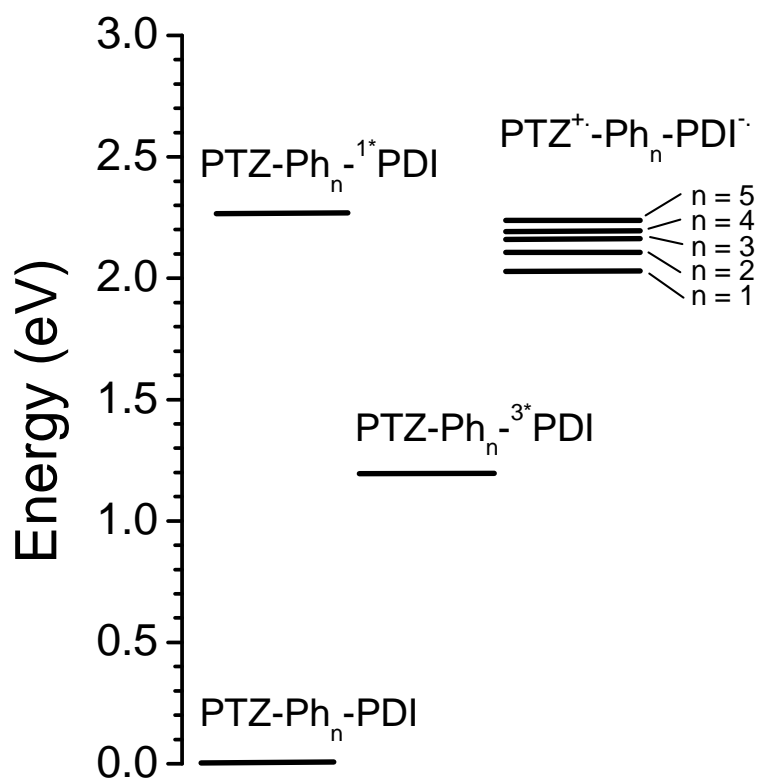
Figure 2.4. Energy levels for the electronic states relevant to the electron transfer pathways for **1-5**.
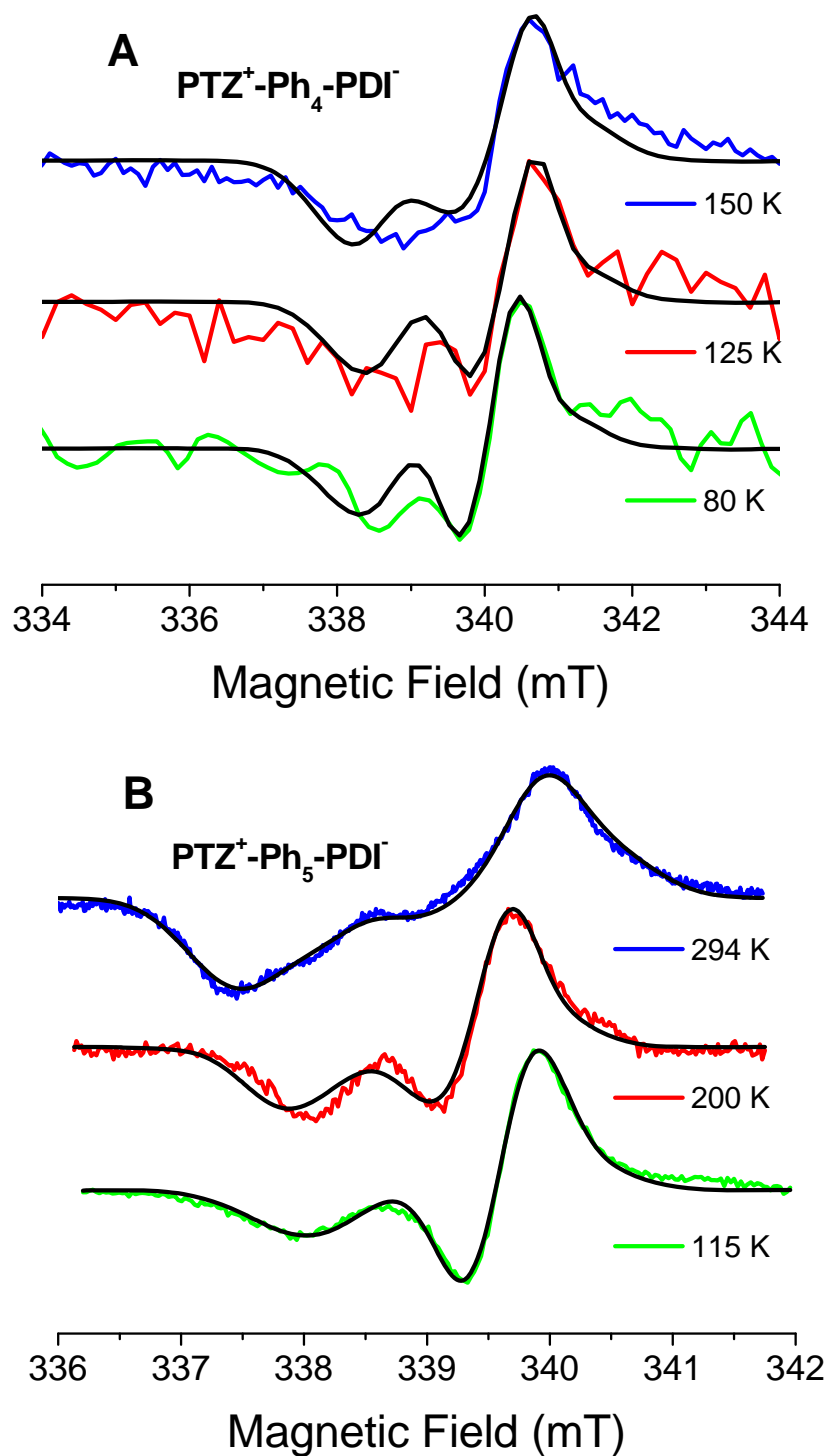
Figure 2.5. TREPR spectra of (A) PTZ$^{+\bullet}$-Ph$_4$-PDI$^{\bullet}$ and (B) PTZ$^{+\bullet}$-Ph$_5$-PDI$^{\bullet}$ at 100 ns following a 532 nm, 1.5 mJ laser pulse at the indicated temperatures in toluene. Smooth curves superimposed on the experimental spectra are computer simulations of the radical pair spectra (see text) with the parameters given in **Table 2.2**. Positive features are in enhanced absorption, while negative features are in emission.

Table 2.1. RP simulation parameters for **4** and **5** at 100 ns after the laser pulse

Compound	T(K)	2*J*(mT)	k_{SS}^{CR} (s⁻¹)	k_{TT}^{CR} (s⁻¹)
4	150	0.9 ± 0.3	$9 \pm 1 \times 10^6$	$3 \pm 0.1 \times 10^7$
4	125	0.8 ± 0.3	$1 \pm 0.1 \times 10^7$	$2 \pm 0.1 \times 10^7$
4	80	0.7 ± 0.3	$1 \pm 0.1 \times 10^7$	$2 \pm 0.1 \times 10^7$
5	294	1.0 ± 0.05	$3.5 \pm 0.5 \times 10^6$	$2.7 \pm 0.5 \times 10^7$
5	200	0.52 ± 0.05	$4.2 \pm 0.5 \times 10^6$	$2.5 \pm 0.5 \times 10^7$
5	115	0.42 ± 0.05	$1.2 \pm 0.5 \times 10^7$	$1.6 \pm 0.5 \times 10^7$

2.2.3 TREPR Spectra of Triplet States Resulting from Charge Recombination.

The TREPR spectra of **5** exhibit two major features at all temperatures: a broad triplet spectrum with a width of ~76 mT, having an electron spin polarization (ESP) phase pattern that changes as a function of temperature, Figure 2.6A, and the narrow RP spectrum at $g \sim 2$, which was discussed above, superimposed on the triplet spectrum. The broad triplet spectrum is detectable at temperatures ranging from 80 K to as high as 225 K, at which toluene is *an isotropic liquid*. The ESP phase pattern is (*a,e,e,a,a,e*) above 125 K, but changes gradually to (*e,e,e,a,a,a*) below 125 K due to the onset of a competitive SO-ISC mechanism.

A PTZ-Ph$_5$-PDI

225 K
200 K
150 K
125 K
80 K

z' x   y   y'   x' z

280   300   320   340   360   380   400

Magnetic Field (mT)

B PTZ-Ph$_4$-PDI

200 K
150 K
125 K
80 K

z' x   y   y'   x' z

280   300   320   340   360   380   400

Magnetic Field (mT)

C **PTZ-Ph₃-PDI**

200 K

150 K

125 K

80 K

z' x   y   y'   x' z

280   300   320   340   360   380   400

Magnetic Field (mT)

D **PTZ-Ph₂-PDI**

200 K

150 K

125 K

80 K

z' x   y   y'   x' z

280   300   320   340   360   380   400

Magnetic Field (mT)
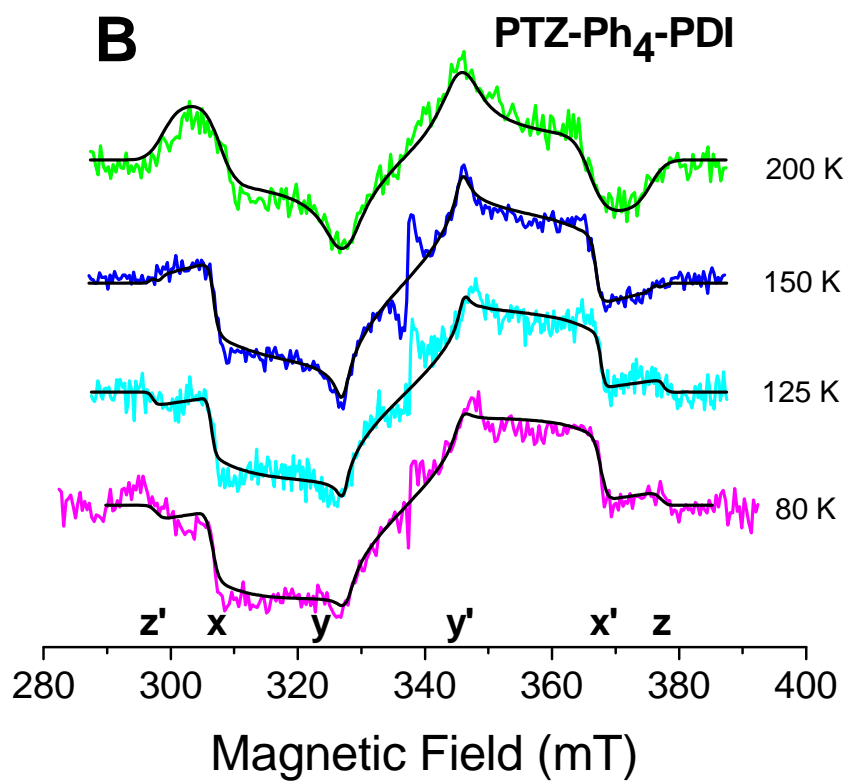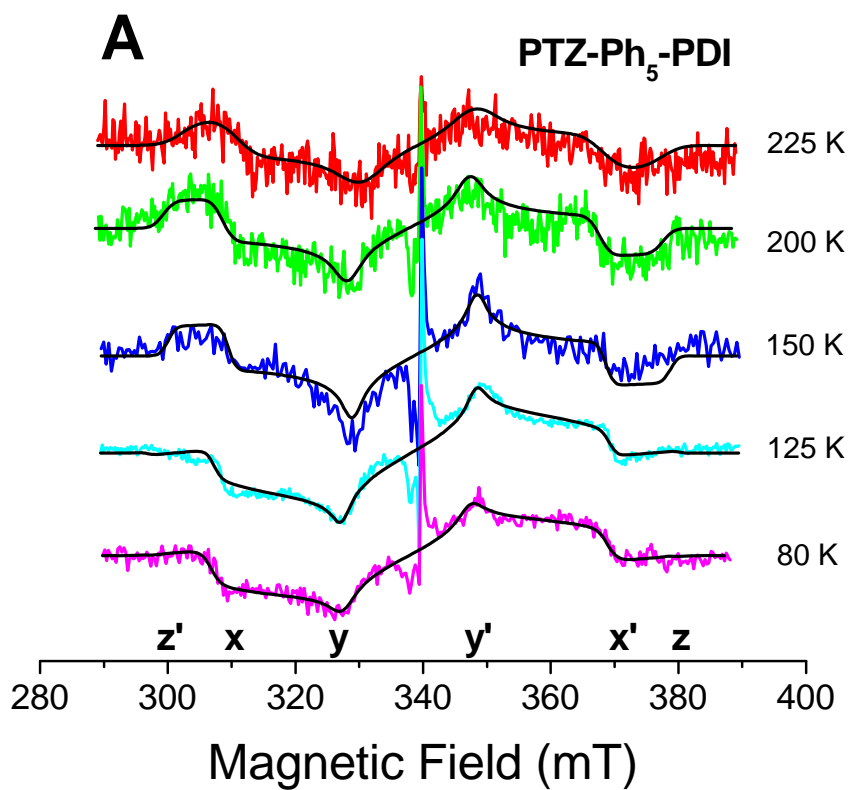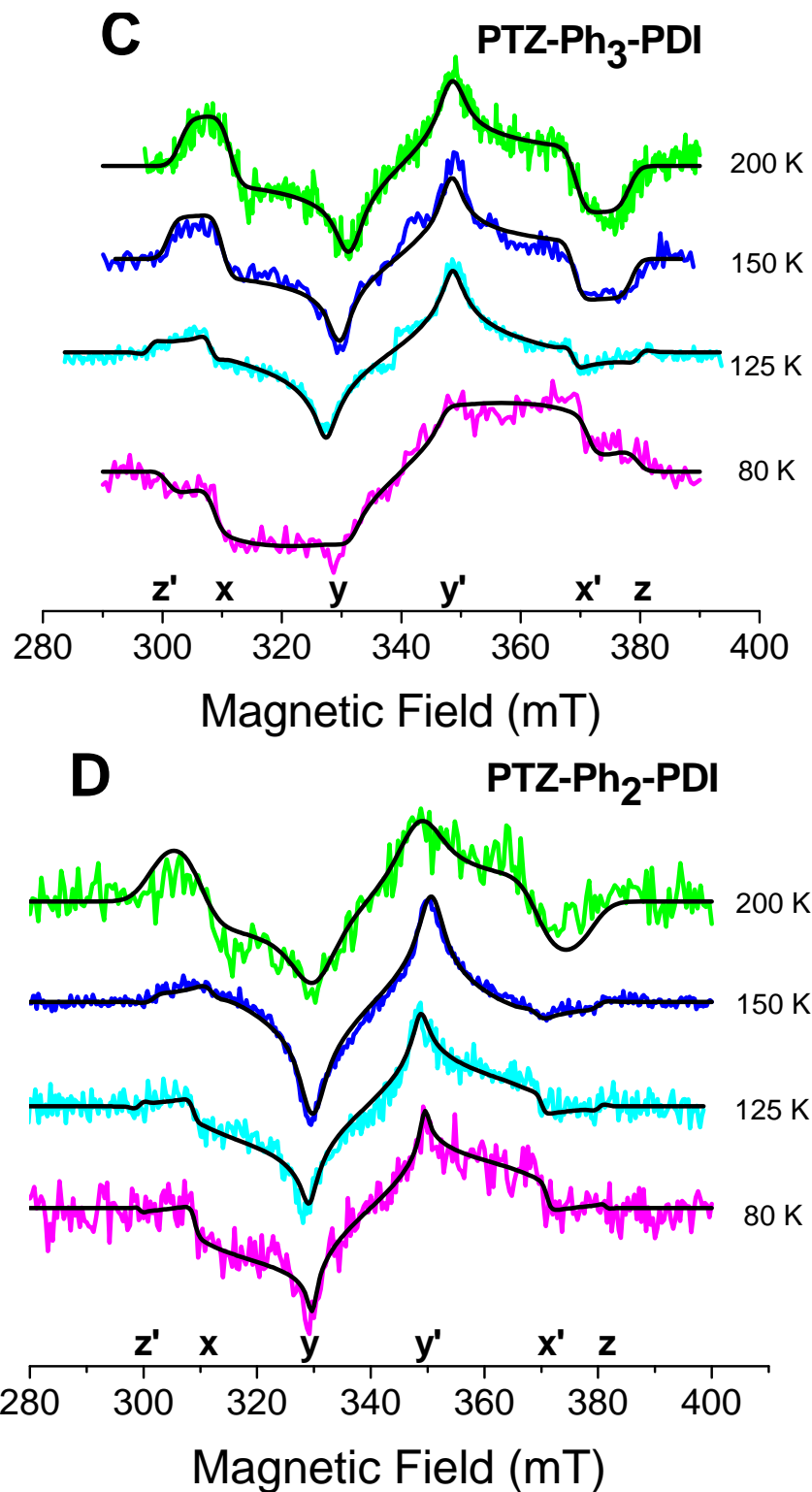
Figure 2.6. TREPR spectra of A) **5**, B) **4**, C) **3**, and D) **2** in toluene at the indicated temperatures at 200 ns following a 532 nm, 1.5 mJ laser pulse. The sharp features at the center of the spectra in A) and B) are the radical pair signals, while the broad features are PTZ-Ph$_n$-^{3*}PDI. The canonical orientations of each transition are indicated. Smooth curves superimposed on the experimental spectra are computer simulations of the triplet with the parameters given in Table 2.2.

The TREPR spectra of **2-4** show characteristics that are similar to those of **5,** Figure 2.6B-D, i.e. a broad triplet spectrum is present over a large temperature range. The triplet ESP phase patterns for **2-4** also exhibit temperature dependencies analogous to that of **5**. The narrow spectrum resulting from the RP is only observed in **4** at lower temperatures, is barely visible for **3** at lower temperatures, and is absent for **1** and **2** at all temperatures. The TREPR spectra of **1**, Figure 2.7, are very different from those of **2-5**. The broad triplet spectrum is only present below the melting point of toluene (~160 K). The (*e,a,e,a,e,a*) ESP pattern is indicative of a SO-ISC mechanism and remains constant at all temperatures at which the spectrum is observed.

Table 2.2. Zero-field splitting parameters (*D* and *E*) and relative population rates of the zero-field spin states obtained from simulations of the triplet state TREPR spectra of **1-5**

Compound 5

T (K)	D (mT)[a]	E (mT)[a]	A'_x[b]	A'_y[b]	A'_z[b]	c_{RP}[c]	c_{SO}[c]
225	37.62	-6.57				1.0	
200	39.17	-6.65				1.0	
150	39.36	-6.62				1.0	
115	41.65	-6.88	0.86	1	0	0.31	0.69
80	41.16	-7.11	1	0.91	0	0.40	0.60

Compound 4

T (K)	D (mT)[a]	E (mT)[a]	A'_x[b]	A'_y[b]	A'_z[b]	c_{RP}[c]	c_{SO}[c]
200	38.39	-6.64				1.0	
150	39.37	-6.88	1	0.76	0	0.57	0.43
125	40.19	-7.10	1	0.81	0.005	0.25	0.75
80	39.69	-7.21	1	0.73	0	0.24	0.76

Compound 3

T (K)	D (mT)[a]	E (mT)[a]	A'_x[b]	A'_y[b]	A'_z[b]	c_{RP}[c]	c_{SO}[c]
200	37.60	-6.78				1.0	
150	39.48	-6.70	0.13	1	0.45	0.96	0.04
125	40.81	-6.88	0.69	1	0	0.40	0.60
80	39.87	-7.70	1	0.82	0	0.04	0.96

Compound 2

T (K)	D (mT)[a]	E (mT)[a]	A'_x[b]	A'_y[b]	A'_z[b]	c_{RP}[c]	c_{SO}[c]
200	39.02	-6.77				1.0	
150	39.16	-6.07	0	1	0.15	0.46	0.54
125	40.45	-6.96	0.49	1	0	0.40	0.60
80	40.97	-7.09	0.77	1	0	0.29	0.71

Compound 1

T (K)	D (mT)[a]	E (mT)[a]	A'_x[b]	A'_y[b]	A'_z[b]	c_{RP}[c]	c_{SO}[c]
150	38.78	-6.59	0.11	1.0	0		1.0
125	41.62	-7.56	0.35	1.0	0		1.0
80	41.62	-7.56	0.35	1.0	0		1.0
40	39.82	-6.50	0.10	1.0	0		1.0

[a] *D* and *E* parameters obtained using Equation 8 to fit experimental results

[b] relative population rates for spin-orbit intersystem crossing (SO-ISC)

[c] coefficient preceding S-T_0 contribution and SO-ISC contribution to the overall fit using the functional form: c_{RP} * (S-T_0) + c_{SO} * (SO-ISC)

The parameters from the line shape analysis of the broad triplet spectra are summarized in Table 2.2. All spectra in **2-5** were simulated using a linear combination of RP-ISC and SO-ISC mechanisms. The spectra of **3-5** exhibit ESP phase patterns that are primarily a result of the S-T_0 RP-ISC mechanism at 150 K and above. However, as the temperature decreases, the ESP pattern changes, with the simulations indicating that a SO-ISC mechanism is the main source of ^{3*}PDI at lower temperatures. The spectra of **2** are similar to **3-5**, but the temperature at which the SO-ISC mechanism becomes the principal source of ^{3*}PDI occurs between 150 and 200 K. The ^{3*}PDI signal from 1 is simulated using the SO-ISC mechanism exclusively (no contribution from RP-ISC), and the relative population rates heavily favor the T'_Y spin state relative to T'_X or T'_Z states. The fits are in good agreement with experimental results at 150 K and 40 K. However, at 125 K and 80 K, the simulations deviate from experimental results for the outermost transitions, Figure 2.7.

PTZ-Ph$_1$-PDI
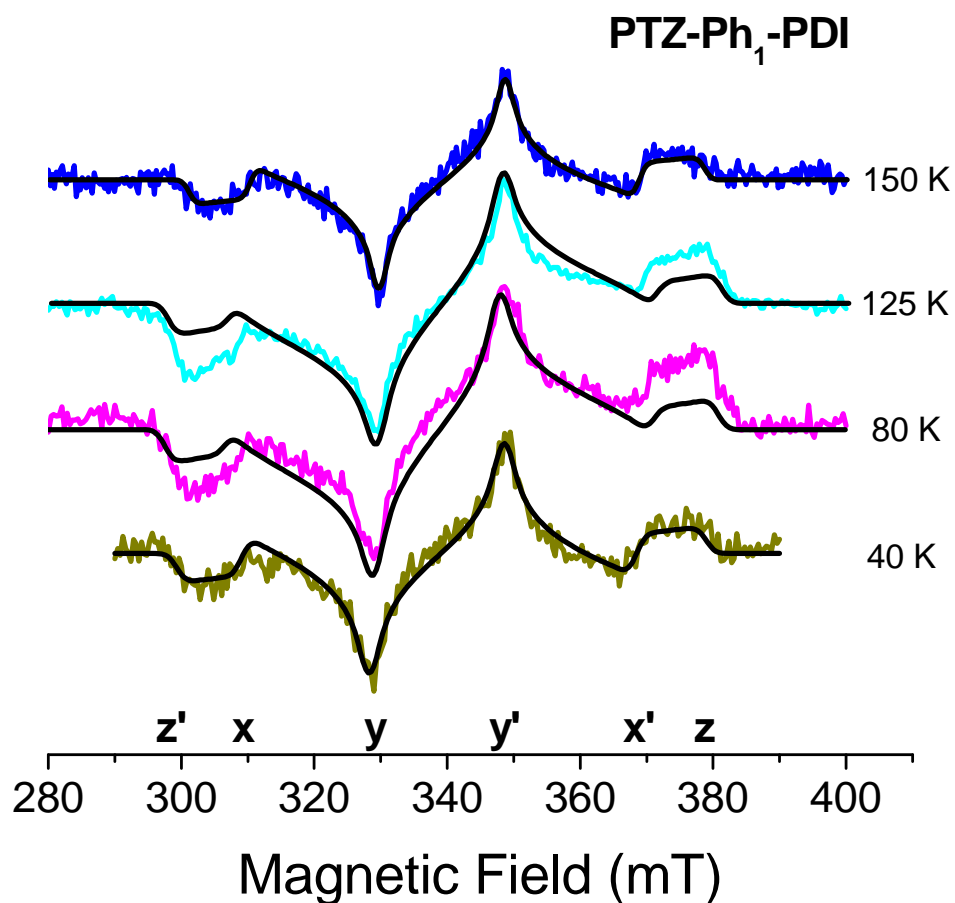
Figure 2.7. TREPR spectra of PTZ-Ph$_1$-^{3*}PDI in toluene at the indicated temperatures at 200 ns following a 532 nm, 1.5 mJ laser pulse. The canonical orientations of each transition are indicated. Smooth curves superimposed on the experimental spectra are computer simulations of the triplet with the parameters given in Table 2.2.

2.2.4 Experimental determination of the absolute phase of the TREPR spectra

The broad spectra are assigned to PTZ-Ph$_n$-^{3*}PDI because the lowest excited triplet state of PDI (^{3*}PDI = 1.2 eV) is far below the lowest excited triplet state of PTZ (^{3*}PTZ = 2.60 eV).[29] The absolute phase of the spectra was determined using zinc tetraphenylporphyrin (ZnTPP) as an internal standard because the absolute phase of the ^{3*}ZnTPP EPR spectrum has been established.[87] An oxygen free, sealed capillary tube of ZnTPP in MTHF was prepared and inserted into a sample of **5** in toluene which was then degassed and sealed to give model system

5(ZnTPP). This arrangement allows simultaneous observation of the ^{3*}ZnTPP and ^{3*}PDI signals, yet prevents chemical interaction of these species during the EPR experiment

Figure 2.8 compares the spectra of **5(ZnTPP)** at 80 K to that of an independent spectrum of ^{3*}ZnTPP at 10 K. The ^{3*}ZnTPP spectrum was taken ~100 ns after the laser pulse and is shown at that time in both Figure 2.8a and Figure 2.8b while the time evolution of the **5(ZnTPP)** signal is shown at 100 and 500 ns, respectively. As time progresses, we see the development of the ^{3*}PDI and can clearly assign the ESP pattern values **-,e,e,a,a,-** to the inner transitions. Canonical orientations 1 and 6 of **5** overlap with the outermost orientations ($Z_{I,II}$ and $Y_{II,I}$) of the ^{3*}ZnTPP signal and thus we cannot assign the ESP using these lines. Regardless, these data directly indicate the absolute phase of the spectrum in PTZ-Ph$_5$-^{3*}PDI at 80 K. Furthermore, the triplet phase pattern of canonical orientations in 3 and 4 (**-,-,e,a,-,-**) remain constant at all temperatures (Figure 2.8a), and the RP signal is clearly **e,a** relative to the 3*ZnTPP spectrum (Inset, Figure 2.8). Thus we can assign an **a,e,e,a,a,e** phase pattern to **5** at temperatures above 125 K. Finally, these results suggest that the same phase pattern assignments are applicable to PTZ-Ph$_{2,3,4}$-^{3*}PDI.

In the same manner as described above, a sample of **1(ZnTPP)** was prepared by inserting a sealed capillary tube of ZnTPP in MTHF into an EPR tube of **1** in toluene. Using a similar analysis, we can assign an absolute ESP phase pattern of **e,a,e,a,e,a** to **1** at all temperatures.
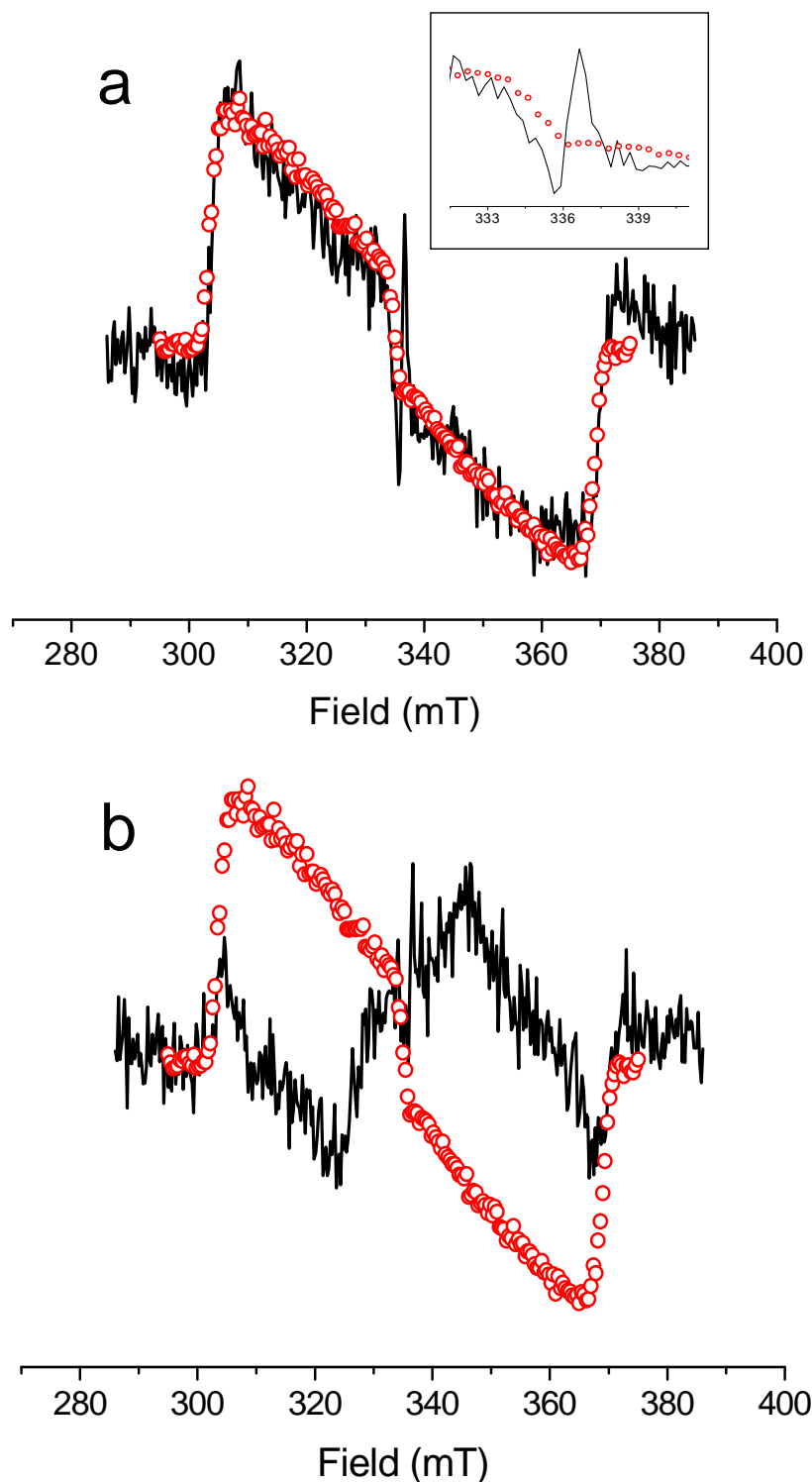
Figure 2.8. Plots of **5(ZnTPP)** (solid black line) at 80 K against ^{3*}ZnTPP (ooo) at 10 K. The ^{3*}ZnTPP spectrum is taken ~100 ns after excitation and is shown at that time in both (a) and (b) so the time evolution of the **5(ZnTPP)** signal is clear. (a) Solid line – spectrum of **5(ZnTPP)** at ~100 ns after 532 nm excitation. Inset: Expanded view of the **5(ZnTPP)** RP signal (e,a) relative to the ^{3*}ZnTPP spectrum. (b) Solid line – spectrum of **5(ZnTPP)** at ~ 500 ns shows development of the ^{3*}PDI signal.

2.2.5 Temperature Dependent UV-vis Spectroscopy.

The ground-state UV-vis spectra of compounds **1-5** at room temperature have an absorption band at 550 nm due to PDI with a lower intensity vibronic band at 515 nm. Additionally, there is a feature between 300 and 350 nm from Ph_n that red shifts and grows in intensity relative to the PDI peaks as n increases.[29] Temperature dependent UV-vis spectra of **3**, Figure 2.9 and **5** (not shown) reveal that as the temperature is lowered from room temperature to 184 K, there is an enhancement of the 515 nm peak relative to the 550 nm peak. Previous work has shown that a fully covalent, cofacial PDI_2 reference dimer displays a very similar enhancement of the 515 nm band at the expense of the 550 nm band.[29, 47, 88, 89] The increasing intensity of the 515 band as the temperature is lowered suggests that the PDI acceptors in these D-B-A molecules aggregate in a parallel, π-stacked geometry. In fact, some aggregation of the PDI chromophores is apparent at temperatures as high as 230 K.
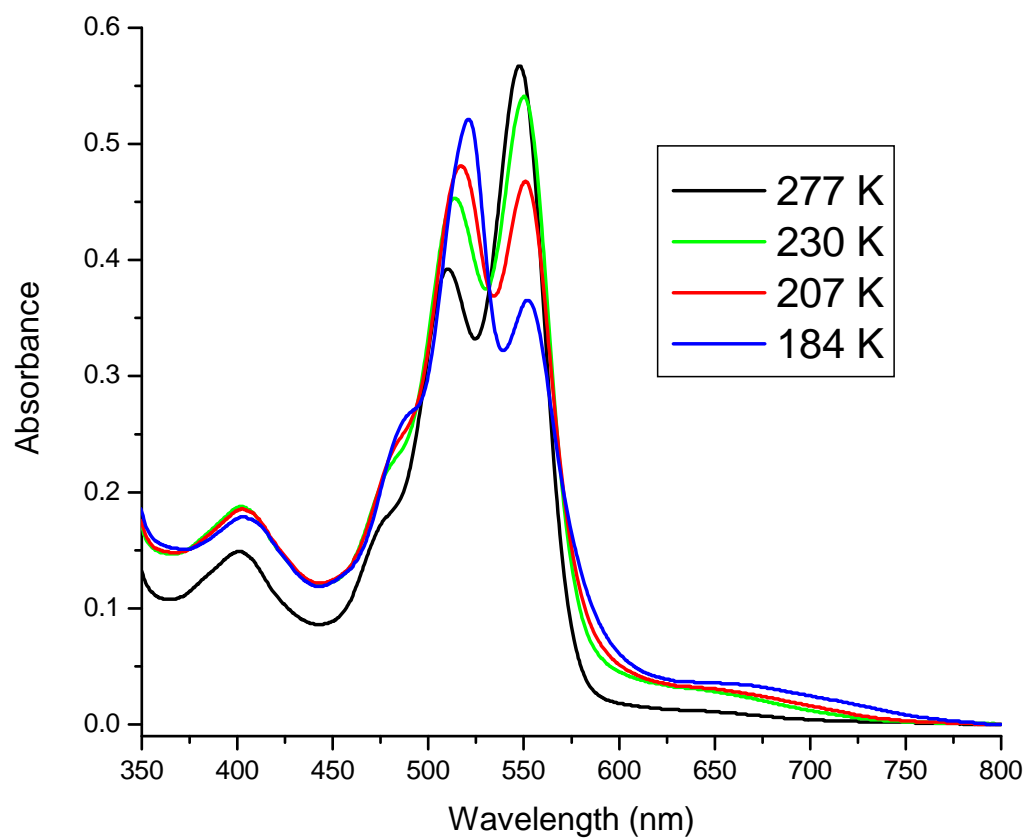
Figure 2.9. Optical absorption spectra of PTZ-Ph$_3$-PDI in toluene at the indicated temperatures.

2.2.6 Time-resolved Fluorescence Anisotropy.

The time-resolved fluorescence results are summarized in Table 2.3. Because the emission transition dipole lies along the long axis of the PDI molecule, the anisotropies are expected to decay to zero according to a simple exponential model:

$$r(t) = r(0)e^{-\frac{t}{\theta_R}}$$ (10)

where θ_R is axial rotational correlation time.[90] In the limit of "stick" diffusion of an ellipsoidal molecule, we can determine the rotational correlation time with

$$\theta_R = \frac{V\eta}{kT} \cdot f(a,b,c)$$ (11)

where V is the volume of the molecule, η is the solvent viscosity, a, b and c are the ellipsoidal radii of the molecule and the function, $f(a,b,c)$, subsumes all the shape dependence of the correlation time. The initial fluorescence anisotropies, $r(0)$, of between –0.1 and –0.05 were all significantly less than the expected value of –0.2 for a chromophore whose absorption transition dipole is perpendicular to the emission transition dipole, as is the case for 391 nm excitation of PDI into its S_2 state. This is most likely due to a change in the relative angle between the S_1 and S_2 transition dipoles from 90° to between 60 and 66° in this highly substituted perylene.[90] At room temperature, θ_R changes linearly with estimated molecular volume, increasing from 0.40 ns in the PDI monomer, to 0.56 ns in **3** and finally to 0.71 ns in **5**, Table 2.3.

Table 2.3. Rotational correlation times as deduced by Time Resolved Fluorescence

Compound	T (K)	V (Å^3)^a	η (cP)^b	θ_R (ns)
PDI	298	981	0.56	0.40 ± 0.03
3	298	1410	0.56	0.56 ± 0.03
5	298	1770	0.56	0.71 ± 0.06
5	230	1770	1.73	1 ± 0.6 (40%)
				9 ± 9 (60%)
5	207	1770	3.60	8 ± 2
5	184	1770	11.0	12 ± 4

^{a} Molecular volumes are calculated for an ellipsoidal molecule with elliptical radii of 2.5 and 7.5 Å with overall length increasing from 25 to 36 to 45 Å for the PDI monomer to **3** to **5** series.

^{b} Viscosities were calculated according to Assael et al.[91] and Barlow et al.[92]

2.3 Discussion

2.3.1 Radical Pair TREPR Spectra.

An examination of the parameters used to simulate the RP TREPR spectra of **4** and **5**, Table 4.2, shows that *2J* decreases as the temperature decreases. This is readily seen in the spectra as well, Figure 2.5, which narrow as the temperature decreases. We showed earlier that *2J* for **2-4** determined from MFEs on the yield of ^{3*}PDI following RP recombination decreases as the temperature decreases; for example, *2J* for **4** decreases from 8.3 mT at 345 K to 4.7 mT at 218 K.[30] It should be noted that values of *2J* estimated from MFE resonances due to S-T$_{\pm1}$ level-crossings and those determined directly from TREPR data may differ somewhat due to the fact that the energies of the level crossings can depend on the nuclear spin states.[93] Given the error bars on the data for **4** in Figure 2.5 A, the small changes of *2J* with temperature should be viewed with appropriate caution. However, the value of *2J* obtained for **5** at 294 K agrees well with that measured earlier using MFEs and displays a similar decrease with decreasing

temperature. Equation 3 and 6 show that the intensity of the SCRP signal is inversely proportional to *2J*, so that the SCRP signal intensity should increase for these systems as the temperature decreases. The result is that *2J* becomes small enough in **4** and to some degree in **3** for the SCRP to become detectable at low temperatures, but remains too large for detection at room temperature or at shorter RP distances. The inability to observe intense RP signals for **1**-**3** and for **4** at higher temperatures given the shorter RP distances and/or larger *2J* values for these molecules is consistent with this picture.

The decrease in *2J* with decreasing temperature is most likely due to a reduction in the amplitude of torsional motions about the single bonds joining the phenyls of the bridge. This results in relaxation of the system into conformations in which the dihedral angles between the π systems of the phenyls are larger, which diminishes the electronic coupling between them. The fact that aggregation of **1**-**5** occurs as the temperature is lowered may also affect the RP properties. We have shown that π-stacking of PDI molecules can result in electron hopping between the PDIs on the time scale of their hyperfine couplings.[83] Additional electron delocalization in the RP due to π-stacking of two or more PDI molecules may result in smaller values of *2J*. Although aggregation may contribute to the observed decrease in *2J* as the temperature is lowered, this effect cannot be distinguished easily from the decrease that is expected from torsional motions between the Ph groups of the bridge molecules.

It is notable that $k_{TT}^{CR} > k_{SS}^{CR}$ for both **4** and **5** as determined from the simulations of their RP spectra over the range of temperatures measured, Table 4.2. This agrees with our results obtained earlier using MFE measurements on the RP and triplet recombination yields of **4** and **5** (as well as **2** and **3**) at low magnetic field strengths. We have shown previously that the total

reorganization energy, λ, for charge recombination of the RPs within these molecules at room temperature is about 0.6 eV.[29] Spin-selective formation of the ground state by charge recombination from the singlet RPs of **4** and **5**, where $\Delta G_{SS}^{CR} = $ -2.1 to -2.2 eV, lies deep within the Marcus inverted region[94] of the rate vs. free energy profile, while the formation of the corresponding local triplet state from the triplet RPs, where $\Delta G_{TT}^{CR} = $ -0.9 to -1.0 eV, is much closer to the peak of the rate vs. free energy profile. Thus, energy gap considerations alone predict that k_{TT}^{CR} should be larger than k_{SS}^{CR}. Both k_{SS}^{CR} and k_{TT}^{CR} change by less than a factor of three over the entire range of temperatures measured. These small changes, which are just outside the error bars on the data, cannot easily be attributed to a single source. For example, over this large temperature range, ΔG_{SS}^{CR}, ΔG_{TT}^{CR}, λ, undoubtedly change. In addition, the electronic coupling matrix elements for charge recombination also change, as indicated by the fact that *2J* is temperature dependent.

2.3.2 Triplet State TREPR Spectra resulting from RP-ISC.

The fluorescence quantum yield of PDI is approximately unity,[95] so that the yield of ^{3*}PDI produced directly from the photoexcited singlet state, ^{1*}PDI, via SO-ISC is insignificant. In fact, triplet EPR spectra have not been observed for any monomeric PDI derivatives following direct photoexcitation. The formation of π-stacked *H*-aggregates of chromophores sometimes leads to enhanced intersystem crossing;[96] however, we have examined model covalent, cofacial PDI dimers,[29] and have found that photoexcitation produces singlet excimer-like states predominantly. Thus, the observation of reasonably intense triplet EPR spectra in **1**-**5** following charge separation in these molecules must be due to mechanisms of ^{3*}PDI formation that depend

in some way on the formation of a RP. A variety of ESP patterns are observed in the triplet state spectra of **1-5**, which depend on both the length of the *p*-phenylene oligomer and the temperature. These patterns provide insights into the triplet formation mechanisms that occur in these molecules.

The ESP pattern (*a,e,e,a,a,e*) of the triplet spectra of PTZ-Ph$_{3-5}$-^{3*}PDI at and above 150 K and of PTZ-Ph$_2$-^{3*}PDI at 200 K uniquely results from RP-ISC, where an intermediate RP, i.e. PTZ$^{+\bullet}$-Ph$_n$-PDI$^{\bullet}$, is required for its realization.[78] In such cases, population of PTZ-Ph$_{2-5}$-^{3*}PDI following charge recombination is selective with respect to the high-field eigenfunctions and not the molecular zero-field eigenfunctions as is the case for SO-ISC. The high-field T$'_0$ triplet sublevel is overpopulated at all canonical orientations, and the ESP patterns are preserved within a particular transition, i.e., T$'_0 \leftrightarrow$ T$'_1$ or T$'_0 \leftrightarrow$ T$'_{-1}$, Figure 2.3B.[97-99] The observed (*a,e,e,a,a,e*) ESP pattern seen at higher temperatures in **2-5** requires that the triplet zero field splitting parameter $D > 0$. Although this same ESP pattern can be formed if $D < 0$ and selective overpopulation of T$'_{\pm1}$ occurs, the latter is unlikely given that $|2J| \ll g\beta\mathbf{B}$ for **2-5** at the temperatures at which ^{3*}PDI is observed. The triplet spectra of PTZ-Ph$_{2-5}$-^{3*}PDI above 150 K and PTZ-Ph$_2$-^{3*}PDI at 200 K in toluene can be accurately simulated with the RP-ISC mechanism making the primary contribution to the line shape relative to the SO-ISC mechanism, Table 2.2. The origin of ^{3*}PDI produced by a SO-ISC mechanism will be discussed in detail below.

An unusual aspect of these systems is the existence of a spin-polarized EPR signal for ^{3*}PDI in the *liquid phase*. Generally, in the liquid phase the anisotropic magnetic dipole-dipole interaction averages to zero and no triplet spectrum is observed.[100, 101] If, however, molecular reorientation is not rapid enough to cause the dipolar contribution to vanish, then a triplet

spectrum may be seen. Recently, Yamauchi et al.[101, 102] suggested that the conditions necessary to observe triplet spectra in fluid solution involve a delicate balance of several parameters, including relatively small ZFS parameters and significant chemically induced dynamic electron polarization (CIDEP). The size of the molecule, and consequently its rotational correlation time, were also found to play an important role in the observation of the triplet spectrum.

The UV-vis absorption spectra of **1**-**5** indicate that these molecules aggregate in toluene at temperatures of 230 K and below, Figure 2.9. We have demonstrated that similar UV-vis spectra occur in covalent, cofacial PDI dimers in which the transition dipoles for the lowest energy transitions in each of the two PDI chromophores, which lie along the N-N axis, are constrained to a parallel orientation.[47] Recent work by Myers-Kelley has modeled the blue-shifted λ_{max} and distorted Franck-Condon progression in related systems, where exciton coupling is treated explicitly for all vibronic levels of the electronic transitions.[89] Unfortunately, the spectra do not indicate the size of the aggregates, nor do they preclude the possibility that any two PDI molecules within the aggregates may deviate somewhat from a strictly cofacial orientation relative to one another to minimize steric interactions.

Since the rotational correlation time for a system is a function of both molecular size and the viscosity of the solvent at a given temperature, it is reasonable to expect aggregates to have longer rotational correlation times than their monomeric constituents. Given that the rate constants for charge separation within **3** and **5** are 6.2×10^8 s^{-1} and 1.3×10^8 s^{-1}, respectively, at 294 K,[29] and the fluorescence lifetime of ^{1*}PDI is intrinsically 4.5 ns, the fluorescence emission of **3** and **5** in toluene is sufficiently long-lived, so that time-resolved fluorescence anisotropy experiments were used to measure their rotational correlation times. Data for **5** were obtained as

a function of temperature down to a range at which some of the TREPR data is obtained,

Table 2.3. The rotational correlation time depends on the molecular volume, Equation 11, so

that the larger size of an aggregate should be reflected in an increase in the fluorescence

anisotropy decay time, Equation 10. At 230 K, the anisotropy exhibits a bi-exponential decay

with a fast decay of ~1 ns probably due to the monomer, and a longer ~ 9 ns decay most likely

due to an aggregated species. The accuracy of the low-temperature anisotropies is hampered by

the relatively large standard deviations in the data due to the inherent difficulty of measuring ~12

ns anisotropy decays for a molecule with a shorter fluorescence lifetime. The anisotropy of **5**

decays with single exponential kinetics at 207 K with a time-constant of ~8 ns, and then

increases to ~12 ns at 184 K. Presumably, at these lower temperatures, the long mono-

exponential anisotropy decay is due largely to the aggregate. The low-temperature rotational

correlation times are shorter than expected for an aggregated species given the potential for

significant changes in V, η, and T in Equation 11; however the large error-bars associated with

these measurements preclude a full discussion of the significance and quantification of the

rotational correlation times. However, in purely qualitative terms, rotational correlation times of

~ 10 ns are significantly slower than the inverse of the frequency (~ 1 ns) that corresponds to the

energy of the dipolar interaction D in the triplet states of these molecules. Thus, the triplet

TREPR spectra observed in liquid toluene are a result of slowed molecular reorientation to the

point where the dipolar interaction is no longer averaged out. Although aggregation occurs, the

D and E values of PTZ-Ph$_{2\text{-}5}$-^{3*}PDI do not change significantly as the temperature decreases

either within one system or in one system relative to another. Thus, it is unlikely that the triplet

excitation in PTZ-Ph$_{2\text{-}5}$-^{3*}PDI is either delocalized or hopping between PDI molecules within the

aggregates at frequencies that are comparable to or faster than those that correspond to D (~ 1 GHz).

2.3.3 Triplet State TREPR Spectra resulting from SO-ISC.

As either the RP distance or the temperature decreases, the fraction of the triplet state TREPR spectrum due to the RP-ISC mechanism diminishes, while that due to a SO-ISC mechanism increases, Table 4.2. Given that direct ^{1*}PDI $\rightarrow$ ^{3*}PDI by SO-ISC is negligible, RP formation is most likely responsible for SO-ISC leading to PTZ-Ph$_{1-5}$-^{3*}PDI. If the orientation between the relevant orbitals of D and A is such that rapid electron transfer between them results in a significant change in orbital angular momentum, recombination of ^{1}(D$^{+\bullet}$-B-A$^{\bullet}$) may be accompanied by a spin flip to directly yield ^{3*}(D-B-A).[63, 65, 66] In this case the spin-orbit interaction does not result in ^{1}(D$^{+\bullet}$-B-A$^{\bullet}$) $\rightarrow$ ^{3}(D$^{+\bullet}$-B-A$^{\bullet}$) because $\langle^{1}$(D$^{+\bullet}$-B-A$^{\bullet}$)$|$ $\mathcal{H}_{SO}$ $|$ ^{3}(D$^{+\bullet}$-B-A$^{\bullet}$)$\rangle$ = 0, due to the fact that there is no change in the spatial orbital for this process.[103] Okada et al.[63] originally proposed this mechanism to explain the formation of a pyrene triplet state within 30 ps following photoexcitation of pyrene to its lowest excited singlet state in a covalently-linked pyrene-N-methylaniline derivative. The rapid rate of pyrene triplet state formation precluded the RP-ISC mechanism, which typically occurs on a timescale of a few nanoseconds. They found that the ISC rate was strongly dependent upon the mutual orientation of the donor and acceptor groups and concluded that $\langle^{1}$(D$^{+\bullet}$-B-A$^{\bullet}$) $|$ $\mathcal{H}_{SO}$ $|$ ^{3*}(D-B-A)$\rangle$ is increased when the electron donating and accepting molecular orbitals are approximately perpendicular to each other. This mechanism is formally similar to rapid SO-ISC that occurs in an n-π^{*} electronic transition within a single chromophore.

Wasielewski et al.[64] studied a zinc porphyrin electron donor to which a tetracyano-naphthoquinodimethane acceptor was rigidly attached so that the π systems of the donor and acceptor were oriented approximately 60° relative to one another. Photoexcitation of this system at 10 K results in quantitative electron transfer from the porphyrin to the acceptor with $\tau = 2.2$ ps to produce a radical ion pair that recombines in about 0.5 ns to give a high yield of the zinc porphyrin triplet state having a TREPR spectrum with an ESP pattern indicative of SO-ISC to the in-plane sublevels of the zinc porphyrin. In contrast, photoexcitation of the zinc porphyrin in the absence of the acceptor produces a porphyrin triplet state in which the out-of-plane sublevel is populated exclusively. Similarly, van Willigen et al.[65] used TREPR to provide convincing evidence that this same mechanism is operative in 10-methylacridinium systems having arene electron donors attached to their 9-position. The ZFS parameters were found to remain essentially constant, whereas the ESP phase pattern was a sensitive function of the orientation of the donor and acceptor ring systems. Their analysis also indicated that, similar to the analysis of Okada et al.,[63] an approximately perpendicular orientation of the donor and acceptor enhanced the rate of SO-ISC. This was reflected in the triplet EPR spectra as an orientation dependent spin selectivity of the population rates A'_x, A'_y, and A'_z. In a more recent example, Gould et al.[66] analyzed rapid intersystem crossing in a series of exciplexes between cyanoanthracene acceptors and alkylbenzene donors and concluded that rapid SO-ISC results in direct population of the excited cyanoanthracene triplet from the singlet exciplex.

In addition to the dependence on orientation between the orbitals relevant to charge transfer, the magnitude of the electronic coupling between D and A strongly influences the contribution from the SO-ISC process.[64, 66, 67, 104-106] The value of *2J* for the RP in **1** is at least

800 mT as estimated from an extrapolation of a linear plot of $\ln(|2J|)$ vs. r_{DA} obtained from

the measured MFEs for **2-5**,[29] so that $|2J| \gg g\beta\mathbf{B}$ for **1** and the yield of ^{3*}PDI resulting from RP-

ISC approaches zero because the large energy gap between singlet and triplet RP states prohibits

significant mixing. The TREPR spectrum of ^{3*}PDI in **1** is not observed in fluid solution. This is

a consequence of the fact that **1** is the smallest molecule of the series and most likely has the

fastest rotational correlation time in liquid toluene. However, an intense ^{3*}PDI spectrum is

observed for **1** at temperatures ≤ 150 K, Figure 2.7. Simulations of the ^{3*}PDI TREPR spectra of

1 agree well with the experimental results at 150 K and 40 K, however at 125 K and 80 K, the

simulations deviate somewhat from experimental results for the outermost transitions. It is likely

that anisotropic spin lattice relaxation is the cause of the deviations and further modeling is

needed to clarify this result.

In aromatic molecules such as PDI, the triplet axis system usually coincides with the

lowest electronic transitions and is clearly dictated by the molecular structure.[104, 107, 108]

Although we have not assigned the principal triplet molecular axes of ^{3*}PDI experimentally, it is

reasonable to assume that the z-axis is the out-of-plane axis, as is typical of π-π^* triplets of

aromatic molecules, which leaves the x and y axes in the plane of ^{3*}PDI.[109-111] In our

simulations, the central zero-field sub-level is assigned to T$'_Y$, Figure 2.3A, and the observed

(*e,a,e,a,e,a*) ESP pattern for **1** is indicative of a SO-ISC mechanism with selective population of

T$'_Y$ for $D > 0$.[99, 112]

Density functional theory (DFT) calculations using the B3LYP functional and 6-31G**

basis set show that the nitrogen atom of PTZ is essentially tetrahedral and the dihedral angle

between the nitrogen lone pair orbital of PTZ and the π system of the attached Ph in the energy-

minimized structure of **1** is 89°, while that between PDI and Ph is 74°.[29]   Thus, electron

transfer from PTZ to ^{1*}PDI involves moving an electron between two orbitals having a geometry

change in the x-z plane as defined in Figure 2.10. Using the right hand rule, this implies that the

angular momentum change is along the y direction, so that the spin orbit interaction that drives

^{1}(PTZ$^{+\bullet}$-Ph$_1$-PDI$^{\bullet}$) $\rightarrow$ PTZ-Ph$_1$-^{3*}PDI should selectively populate T$'_Y$ of PTZ-Ph$_1$-^{3*}PDI as is

observed in the TREPR spectra of the triplet state of **1**.[113, 114] An additional contribution to spin-

orbit coupling may arise from the presence of the sulfur atom in PTZ cation, i.e. the heavy atom

effect.[67, 115] However, since calculations indicate that the unpaired spin density at this position is

low, it is unlikely that this contribution will be a significant source of intersystem crossing.

At temperatures above 150 K, the ESP phase pattern in PTZ-Ph$_{2-5}$-^{3*}PDI is primarily the

result of S-T$_0$ mixing resulting from RP-ISC, but at 125 K and below, the ESP phase pattern for

2-5 changes to (*e,e,e,a,a,a*), Figure 2.6. Simulations of the PTZ-Ph$_{2-5}$-^{3*}PDI TREPR spectra at

low temperatures using a linear combination of the RP-ISC mechanism in addition to a SO-ISC

mechanism with approximately equal population of the zero field T$'_X$ and T$'_Y$ eigenstates agrees

well with experiment (see Figure 2.6A-80K and Table 2.2). This observation can be explained

by reference again to Figure 2.10. The Ph-Ph torsional angles in **2-5** are all about 40° in the

neutral bridge molecule and diminish to about 25° if the bridge is oxidized.[29] These torsional

angles result in a change in the dihedral angle between the PDI π system and the nitrogen lone

pair orbital of PTZ, so that angular momentum changes occur in both the x and y directions

following electron transfer. Since spin-orbit coupling matrix elements are inherently symmetry

dependent,[104, 105, 114] these components result in selective population of both T$'_X$ and T$'_Y$ for **2-5**,

which produces the observed (*e,e,e,a,a,a*) ESP pattern seen at 125 K and below in the TREPR

spectra.   The increase in the fraction of PTZ-Ph$_{2-5}$-^{3*}PDI produced by direct charge recombination from the singlet RP (k_{ST}^{CR}, Figure 2.2A) as the temperature decreases is most likely due to a decrease in the amplitudes of the torsional motions about Ph-Ph single bonds. This results from the large increase in toluene viscosity as the temperature is lowered,[91, 116] especially in the glassy state below 160 K.[92]   A narrow distribution of large Ph-Ph dihedral angles will promote SO-ISC by the mechanism indicated in Figure 2.10.
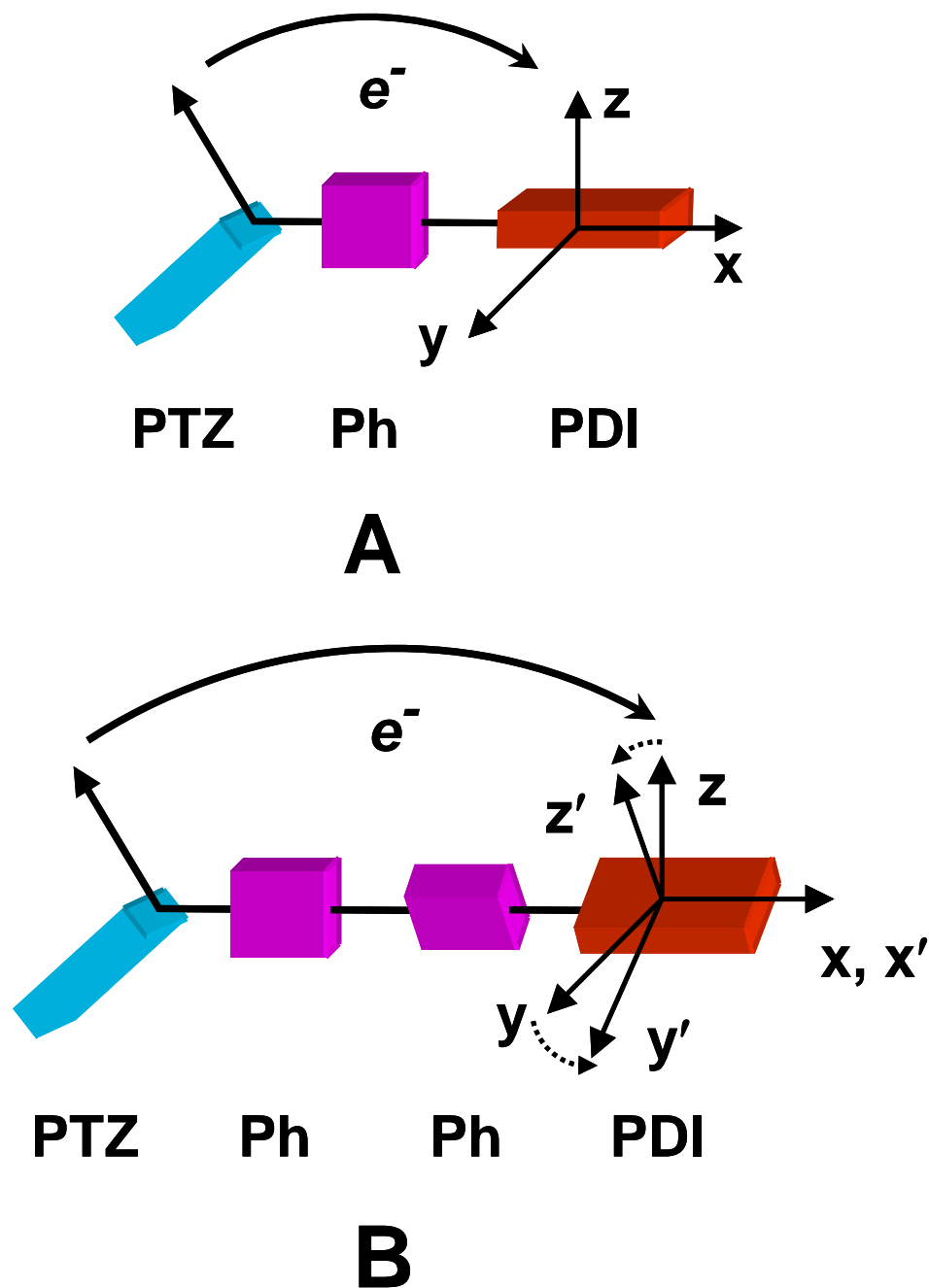
Figure 2.10. A) Electron transfer from PTZ to ^{1*}PDI in PTZ-Ph$_1$-PDI between orbitals oriented in the x-z plane results in an angular momentum change along y. B) Rotation of the PDI π system away from the x-z plane in PTZ-Ph$_{2-5}$-PDI due to changes in the Ph-Ph torsional angles results in an angular momentum change in both the x and y directions. These angular momentum changes result in SO-ISC to the corresponding spin sub-levels of ^{3*}PDI.

2.3.4 Conclusions

TREPR studies show that the spin dynamics of both photogenerated RPs and the neutral local triplet states that result from RP charge recombination are a strong function of both RP distance and temperature in the PTZ-Ph$_n$-PDI series, where n = 1-5. Above 150 K, when n =1, the RP lifetime is too short to observe by TREPR. In addition, $|2J| \gg g\beta\mathbf{B}$, so that the RP-ISC cannot occur. In contrast, above 150 K, when n = 2-5, the lifetimes of the RPs are sufficiently long and $|2J| \ll g\beta\mathbf{B}$, so that RP-ISC via S-T$_0$ mixing occurs, which produces a spin correlated radical pair. Charge recombination leads to PTZ-Ph$_{2-5}$-^{3*}PDI, which exhibit the unique ESP pattern seen in the photosynthetic reaction center that is the signature of the RP-ISC mechanism. Aggregation of PTZ-Ph$_n$-PDI molecules below 230 K combined with increasing solvent viscosity slows molecular reorientation and allows EPR detection of PTZ-Ph$_n$-^{3*}PDI in liquid solution. Below 150 K, when n = 1-5, a rapid SO-ISC mechanism where ^{1}(PTZ$^{+\bullet}$-Ph$_{1-5}$-PDI$^{\bullet}$) $\rightarrow$ PTZ-Ph$_{1-5}$-^{3*}PDI competes with RP-ISC. This SO-ISC mechanism is characterized by the ESP phase patterns of the PTZ-Ph$_{1-5}$-^{3*}PDI TREPR spectra, and depends on the relative orientation of the orbitals involved in the charge recombination as well as the magnitude of the electronic coupling between the donor and acceptor, mirrored by $2J$. These results reveal the considerable level of structurally-dependent mechanistic complexity responsible for charge and spin transport within conjugated oligomers, and provide insights into how their structures may be controlled to enhance their properties of interest to solar energy conversion.

Chapter 3

Direct Observation of Bridge-mediated Hole Transfer: Time-Resolved

EPR Studies of Radical Pair Spin Dynamics and Intramolecular Triplet-

Triplet Energy Transfer in Donor-Bridge-Acceptor Molecules

3.1 Introduction

Understanding how the electronic structures of electron donor-bridge-acceptor (D-B-A) molecules influence the lifetimes of radical ion pairs (RPs) photogenerated within them (D$^{+\bullet}$-B-A$^{-\bullet}$) is critical to developing molecular systems for solar energy conversion. A general question that often arises is whether the HOMOs or LUMOs of D, B, and A within D$^{+\bullet}$-B-A$^{-\bullet}$ are primarily involved in charge recombination. If this information is available, molecular structures with properly adjusted energy levels and electronic couplings between states involving these orbitals can be designed to significantly slow energy-wasting charge recombination rates. We have reported on related D-B-A molecules where both photoinduced charge separation and RP recombination most likely involve charge transfer via the HOMOs of D, B, and A (i.e. hole transfer).[45, 117] Those D-B-A systems consist of a series of either oligo-p-phenylenes (Ph$_n$) or oligofluorenes that link a phenothiazine (PTZ) electron donor to a perylene-3,4:9,10-bis(dicarboximide) (PDI)[47] electron acceptor (i.e., PTZ-B-PDI). Using transient optical absorption spectroscopy and optically-detected magnetic field effects (MFEs) on charge recombination it was shown that selective photoexcitation of the acceptor (PDI) within PTZ-B-PDI results in charge separation to produce a spin-coherent singlet radical ion pair (RP), ^{1}(PTZ$^{+\bullet}$-B-PDI$^{-\bullet}$).[117] In the case of PTZ-Ph$_n$-PDI, the energies of PTZ$^{+\bullet}$-Ph$_n^{-\bullet}$-PDI are $\geq$ 3.0 eV above the respective ground states (and $\geq$ 1.0 eV above their respective PTZ$^{+\bullet}$-Ph$_n$-PDI$^{-\bullet}$ states), so that electron injection onto the bridge is very improbable, and charge recombination likely proceeds by hole transfer through the bridge. However, to our knowledge, there is no direct evidence from any D-B-A system that hole transfer is the favored mechanism of charge recombination.

To this end, we have recently developed and reported on a new series of D-B-A molecules, which uses a photogenerated charge transfer (CT) state as a high-potential photoreductant to rapidly and nearly quantitatively transfer an electron across an oligo-*p*-phenylene bridge to produce a long-lived RP. Time-resolved EPR (TREPR) spectroscopy shows directly that charge recombination of the RP initially produces a spin-polarized triplet state that can *only* be produced by hole transfer involving the HOMOs of D, B, and A within the D-B-A system. The D-B-A system, Figure 3.1, consists of a 3,5-dimethyl-4-(9-anthracenyl)julolidine (DMJ-An) electron donor linked to a naphthalene-1,8:4,5-bis(dicarboximide) (NI) acceptor via a series of Ph_n oligomers, where $n = 1$-4, to give DMJ-An-Ph_n-NI, **1-4**. DMJ-An is modeled after well-known 4-(9-anthryl)-*N,N*-dimethylaniline (ADMA) derivatives,[118] but is tailored to produce a high energy CT excited state that can serve as a good reductant by minimizing molecular motions in the excited state. The nitrogen lone pair in julolidine is conformationally restricted to be parallel to its benzene ring π system, resulting in an electron donor with a reversible oxidation potential of 0.63 V vs. SCE, while the methyl groups at the 3 and 5 positions of julolidine strongly constrain its π system to ~90° relative to that of the anthracene.

DMJ   An   Ph   NI
1 - 4 (n = 1-4, respectively)
1-3: R = n-C_8H_{17} ; **4**: R = 2,5-di-t-butylphenyl
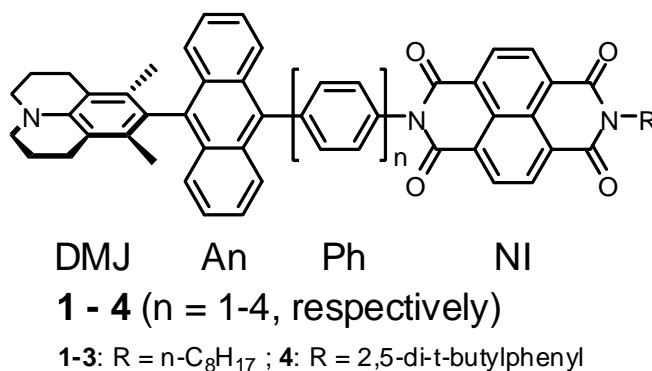
Figure 3.1. Chemical structure of DMJ-An-Ph_n-NI where $n = 1$ for compound 1, $n = 2$ for compound 2, etc.

Following photoexcitation, when the RP distances in $D^{+\bullet}$-B-$A^{-\bullet}$ are > ~15Å, the spin-spin exchange interaction, *2J*, is generally <10 mT. Under these conditions electron-nuclear hyperfine coupling drives radical pair-intersystem crossing (RP-ISC), which mixes the singlet (S) and triplet (T_0) states within the RP: $^1(D^{+\bullet}$-B-$A^{-\bullet}) \leftrightarrow {}^3(D^{+\bullet}$-B-$A^{-\bullet})$.[13, 74, 75, 119] The resultant spin-correlated RP states can be identified through the unique polarization of the EPR transitions that occur between them.[70, 71] The mechanistic details of RP-ISC and the theory behind magnetic field effects on electron transfer reactions have been researched extensively[13, 48-51] and have been applied to many donor-acceptor systems[43, 44, 52-57, 117] The subsequent charge recombination process is spin selective; i.e. the singlet RP $^1(D^{+\bullet}$-B-A) recombines to the singlet ground state D-B-A with a rate constant k_{SS}^{CR}, while the triplet RP $^3(D^{+\bullet}$-B-$A^{-\bullet})$ recombines to yield the neutral local triplet ^{3*}(D-B-A) with a rate constant k_{TT}^{CR}, Figure 3.2A. In addition, the non-Boltzmann spin populations within $^3(D^{+\bullet}$-B-$A^{-\bullet})$ are transferred to the neutral triplet state ^{3*}(D-B-A) during recombination.[78, 120] Application of a magnetic field results in Zeeman splitting of the RP triplet sublevels, which at low fields are best described by the zero-field eigenstates, T_X, T_Y, and T_Z that are quantized in the molecular framework, and at high fields by the T_{+1}, T_0, and T_{-1} eigenstates that are quantized along the applied magnetic field.
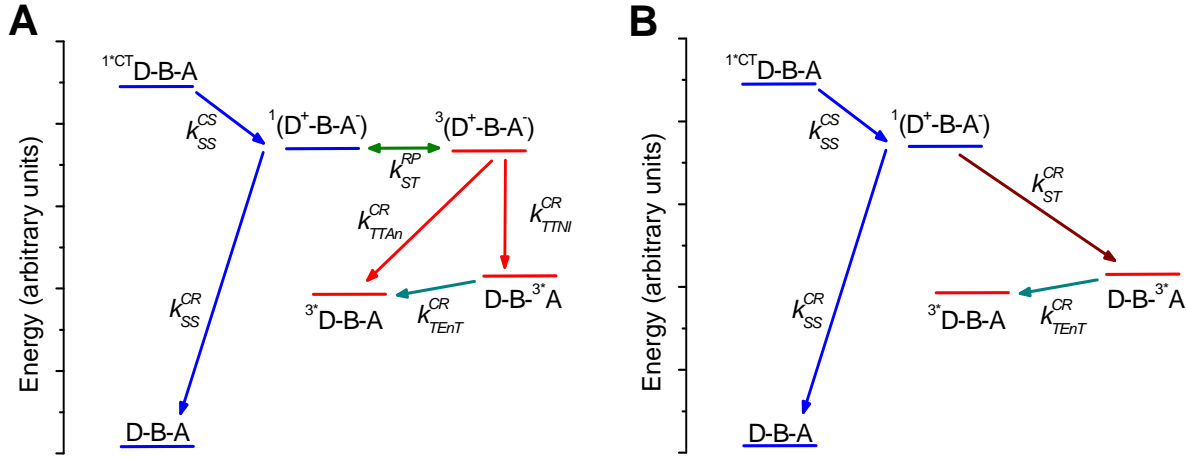
Figure 3.2. Charge transfer, energy transfer, and intersystem crossing pathways in A) **2-4** and B) **1**.

Alternatively, when the RP distances decrease to lengths such that $|2J| \gg g\beta\mathbf{B}$, RP-ISC is effectively inhibited. However, rapid intersystem crossing from the singlet radical pair may take place via a spin-orbit coupling mechanism to produce ^{3*}(D-B-A) directly by charge recombination, k_{SS}^{CR}, Figure 3.2B, provided that the symmetries of the orbitals involved in the electron transfer are such that the spin flip is coupled to a significant change in orbital angular momentum.[63-67] This mechanism will be discussed in more detail in the Discussion section.

Analogous to the RP triplet, the presence of a magnetic field splits the sublevels of ^{3*}(D-B-A), Figure 3.3. The main features of the EPR spectrum of ^{3*}(D-B-A) arise from zero-field splitting (ZFS), which is a result of the magnetic dipole-dipole interaction between the two unpaired electrons in the triplet state. The Hamiltonian that describes this interaction is:[79-82]

$$\mathcal{H}_{\text{dipolar}} = D(\mathbf{S}_{\mathbf{z}}^2 - \mathbf{S}^2/3) + E(\mathbf{S}_{\mathbf{x}}^2 - \mathbf{S}_{\mathbf{y}}^2) \tag{1}$$

where D and E are the zero-field-splitting parameters and $\mathbf{S}_{\mathbf{x,y,z}}$ are the components of the total spin angular momentum operator (S) for the triplet state. The effect of this interaction is to lift

the degeneracy of the triplet manifold in the absence of an external magnetic field as a function of the symmetry of the molecule. The polarization of the EPR transitions exhibited by ^{3*}(D-B-A) formed by the RP-ISC mechanism can be differentiated from those formed by a spin-orbit intersystem crossing (SO-ISC) mechanism by the electron spin polarization (ESP) pattern of the six EPR transitions, i.e. the two transitions at each canonical (x, y, z) orientation.[78] RP-ISC acts directly on the high-field triplet sublevels of the RP via S-T_0 (or S-$T_{\pm1}$) mixing, Figure 3.3B. The six EPR transitions from low to high field yield an (*a,e,e,a,a,e*) polarization pattern, (where *a* = enhanced absorption and *e* = emission) which results exclusively from the RP-ISC mechanism.[120] Comparatively, in SO-ISC, the three zero-field levels T′$_X$, T′$_Y$, and T′$_Z$ of ^{3*}(D-B-A) are selectively populated and this selectivity is carried over to the high field energy levels. For example, assuming selective population of the T′$_Y$ zero-field level and $D > 0$, Figure 3.3A the triplet spectrum exhibits an (*e,a,e,a,e,a*) ESP polarization pattern.
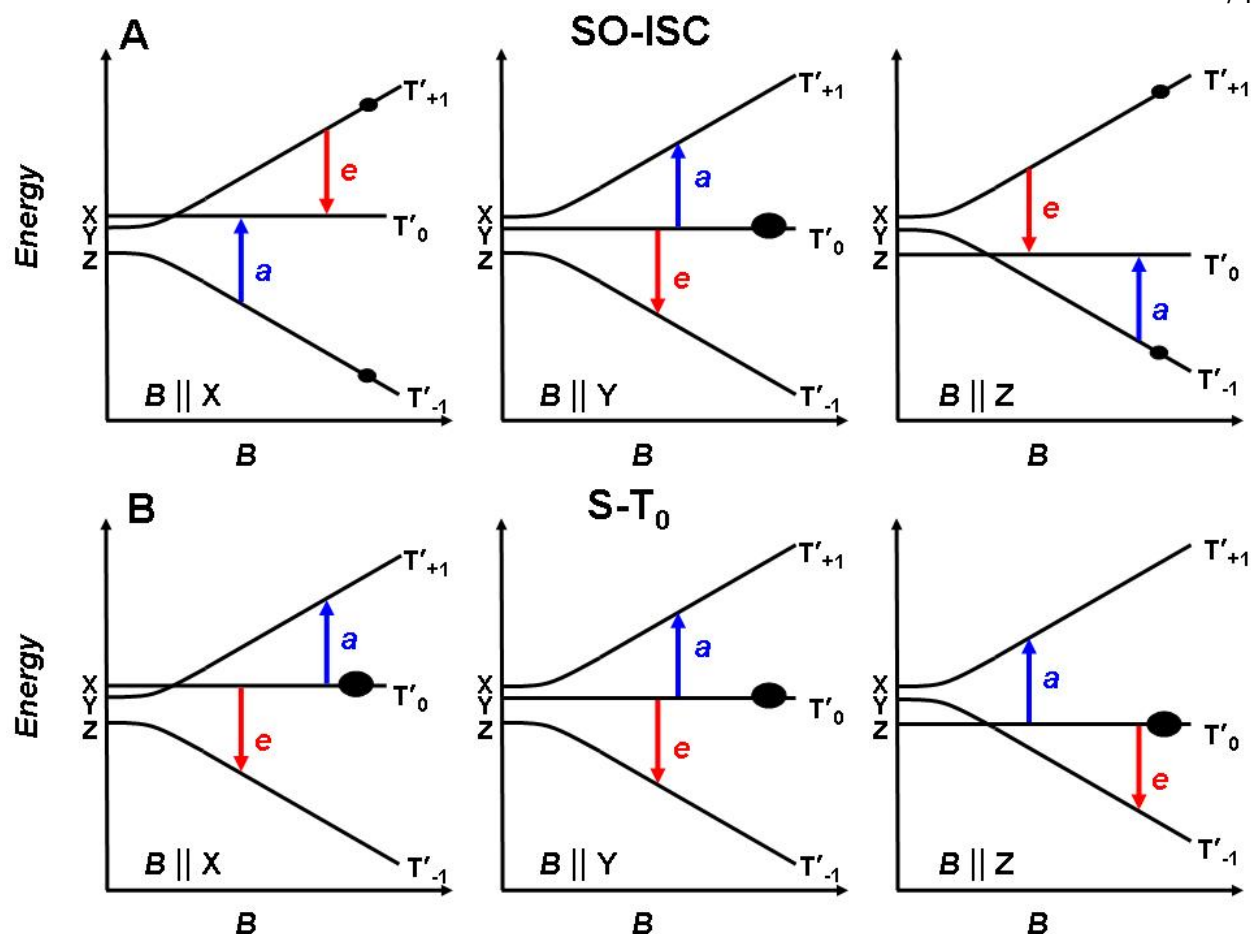
Figure 3.3. Energy levels of ^{3*}(D-B-A) formed by (A) SO-ISC with selective population of T$'_Y$ ($D > 0$, $E < 0$) and (B) S-T$_0$ mixing within a radical pair precursor. The arrows indicate the direction of the transition and are labeled a = enhanced absorption, e = emission.

3.2 Results

3.2.1 Electron Transfer Reaction Energetics

The distances between the donor, bridge, and acceptor components were determined from the energy minimized structures of DMJ-An-Ph$_n$-NI determined using semi-empirical RHF-PM3 and UHF-PM3 electronic structure calculations.[121] These data are given in Table 3.1. Direct excitation of DMJ-An produces DMJ$^{+\bullet}$-An$^{-\bullet}$, which has a measured energy of E_{CT} = 2.89 eV in toluene, so that the energies of the ion pairs produced by subsequent electron transfers can be

calculated from the corresponding changes in redox potentials and the change in Coulomb

energies as the distances between the ion pairs change:[74]

$$\Delta G_F = \Delta G_I + sign(E_I - E_F) + \frac{e^2}{\varepsilon_S}\left(\frac{1}{r_I} - \frac{1}{r_F}\right) \quad \text{if } |E_F| > |E_I|, \text{then } sign = (-);$$

$$\text{if } |E_I| > |E_F|, \text{then } sign = (+)$$

where ΔG_I and ΔG_F are the energies above ground state for the initial and final ion pairs,

respectively, E_I and E_F are the redox potentials for the initial and final ions, respectively,

between which the electron is transferred, r_I and r_F are the initial and final ion pair distances,

respectively, e is the electronic charge, and ε_S is the static dielectric constant of the solvent (ε_S =

2.38 for toluene[122]). The one-electron oxidation potentials for DMJ, Ph, Ph_2, Ph_3, and Ph_4 are

0.63, 2.4, 1.85, 1.60, and 1.47 V vs. SCE, respectively.[123] The one-electron reduction potentials

for NI,[124] Ph, Ph_2, Ph_3, and Ph_4 are -0.53, -3.35, -2.68, -2.40, and -2.28 V vs. SCE,

respectively.[123] The results of these ion pair energy calculations are given in Table 3.1.

Table 3.1. Ion pair distances and energies for **1-4**

Compound	$r_{\text{An-NI}}$ (Å)	$r_{\text{DMJ-NI}}$ (Å)	$r_{\text{DMJ-Ph}}$ (Å)	$r_{\text{Ph-NI}}$ (Å)	$-\Delta G_{\text{DMJ+NI-}}$ (eV)	$-\Delta G_{\text{DMJ+Ph-}}$ (eV)	$-\Delta G_{\text{Ph+NI-}}$ (eV)
1	10.4	15.8	9.6	6.2	2.16	4.73	3.34
2	14.7	20.1	11.8	8.3	2.24	4.18	3.03
3	19.0	24.4	13.8	10.6	2.29	3.97	2.94
4	23.4	28.8	16.1	12.7	2.33	3.92	2.90

3.2.2 Radical Pair TREPR Spectra

The lowest excited singlet CT state energy of DMJ-An in toluene, obtained by averaging the energies of its CT absorption and emission maxima at 367 and 519 nm, respectively, is 2.89 eV, while the lifetime of this state measured by time-resolved fluorescence spectroscopy[13] is $\tau =$ 45 ns. Solvatochromism of the CT emission maximum strongly suggests that charge separation is essentially complete to give DMJ$^{+\bullet}$-An$^{-\bullet}$, whereby An$^{-\bullet}$ serves as an electron donor to NI in **1-4** (E_{RED} (An) = -1.97 V[125] and E_{RED} (NI) = -0.53 V[124] vs. SCE). The rate constants for charge separation (k_{CS}) and recombination (k_{CR}) were obtained by transient absorption spectroscopy[117] following selective photoexcitation of the CT band in **1-4** with 416 nm, 120 fs (k_{CS}) and 7 ns (k_{CR}) laser pulses, respectively. The charge separation reactions for **1-4**: ^{1}(DMJ$^{+\bullet}$-An$^{-\bullet}$-Ph$_n$-NI) $\rightarrow$ ^{1}(DMJ$^{+\bullet}$-An-Ph$_n$-NI$^{-\bullet}$) are both rapid and nearly quantitative, resulting in formation of a spin coherent singlet RP. RP-ISC yields spin-polarized RPs which were observed for **2-4** at 293 K and 85 K indicating that charge transfer still occurs efficiently at low temperature. The RP lifetime for **1** is too short to observe by TREPR. The RP spectra of **2-4** were simulated with the SCRP mechanism using the model of Till and Hore which accounts for the fact that the singlet and triplet RP states generally recombine with different rates, i.e., $k_{SS}^{CR} \neq k_{TT}^{CR}$.[50] The best fits to

the data are given in Figure 3.4, while the fitting parameters are summarized in Table 3.2. The

calculated[126, 127] hyperfine coupling constants of DMJ$^{+\bullet}$-An, Figure 3.5, as well as the measured

g-factor and hyperfine coupling constants of NI$^{-\bullet}$ were used in the simulations. The ESP pattern

of the EPR signal, i.e. which transitions are in enhanced absorption (A) or emission (E), is

determined by the SCRP sign rule,

$$\Gamma = \mu \cdot \text{sign}[J - D(3 \cos^2 (\xi) - 1)] = (-) \text{ gives E/A or } = (+) \text{ gives A/E} \tag{2}$$

where μ is -1 or +1 for a singlet or triplet excited state precursor, respectively, and ξ is the angle

between the dipolar axis of the radical pair and the direction of the magnetic field **B**. Given that

photoexcitation initially produces a singlet RP, and that the experimentally determined absolute

phases of the RP spectra are E/A,[85, 86] it follows from Eqn. 2 that $2J$ is positive for the RPs at all

temperatures. The dipolar interaction between the electron spins in **2-4** is ≤ 0.3 mT due to the

long RP distances[77].

Table 3.2. RP simulation parameters for **2-4**

Compound	T(K)	$2J$(mT)	k_{SS}^{CR} (s^{-1})	k_{TT}^{CR} (s^{-1})	Delay(ns)
2	293	30 ± 3	1.7 ± 0.5 x 10^7	3.5 ± 0.5 x 10^6	140
2	125	1.7 ± 1.1	1.9 ± 0.2 x 10^7	1.5 ± 0.1 x 10^7	140
3	293	4.7 ± 0.3	2.6 ± 0.1 x 10^7	1.2 ± 0.1 x 10^7	200
3	85	1.0 ± 0.2	1.4 ± 0.3 x 10^7	1.9 ± 0.3 x 10^7	200
4	295	0.86 ± 0.1	1.7 ± 0.3 x 10^7	1.2 ± 0.3 x 10^7	300
4	85	0.81 ± 0.1	1.2 ± 0.3 x 10^7	1.5 ± 0.3 x 10^7	300
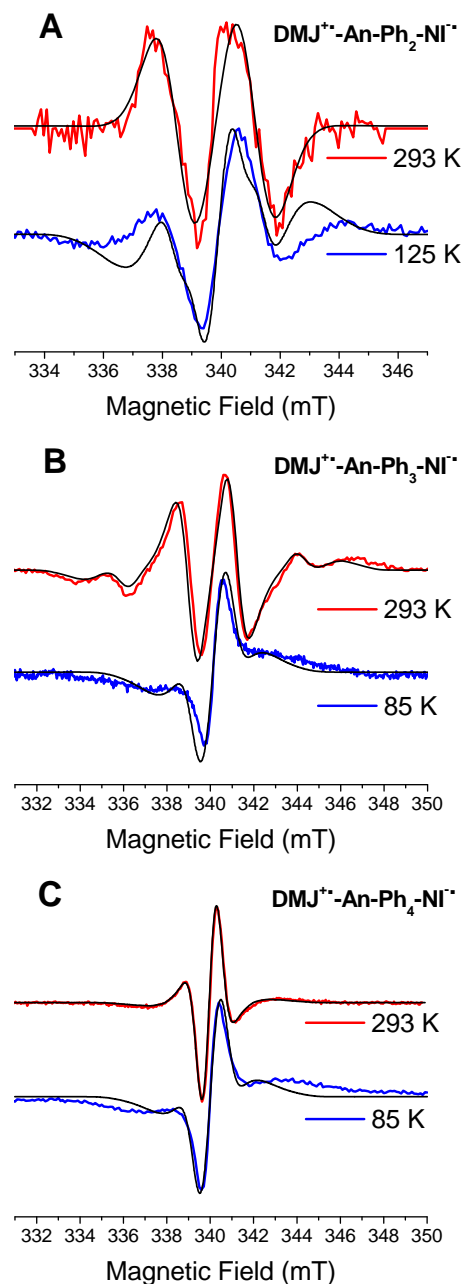
Figure 3.4. TREPR spectra of (A) DMJ$^{+\bullet}$-An-Ph$_2$-NI$^{-\bullet}$ at 140 ns, (B) DMJ$^{+\bullet}$-An-Ph$_3$-NI$^{-\bullet}$ at 200 ns, and (C) DMJ$^{+\bullet}$-An-Ph$_2$-NI$^{-\bullet}$ at 300 ns following a 416 nm, 1.5 mJ laser pulse at the indicated temperatures in toluene. Smooth curves superimposed on the experimental spectra are computer simulations of the radical pair spectra (see text) with the parameters given in **Table 3.2**. Positive features are in enhanced absorption, while negative features are in emission.
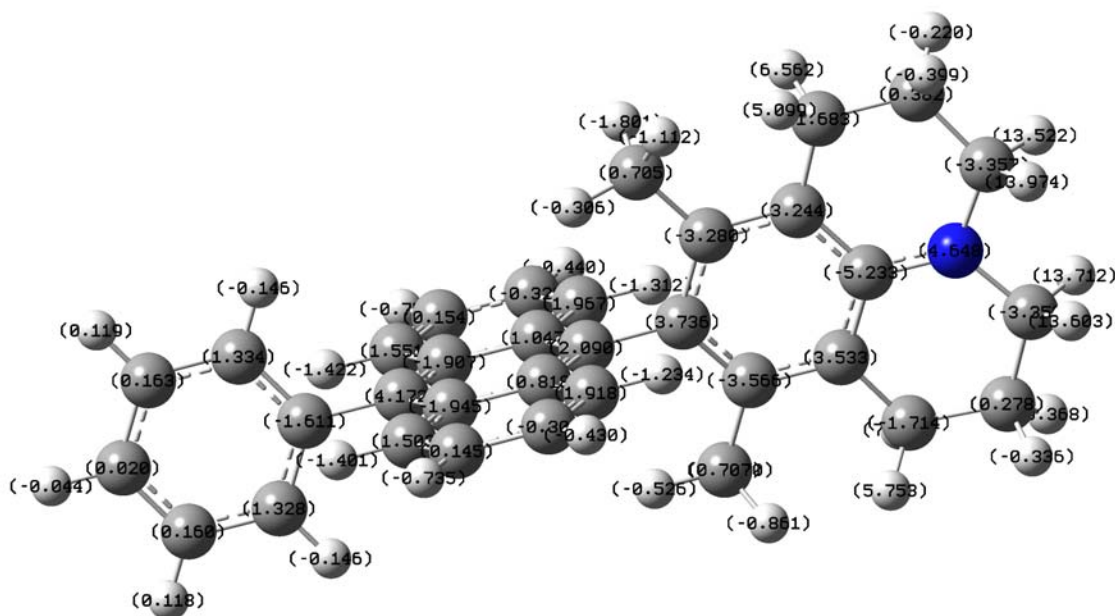
Figure 3.5. Calculated hyperfine coupling constants (gauss) for **DMJ$^{+\bullet}$-An-tol**.

3.2.3 TREPR Spectra of Triplet States Resulting from Charge Recombination

Upon charge recombination, two overlapping broad triplet spectra with widths of ~150 mT appear in the TREPR spectra of **1-4**. In addition, the narrow RP spectrum at g ~ 2, which was discussed above, is superimposed on the triplet spectra. Figure 3.6 shows spectra for **2-4** having (*a*,*e*,*e*,*a*,*a*,*e*) ESP phase patterns, whereas Figure 3.7 shows spectra of **1** exhibiting an (*e*,*e*,*a*,*e*,*a*,*a*) phase pattern. The overlapping triplet states have zero field splittings that identify them as ^{3*}An and ^{3*}NI having energies of 1.8 eV[128] and 2.0 eV,[129] respectively, Figure 3.6D and Table 3.3. The TREPR spectra of **1** are very different from those of **2-4**, and are characteristic of a SO-ISC mechanism of formation. The time-resolved data clearly show that ^{3*}NI is produced

first, even though both ^{3*}An and ^{3*}NI have lower energies than the RPs, Table 3.1. Following

charge recombination to ^{3*}NI, triplet-triplet energy transfer (TEnT) occurs to ^{3*}An with a rate

constant, k_{TEnT}, that decreases as the bridge length increases. The rate constants for TEnT were

calculated according to the equation:

$$k_{TEnT} = 1/\tau - 1/\tau_0 \tag{3}$$

where τ is decay of ^{3*}NI in **2-4** and τ_0 is the decay of ^{3*}NI for a suitable model compound, Figure

3.8.[74]

Table 3.3. Zero-Field Splitting Parameters and Relative Contributions from simulations of the Triplet-State TREPR Spectra of **1-4**

Compound 4

Delay (µs)	D_{An} (mT)[a]	E_{An} (mT)[a]	D_{NI} (mT)[a]	E_{NI} (mT)[a]	c_{An}[b]	c_{NI}[b]
0.2	72.59	-7.55	74.14	1.05	0.40	0.60
3.2	72.87	-7.55	72.76	0.81	0.76	0.24
25.6	72.56	-7.44	74.79	0.61	0.90	0.10

Compound 3

Delay (µs)	D_{An} (mT)[a]	E_{An} (mT)[a]	D_{NI} (mT)[a]	E_{NI} (mT)[a]	c_{An}[b]	c_{NI}[b]
0.2	72.58	-7.42	74.26	1.05	0.40	0.60
3.2	72.49	-7.27	75.33	0.95	0.47	0.53
25.6	72.34	-7.27	72.90	0.86	0.71	0.29

Compound 2

Delay (µs)	D_{An} (mT)[a]	E_{An} (mT)[a]	D_{NI} (mT)[a]	E_{NI} (mT)[a]	c_{An}[b]	c_{NI}[b]
0.2	71.92	-7.30	75.88	1.01	0.32	0.68
3.2	71.97	-7.31	77.00	1.36	0.51	0.49
25.6	71.14	-7.03	76.90	0.83	0.73	0.27

Compound 1

Delay (µs)	D_{An} (mT)[a]	E_{An} (mT)[a]	A'_x[c]	A'_y[c]	A'_z[c]	c_{An}[b]
0.8	38.78	-6.59	1.0	0	0	1.0

[a] D and E parameters obtained using Equation 1 to fit experimental results

[b] coefficient preceding ^{3*}An and ^{3*}NI contribution to the overall fit using the functional form: $c_{An} * (S-T_0) + c_{NI} * (S-T_0)$

[c] relative population rates for spin-orbit intersystem crossing (SO-ISC)
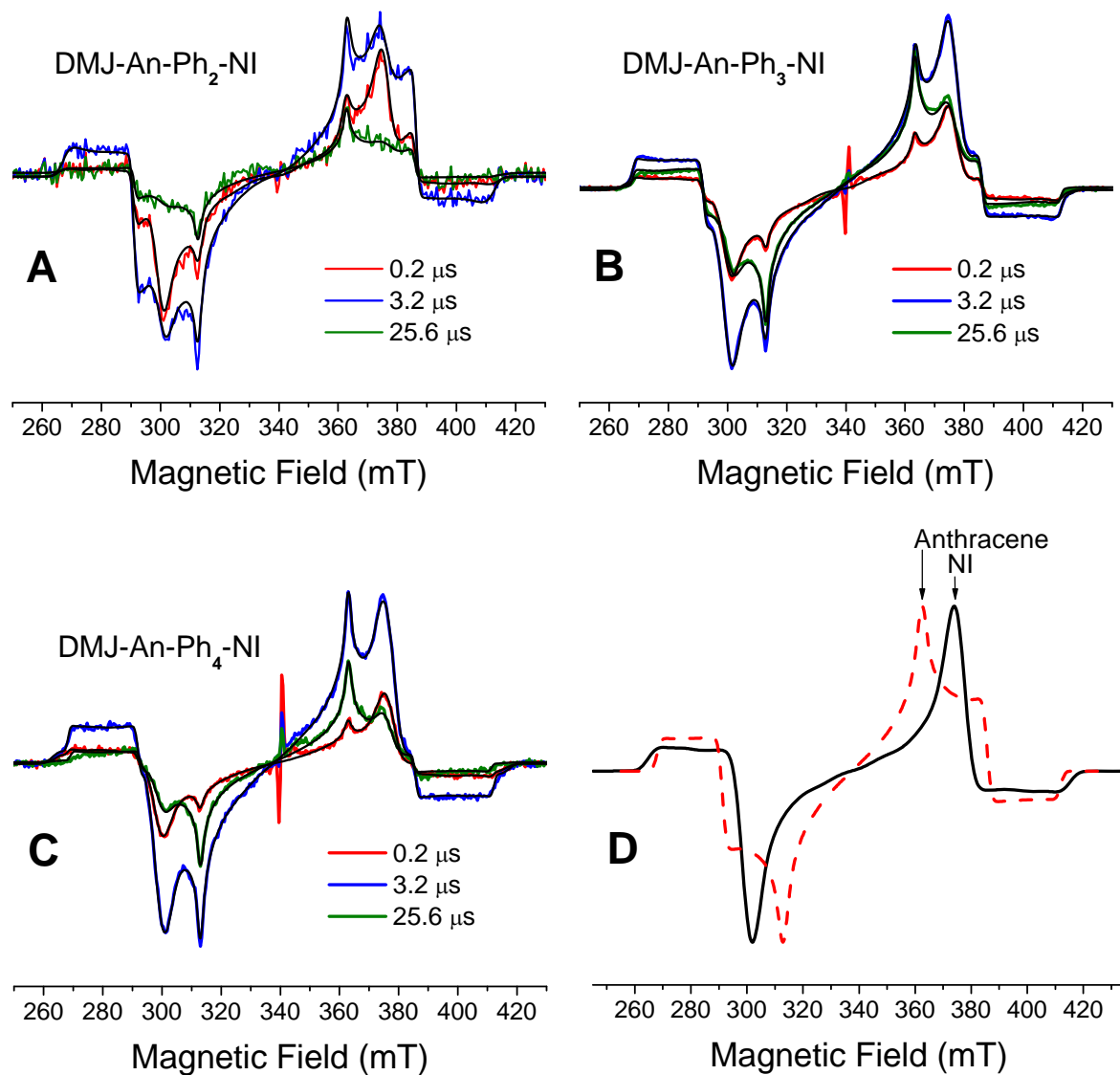
Figure 3.6. TREPR spectra of (A) **2**, (B) **3**, and(C) **4** in toluene at the indicated times at 85 K following a 416 nm, 1.5 mJ laser pulse. The sharp features at the center of the spectra in (B) and (C) are the radical pair signals, while the broad features are the triplet signals. Smooth curves superimposed on the experimental spectra are computer simulations of the triplets with the parameters given in **Table 3.3**. (D) computer simulated spectra of ^{3*}NI and ^{3*}An indicating their respective contributions to the total lineshape in A-C.
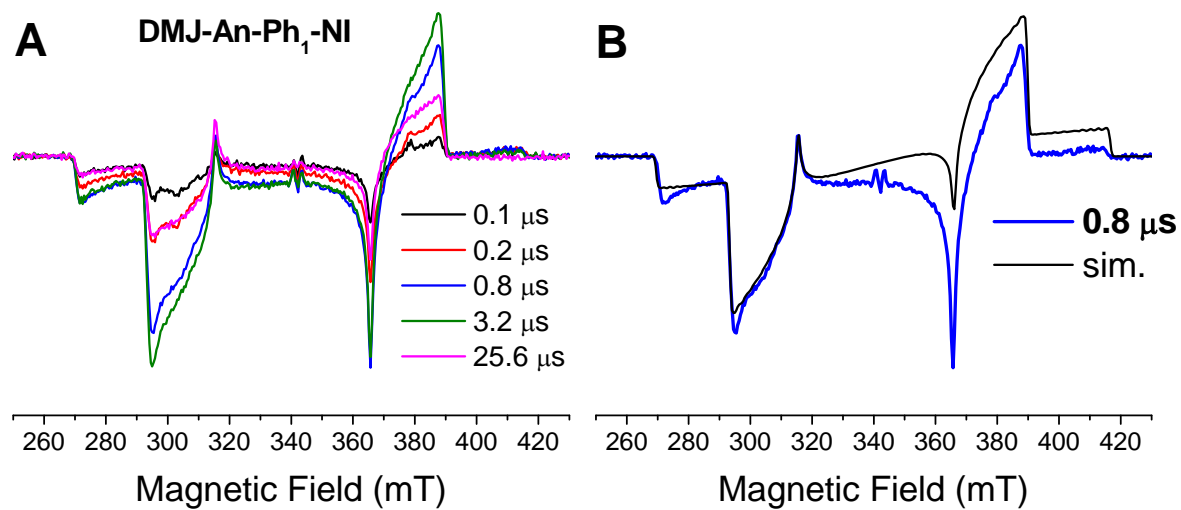
Figure 3.7. TREPR spectra of **1** at the indicated times at 85 K following a 416 nm, 1.5 mJ laser pulse at. A) selected times and B) at 0.8 μs with the computer simulation using the parameters given in **Table 3.3**.
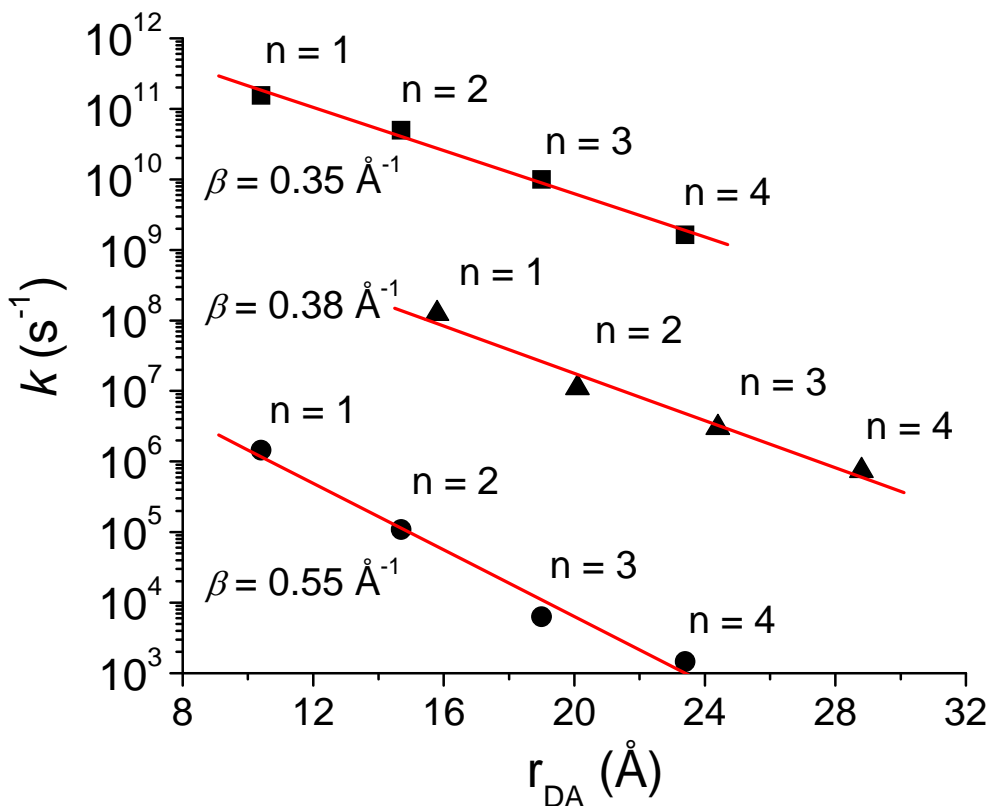
Figure 3.8. Plots of k_{CS} (■), k_{CR} (▲) at 293 K, and k_{TEnT} (●) at 85 K vs. distance, r_{DA}. The red lines are the linear fits to the data.

All of the broad triplet spectra in **2-4** were simulated using the S-T_0 RP-ISC mechanism, and the parameters from the line shape analysis are summarized in Table 3.3. Each simulation is a composite spectrum incorporating a linear combination of the ^{3*}NI and ^{3*}An line shapes whose respective contributions vary as a function of time. In contrast, the computer simulations indicate that triplet formation in **1** results from an SO-ISC mechanism. At early times ^{3*}NI is obviously present, Figure 3.7, but because TEnT is fast, the ^{3*}NI contribution to the total observed spectrum is very small. As such, it was not possible to determine spectral fitting parameters corresponding to ^{3*}NI. However, at later times, the fits of **1** indicate that an SO-ISC mechanism is dominant and that the D and E parameters correspond to ^{3*}An with the relative

population rates heavily favoring the T'_X spin state relative to the T'_Y or T'_Z states. Because the mechanism of triplet formation is different, an exponential fit to the rise of ^{3*}An was used in order to determine k_{TEnT} for **1**.

3.3 Discussion

3.3.1 Superexchange Charge Transfer and Radical Pair Spin Dynamics

The observed exponential distance dependence for both k_{CS} and k_{CR} at 293 K in **1-4** reveals that the superexchange electron transfer mechanism dominates, Figure 3.8.[18, 19] In the superexchange mechanism the bridge orbitals are energetically well-separated from those of the donor and acceptor and the electronic coupling matrix element, V_{DA}, gives the effective interaction energy between the relevant orbitals on the donor and acceptor.[32-34] Importantly, the rate of electron transfer is proportional to V_{DA}^2, which is a strong function of D-B-A structure.[35, 36] Furthermore, when the charge transport process originates from a state in which the redox centers are also paramagnetic, e.g. charge recombination from a radical ion pair (RP) state $D^{+\bullet}$-B-$A^{-\bullet}$, the superexchange coupling, V_{DA}, which dictates charge transfer is the same coupling that determines the magnetic interaction between the unpaired spins in the RP. Therefore $2J$, and its dependence on molecular structure mirror that of V_{DA}.[32-34, 37-42] We have demonstrated earlier that $2J$ is proportional to V_{DA}^2, and is highly sensitive to both the RP distance and the structure of the intervening bridge system.[30, 43-46, 117, 130] In addition, the spin dynamics monitored with TREPR that accompany RP-ISC provide a very sensitive measure of $2J$.

Following photoexcitation, charge separation yields ^{1}(DMJ$^{+\bullet}$-An-Ph$_n$-NI$^\bullet$), which subsequently undergoes S-T_0 RP-ISC to produce ^{3}(DMJ$^{+\bullet}$-An-Ph$_n$-NI$^\bullet$). Computer simulations

at 293 K agree remarkably well with the RP TREPR experimental spectra, Figure 3.4. The

parameters derived from these simulations show that *2J* behaves very similarly to other systems

studied in this laboratory.[29, 30, 45]   Specifically, *2J* in **2** and **3** decreases as the temperature

decreases and as the length of the intervening bridge structure increases. As the temperature

decreases, the amplitude of the torsional motions about the single bonds joining the phenyls of

the bridge is reduced resulting in conformations having larger dihedral angles between the π

systems of the phenyl units. The diminished electronic coupling within the bridge is the most

likely source of the decrease in *2J* as the temperature decreases. In **4** at room temperature, *2J* is

already quite small and does not change appreciably at 85 K. At lower temperatures, the fits of

the data are not as good as those at 293 K, particularly that of **2**. The hyperfine coupling

constants and *g*-factors used in the computer simulations were assumed to be temperature

independent. However, it is clear in **2-4**, Figure 3.4, that the *g*-factors and hyperfine coupling

constants are anisotropic at low temperature. The resulting line broadening makes it difficult to

determine very small values of *2J*. Thus, the small changes of *2J* with temperature in **4** and the

parameters determined for **2** at low temperature should be viewed with appropriate caution.

Temperature dependent CW-EPR studies of the DMJ$^{+\bullet}$ radical cation, which can be used to

determine more accurate fitting parameters as a function of temperature, are underway.

Probably due to its short RP lifetime, the RP spectrum for **1** is not detected at any

temperatures. Although **2** also has a relatively large *2J* value at 293 K, it exhibits a detectable

TREPR spectrum which is a direct result of the nearly quantitative yield of charge transfer. The

RP spectrum seen in **3** displays the most structure of any RP in these systems. The breadth of the

spectrum results from large hyperfine coupling constants in the DMJ$^{+\bullet}$ radical cation.   In

particular, hyperconjugation with the aromatic π system of the julolidine leads to significant spin

density and large hyperfine coupling constants for the β-protons attached to nitrogen and the sp^2 carbons, Figure 3.5.

It is particularly interesting to note that at 293 K $k_{TT}^{CR} < k_{SS}^{CR}$ whereas at low temperatures, this relationship is reversed, Table 3.1. This result is in contrast to other systems studied in our laboratory[13, 30], where k_{TT}^{CR} was the dominant recombination route at all temperatures. As discussed in the introduction, those systems employed Ph$_n$ bridges to connect a PTZ donor to a PDI acceptor. We have shown previously that the total reorganization energy, λ, for charge recombination of the RPs within PTZ-Ph$_n$-PDI at room temperature is about 0.6 eV.[117] Spin-selective formation of the ground state by charge recombination from the singlet RPs of PTZ-Ph$_{4,5}$-PDI, where ΔG_{SS}^{CR} = -2.1 to -2.2 eV, lies deep within the Marcus inverted region[94] of the rate vs. free energy profile, while the formation of the corresponding local triplet state from the triplet RPs, where ΔG_{TT}^{CR} = -0.9 to -1.0 eV, is much closer to the peak of the rate vs. free energy profile, Figure 3.9. Thus, energy gap considerations alone predict that k_{TT}^{CR} should be larger than k_{SS}^{CR}. It should be noted that Figure 3.9 illustrates the relationship of the free energy profiles between the RP, ground, and local triplet states in PTZ-Ph$_{4,5}$-PDI and **2-4**. Conventionally in these diagrams, the reactant state is positioned closer to the origin or the Reaction Coordinate axis, while the product state is shown further from the origin. However, in Figure 3.9, the reactant state, i.e., the RP, is depicted so that it can clearly be seen that charge recombination to the ground state is in the Marcus inverted region while charge recombination to the local triplet state is in the Marcus normal region.
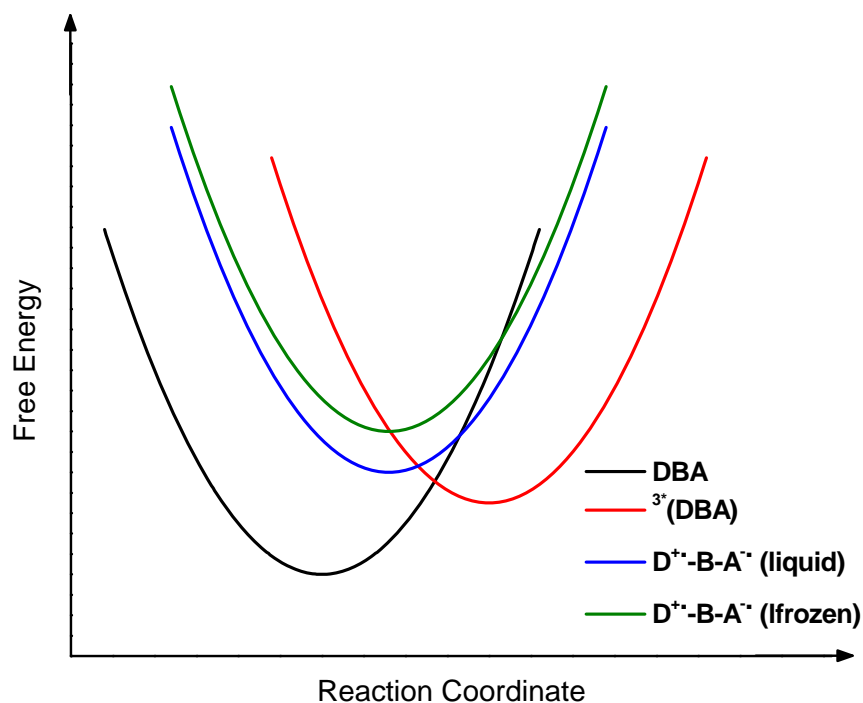
Figure 3.9. A schematic potential energy diagram illustrating the change in RP state energy and how it affects spin-selective recombination energetics.

Likewise, at 293 K in **2-4**, where ΔG_{SS}^{CR} = -2.2 to -2.3 eV and ΔG_{TT}^{CR} = -0.2 to -0.3 eV, the strongly constrained nature of DMJ-An leads to a similar value, $\lambda \approx$ 0.5 eV, for the total reorganization energy. However, at low temperature in a frozen toluene matrix, solvent reorganization is inhibited and the RP state energies increase because they are no longer stabilized by solvent dipole rotations.[131, 132] The effect of this destabilization is twofold; ΔG_{SS}^{CR} is moved further into the Marcus inverted region, and ΔG_{TT}^{CR} approaches the peak of the rate vs. free energy profile, Figure 3.9. Thus, the combined effect of these energetic terms will change the relative magnitudes of k_{SS}^{CR} and k_{TT}^{CR} as a function of temperature, and possibly even change the dominant recombination route. Nonetheless, although energetic considerations may be able

to account for a reversal in the relative magnitudes of k_{SS}^{CR} and k_{TT}^{CR} as a function of temperature, the values of ΔG_{SS}^{CR} and ΔG_{TT}^{CR} predict that k_{TT}^{CR} should be larger than k_{SS}^{CR} in **2-4** at all temperatures. The fact that the simulations show a switch in the dominant recombination route suggests that energetic factors alone are insufficient to explain this result and that electronic coupling and vibronic overlap contributions must also be considered.

3.3.2 Triplet State TREPR Spectra resulting from RP-ISC and Triplet-Triplet Energy Transfer

Following RP-ISC, spin-selective charge recombination in **2-4** transfers the non-Boltzmann spin populations of the RP states to the triplet state ^{3*}(D-B-A).[120] In this situation, population of ^{3*}(D-B-A) following charge recombination is selective with respect to the high-field eigenfunctions. The high-field T'_0 triplet sublevel is overpopulated at all canonical orientations, and the ESP patterns are preserved within a particular transition, i.e., $T'_0 \leftrightarrow T'_1$ or $T'_0 \leftrightarrow T'_{-1}$, Figure 3.3B, yielding the observed (*a,e,e,a,a,e*) ESP pattern, Figure 3.6A-C.[97-99] The EPR spectra explicitly show for the first time the *direction* of charge recombination, i.e. it occurs by hole transfer via the HOMOs from DMJ$^{+\bullet}$ to NI$^{\bullet}$ to initially yield ^{3*}NI preferentially over electron transfer via the LUMOs from NI$^{\bullet}$ to DMJ$^{+\bullet}$ to initially yield ^{3*}An.

As discussed above, charge transfer in these systems occurs via superexchange, whereby an electron or hole is transferred in a single step from donor to acceptor, and the bridge, whose states are too high in energy to be directly occupied, is used as a medium for electronic coupling. The redox state of the bridge does not change, and the probability of transferring an electron/hole between donor and acceptor generally decreases exponentially with distance. The electronic

coupling matrix element for the superexchange charge transfer mechanism V_{DA} can be approximated as $V_{DB} \cdot V_{BA}/\Delta E_{DB}$, where V_{DB} and V_{BA} are the donor-bridge and bridge-acceptor couplings, respectively, and ΔE_{DB} is the donor-bridge energy gap.[19, 133-135] These parameters are determined primarily by bridge structure and length, conformational rigidity, temperature, and the electronic properties of the redox centers.[27, 28, 30, 43-46, 117, 130] The energies of all the electronic states with charge formally residing on the bridge in **1-4** are high enough that these states remain unpopulated virtual states. However, the energy gaps between $DMJ^{+\bullet}$-An-Ph_n-$NI^{\bullet}$ and DMJ-An-$Ph_n^{+\bullet}$-$NI^{\bullet}$ are ~1.0-1.4 eV smaller than those between $DMJ^{+\bullet}$-An-Ph_n-$NI^{\bullet}$ and $DMJ^{+\bullet}$-An-$Ph_n^{-\bullet}$-NI, Table 3.1. As a result, superexchange-mediated hole transfer via the HOMOs is energetically favored over electron transfer via the LUMOs for this D-B-A series.

Following the formation of ^{3*}NI, triplet-triplet energy transfer (TEnT) from ^{3*}NI to ^{3*}An occurs, TEnT occurs by a Dexter-type mechanism that can viewed as a pair of simultaneous hole and electron transfer events involving the HOMOs and LUMOs, respectively, of the D-B-A system.[136] Thus, it is governed by the same parameters used to describe superexchange electron or hole transfer.[40, 137] Specifically, the rate constant for TEnT, k_{TEnT}, also displays an exponential distance dependence $k_{TEnT} = k_0 \exp[-\beta \cdot (r_{DA}-r_0)]$, where k_0 is the rate constant at van der Waals contact, r_0, r_{DA} is the donor-acceptor center-to-center distance, and β depends on the nature of the bridge and the energy matching between the donor and the bridge.[138] Figure 3.8 shows a plot of ln k_{TEnT} vs. r_{DA} for **1-4** in which the best fit line through the data points gives $\beta_{TEnT} = 0.55$ Å^{-1}. This value of β_{TEnT} is similar to that obtained from studies of TEnT from $Ru(bpy)_3^{2+}$ to $Os(bpy)_3^{2+}$ through olig*o-p*-phenylenes, where $\beta = 0.50$ Å^{-1}.[139]

The plots of k_{CS} and k_{CR} vs. r_{DA} for **1-4** in Figure 1 yield $\beta_{CS} = 0.35$ Å^{-1} and $\beta_{CR} = 0.38$ Å^{-1}, respectively. It has been shown that $\beta_{TEnT} \cong \beta_{CS} + \beta_{CR}$ provided that the Franck-Condon-weighted densities of states (FCWD) are similar for these processes. [40, 96, 137] Using this approximation, the measured values of β_{CS} and β_{CR} predict that $\beta_{TEnT} = 0.73$ Å^{-1} which is only modestly larger than the measured value of $\beta_{TEnT} = 0.55$ Å^{-1}. There are several possible factors which are responsible for the difference between the measured and predicted values, however the most probable is that k_{CS} and k_{CR} are measured at 293 K, while k_{TEnT} is obtained at 85 K. As shown in the previous section, variations in temperature can strongly affect the electronic coupling matrix elements of charge transfer processes. In these systems and related oligo-*p*-phenylenes, there is a corresponding reduction in the electronic coupling as the temperature is decreased.[13, 30] The electron/hole transfer and TEnT processes are all very sensitive to the electronic coupling, so it is remarkable that the measured and predicted values are in such agreement. An additional factor is that the β values obtained for this series assume a constant Franck-Condon weighted densities of states (FCWD) contribution to the rates of charge and energy transfer. Although the distance dependence of the electronic coupling is far stronger, the solvent reorganization energy, λ_S, which is included in FCWD term, varies weakly with distance and will contribute to the deviation. Finally, all of these processes occur from different initial states and finish at different final states. Despite the participation of the oligo-*p*-phenylene bridge in each step, the energy matching between the initial and final states and the bridge states is different for each event. It has been demonstrated that ΔE_{DB} can make strong contribution to the measured rate constants of charge transfer processes.[135, 140-142]

Finally, although it is clear from the experimental spectra that ^{3*}NI is formed first, the spectral computer simulations indicate that the ^{3*}An contribution to the total line shape is larger

than what is expected based on TEnT alone. This reveals that some charge recombination via the LUMOs happens even though the virtual states associated with electron transfer are substantially higher than those for hole transfer, Table 3.1. The likely reason for this is that the RPs live long enough even to allow a process having a substantial tunneling barrier to proceed with a moderate yield. The contribution from ^{3}(DMJ$^{+\bullet}$-An-Ph$_n$-NI$^\bullet$) directly to DMJ-^{3*}An-Ph$_n$-NI is expected to increase as the bridge lengthens corresponding to a decrease in the energy of the virtual states involved with electron transfer[29, 123], Figure 3.2A. However, we were unable to measure this process directly, and further work is underway to quantify the respective contributions to ^{3*}An.

3.3.3 Conservation of Spin Polarization and Triplet State TREPR spectra resulting from SO-ISC

The exchange operator which dictates TEnT does not change the electron spin direction. As a result, the non-Boltzmann spin populations in **2-4** are preserved during TEnT, i.e., electron spin polarization is conserved.[136, 143-146] Akiyama et al.[147, 148] used TREPR to study intramolecular TEnT within two naphthalene spirans where the donor and acceptor orientations were rigidly fixed by the spiran connectivity. In these systems a spin-orbit mechanism was responsible for the donor polarization pattern. During TEnT, the donor magnetic sublevel populations were transferred with probabilities that are proportional to the squares of the projections onto the principal magnetic axes of the acceptor. Importantly, the EPR spectra that resulted from TEnT could exhibit extreme deviations from symmetry depending on the relative orientation of the donor and acceptor as well as the zero-field splitting parameters for both the donor and acceptor. As previously discussed, the triplet ESP phase patterns in **2-4**, result from

RP-ISC. Since RP-ISC operates directly the high-field triplet sublevels, when TEnT occurs, this polarization is preserved. As such, both ^{3*}NI and ^{3*}An exhibit the characteristic ESP phase pattern resulting from RP-ISC.

In contrast, the mechanism of triplet formation in **1** is entirely different than that in **2-4**. If the orientation between the relevant orbitals of D and A is such that charge transfer between them is coupled with a significant change in orbital angular momentum, recombination of ^{1}(D$^{+\bullet}$-B-A$^{\bullet}$) may be accompanied by a spin flip to directly yield ^{3*}(D-B-A).[63, 65, 66] Okada et al.[63] originally proposed this mechanism to explain the formation of a pyrene triplet state within 30 ps following photoexcitation of pyrene to its lowest excited singlet state in a covalently-linked pyrene-*N*-methylaniline derivative. RP-ISC, which usually occurs on a timescale of a few nanoseconds, could not explain the rapid rate of formation of the pyrene triplet state. They found that the ISC rate was strongly dependent upon the mutual orientation of the donor and acceptor groups and concluded that $\langle ^{1}(D^{+\bullet}\text{-B-A}^{\bullet}) | \mathcal{H}_{SO} | ^{3*}(D\text{-B-A}) \rangle$ increases when the electron donating and accepting molecular orbitals are approximately perpendicular to each other. This mechanism has been observed for several other electron donor-acceptor systems,[64-66] and has been found to depend strongly on the magnitude of the electronic coupling between D$^{+\bullet}$ and A$^{\bullet}$ as well.[64, 66, 67, 105, 106, 144]

In aromatic molecules of sufficient symmetry, such as NI and An, the triplet axis system usually coincides with the lowest electronic transitions and is clearly dictated by the molecular structure.[107, 108, 144] We have not experimentally assigned the principal triplet molecular axes of ^{3*}NI, however it is reasonable to assume that the z-axis is the out-of-plane axis, as is typical of π-π^{*} triplets of aromatic molecules, which leaves the x and y axes in the plane of ^{3*}NI.[109-111] For

the sake of clarity, we will assume that the long axis of NI is the y-axis. Density functional

theory (DFT) calculations[126] using the B3LYP[149, 150] functional and 6-31G* basis set show that

the torsional angle between the DMJ and An π systems is 90° while that between NI and An is

~14°. Thus, electron transfer from DMJ$^{+\bullet}$ to NI$^{-\bullet}$ involves moving an electron between two

orbitals having a torsional angle of 76° between them. Using the right hand rule, this implies

that the angular momentum change is along the y direction, so that the spin orbit interaction that

drives ^{1}(DMJ$^{+\bullet}$-An-Ph$_n$-NI$^{-\bullet}$) → DMJ-An-Ph$_n$-^{3*}NI should selectively populate T$'_Y$ of DMJ-An-

Ph$_n$-^{3*}NI. At early times, ^{3*}NI is visible in the TREPR spectra of **1**, Figure 3.7A. Unfortunately,

the line shape can not be simulated because it is heavily obscured by the presence of ^{3*}An which

grows in with the time constant of TEnT, τ_{TEnT}.

Studies have shown the energetic order of anthracene's triplet sublevels to be T$'_X$ > T$'_Y$ >

T$'_Z$, such that the ZFS parameters $D > 0$ and $E < 0$. The principal axis system is defined with z

being perpendicular to the molecular plane with x and y in the plane where in this case x is

parallel to the long axis.[107, 108, 144, 151] The (e,e,a,e,a,a) phase pattern displayed by **1** is best

simulated by preferential population of the T$'_X$ sublevel, Figure 3.7B. We have shown that some

charge recombination occurs via the energetically unfavored LUMOs in **2-4**. If the source of

^{3*}An in **1** was from direct recombination, i.e., ^{1}(DMJ$^{+\bullet}$-An-Ph$_n$-NI$^{-\bullet}$) → DMJ-^{3*}An-Ph$_n$-NI, then

invoking the same SO-ISC mechanism as described in the formation of ^{3*}NI would lead to

preferential population of T$'_Y$ which is not the case. In fact, computer simulations of the triplet

spectra of the model compound **DMJ-^{3*}An** indicate that its (e,a,e,a,e,a) ESP phase pattern

following photoexcitation is the result of an SO-ISC coupling mechanism with preferential

population of the T$'_Y$ sublevel as predicted.[99, 112] This evidence suggests that direct

recombination does not make a significant contribution to the formation of ^{3*}An seen in **1**. Furthermore, the asymmetry seen in the triplet spectrum of **1** is additional evidence that ^{3*}NI followed by TEnT leads to population of ^{3*}An. As discussed earlier, TEnT can cause significant deviations from spectral symmetry and further modeling is underway to improve the computer simulations.

3.4 Conclusions

TREPR studies have been used to elucidate the RP and triplet spin dynamics of DMJ-An-Ph$_n$-NI. The photoexcited charge transfer state of DMJ-An acts as a high-potential photoreductant to rapidly and nearly quantitatively transfer an electron across the Ph$_n$ bridge to produce a spin-coherent singlet RP ^{1}(DMJ$^{+\bullet}$-An-Ph$_n$-NI$^{\bullet}$). Subsequent radical pair intersystem crossing in **2-4** yields ^{3}(DMJ$^{+\bullet}$-An-Ph$_n$-NI$^{\bullet}$) and spin-selective charge recombination yields the neutral triplet state. The recombinant triplet in **1** is formed by a SO-ISC mechanism where ^{1}(DMJ$^{+\bullet}$-An-Ph$_n$-NI$^{\bullet}$) $\rightarrow$ DMJ-An-Ph$_n$-^{3*}NI. This mechanism depends on the relative orientation of the orbitals involved in the charge recombination as well as the magnitude of the electronic coupling between the donor and acceptor. Time-resolved EPR spectroscopy shows directly that charge recombination of the RP initially produces a spin-polarized triplet state that can *only* be produced by hole transfer involving the HOMOs of D, B, and A within DMJ-An-Ph$_n$-NI. These results suggest that designing molecular systems for solar energy conversion requires judicious choice of synthetic components which match the electronic couplings and energy levels involved with the charge transfer processes.

Chapter 4

Intersystem Crossing Mediated by Photoinduced Intramolecular Charge

Transfer in Julolidine-Anthracene Donor-Acceptor Molecules

4.1 Introduction

In the past four decades, the photophysics of Donor-Acceptor (D-A) compounds formally linked by a single bond have been the focus of extensive study and lively discussion. The majority of the work thus far has been directed at understanding the electronic structures and conformations of these molecules in their ground and lowest excited singlet charge transfer states (^{1}CT).[118, 152-163] These systems usually display CT absorption and emission bands and exhibit large dipole moments which imply that significant electron density is transferred from the donor to the acceptor. One particular class of compounds that fulfills these criteria are 4-(9-anthryl)-*N,N*-dimethylaniline (ADMA) derivatives. ADMA was reported and thoroughly studied by Okada et al.[156] then later by others.[118, 152-155, 157-165] The nature of the ADMA excited CT state has been the source of much debate and has been specifically addressed by Okada *et al.*[166] and Herbich *et al.*[118, 167] and is summarized by Grabowski *et al.*[168, 169] Because ADMA derivatives show complex solvent polarity and temperature dependent behavior, many of these derivatives employ substituent steric effects to control intramolecular conformations. For example, in **J-An**, Figure 4.1, the julolidine moiety conformationally restricts the amine, which enforces conjugation between the nitrogen lone pair and the phenyl ring.[152] Of critical importance in systems such as **J-An** is the torsional angle (θ_1) between the π system of the anthracene and the nitrogen lone pair of the amine, which determines the degree of excited-state charge transfer character.[160, 161, 170-172]

Figure 4.1. Principal axis system and molecular structures of anthracene and its julolidine-substituted derivatives.

Despite the substantial attention these systems have received, there have been relatively few studies on the mechanism of radiationless CT state decay.[152, 173] As is usually the case, this decay can occur by internal conversion (IC) to the ground state or intersystem crossing (ISC) to the triplet manifold, Figure 4.2. In the present work, we explore the spin dynamics associated with the formation of the triplet state localized on the anthracene following photoexcitation into the CT absorption band of **J-An**, **DMJ-An**, and **DMJ-An–tol**, Figure 4.1. **DMJ-An** is modeled after **J-An**, but tailored in such a way as to further limit conformational motion in the ground and excited states. Methyl groups at both the 3- and 5- positions enforce a geometry wherein the π system of the julolidine is perpendicular to that of the anthracene, $\theta_1 \approx 90°$. **DMJ-An-tol** was

also studied because 9- and 9,10-substitution has been shown to have a dramatic effect on ISC in anthracene derivatives.[174-183]

A detailed analysis of the ISC mechanism in **J-An**, **DMJ-An**, and **DMJ-An–tol** requires careful consideration of the nature of their CT states, which can be represented as a mixture of ground, locally excited (LE), and CT states.[66, 162, 169, 184-188]

$$\Psi_{CT} = c_G \Psi^0_{D\text{-}A} + c_{*D} \Psi^0_{*D\text{-}A} + c_{1*A} \Psi^0_{D\text{-}1*A} + c_{3*A} \Psi^0_{D\text{-}3*A} + c_{CT} \Psi^0_{D+\bullet\text{-}A\text{-}\bullet\text{-}} \tag{1}$$

where $\Sigma c_i^2 = 1$. In these D-A systems, the contributions from the ground state and the locally excited donor (*D) state are small ($c_G \approx c_{*D} \approx 0$), while those of the singlet (c_{1*A}) and triplet (c_{3*A}) locally excited states should be significant because ISC is the relevant process.

Time-resolved electron paramagnetic resonance (TREPR) techniques, which are particularly well suited for investigating the behavior of charge and spin transfer mechanisms involving paramagnetic states,[9-11, 13-15, 68, 76, 77, 189-192] were used to examine the triplet states of **An**, **J-An**, **DMJ-An**, and **DMJ-An–tol**. The triplet EPR spectra exhibit electron spin polarization (ESP) patterns which are characteristic of the mechanism of their formation. These spectra depend strongly on the value of θ_1, which determines the degree of charge transfer (c_{CT}), the relative orientation of the molecular orbitals involved in the CT event, the magnitude of the electronic coupling between D and A, and the contribution from the locally excited states (c_{*A}).
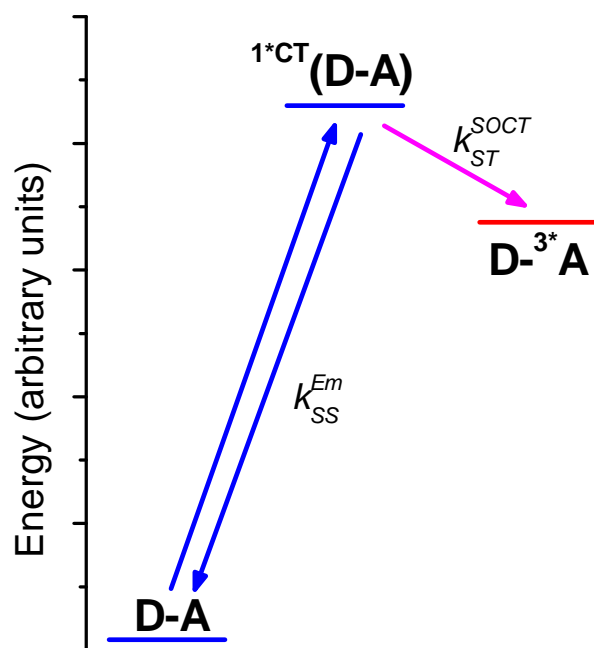
Figure 4.2. Energy levels and emission and intersystem crossing pathways for **J-An**, **DMJ-An**, and **DMJ-An-tol**.

4.1.1 Mechanisms of Intersystem Crossing and TREPR of Triplet States.

When CT states are formed following photoexcitation, Figure 4.2, there are two ISC mechanisms that may occur which yield a local triplet state. The first, radical pair-intersystem crossing (RP-ISC), involves electron-nuclear hyperfine coupling-induced mixing between the singlet (^{1}CT) and triplet (^{3}CT) states. This is followed by spin-selective recombination to produce the local triplet state (D-^{3*}A). The mechanistic details of RP-ISC and the theory behind magnetic field effects on electron transfer reactions have been researched extensively[13, 48-51] and have been applied to many donor-acceptor systems[29, 43, 44, 52-57] Alternatively, intersystem crossing from the singlet CT state may take place via a spin-orbit coupling mechanism to produce the local triplet state directly (^{1}CT → D-^{3*}A), provided that the symmetries of the

orbitals involved in the charge transfer are such that the spin flip is coupled with a significant change in orbital angular momentum.[63-67]

Application of a magnetic field results in Zeeman splitting of the triplet sublevels, which at low fields are best described by the zero-field eigenstates, T_X, T_Y, and T_Z, that are quantized in the molecular framework, and at high fields by the T_{+1}, T_0, and T_{-1} eigenstates that are quantized along the applied magnetic field, Figure 4.3. The main features of the EPR spectrum of D-^{3*}A arise from zero-field splitting (ZFS), which is a result of the magnetic dipole-dipole interaction between the two unpaired electrons in the triplet state. The Hamiltonian that describes this interaction is:[79-82]

$$\mathcal{H}_{\text{dipolar}} = D(\mathbf{S}_z^2 - \mathbf{S}^2/3) + E(\mathbf{S}_x^2 - \mathbf{S}_y^2) \tag{2}$$

where D and E are the zero-field-splitting parameters and $\mathbf{S_{x,y,z}}$ are the components of the total spin angular momentum operator ($\mathbf{S}$) for the triplet state. The effect of this term is to lift the degeneracy of the triplet manifold in the absence of an external magnetic field as a function of the symmetry of the molecule. The polarization of the EPR transitions exhibited by D-^{3*}A formed by a spin-orbit-intersystem crossing mechanism (SO-ISC) can be differentiated from the RP-ISC mechanism by the ESP pattern of the six EPR transitions, i.e. the two transitions at each canonical (x, y, z) orientation.[78] In SO-ISC, the three zero-field levels T_X, T_Y, and T_Z of D-^{3*}A are selectively populated and this selectivity is carried over to the high field energy levels. For example, assuming selective population of the T_Y zero-field level and $D > 0$, Figure 4.3A shows that the six EPR transitions from low to high field yield an (e,a,e,a,e,a) polarization pattern, where a = enhanced absorption and e = emission of microwave radiation. In contrast, RP-ISC acts directly on the high-field triplet sublevels of the RP via S-T_0 mixing, Figure 4.3B. Spin

polarization is preserved upon recombination, and the resulting (a,e,e,a,a,e) polarization pattern exhibited by D-^{3*}A is the unique signature of the RP-ISC mechanism.
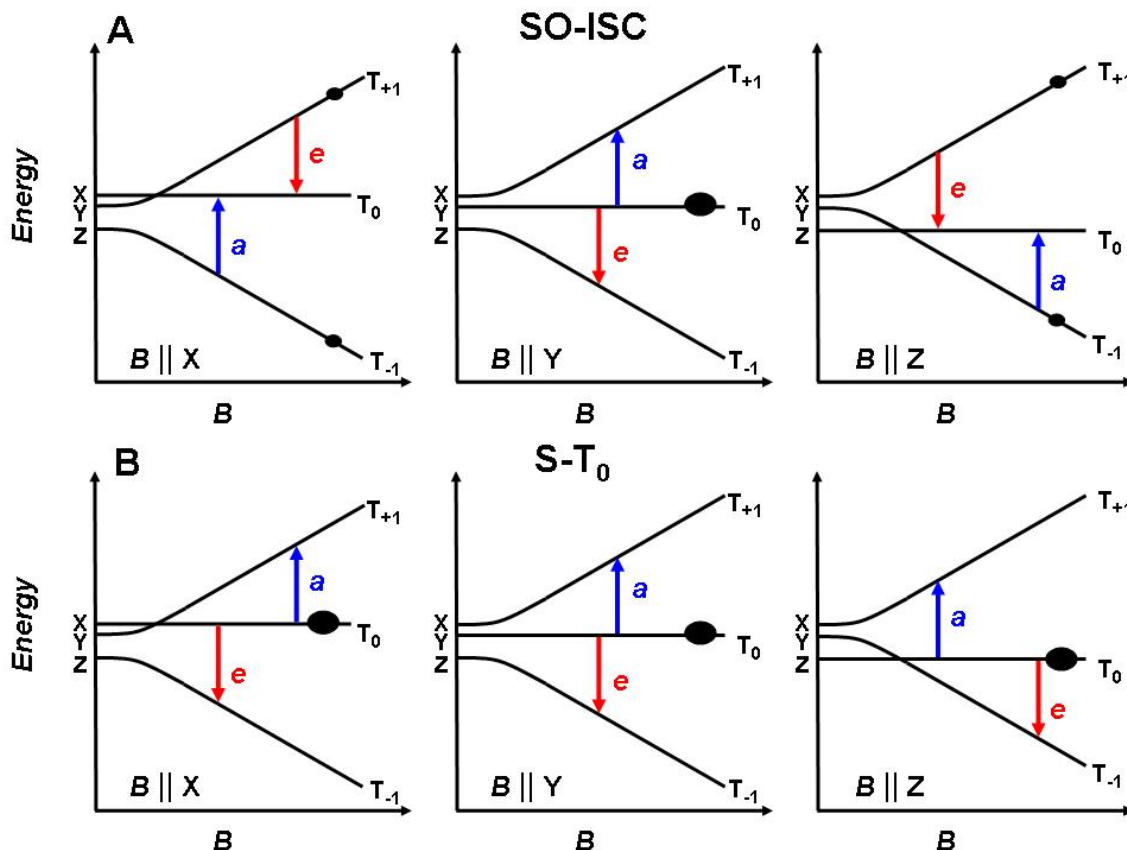
Figure 4.3. Energy levels of D-^{3*}A formed by (A) SO-ISC with selective population of T_Y ($D > 0$, $E < 0$) and (B) S-T_0 mixing within a radical pair precursor. The arrows indicate the direction of the transition and are labeled $a =$ enhanced absorption, $e =$ emission.

4.2 Results and Discussion

The ground-state spectrum of **DMJ-An** can be deconvoluted into a sum of Gaussians to account for the anthracene Franck-Condon progression and an additional Gaussian to fit the broad **DMJ-An** charge-transfer absorption band. The presence of the CT absorption band indicates that there is moderately strong electronic coupling between the julolidine and anthracene moieties in **J-An**, **DMJ-An**, and **DMJ-An–tol**. The lowest excited singlet state

energy of **DMJ-An** in toluene at room temperature, obtained by averaging the energies of its

CT absorption and emission maxima at 367 and 519 nm, respectively, is 2.89 eV. Similarly, the

lowest excited singlet state energies of **J-An and DMJ-An-tol** in toluene are 2.95 eV and 2.87

eV, respectively. Following direct photoexcitation into the ^{1}CT absorption band, the $\Delta m_s = 1$

TREPR spectra of **J-An**, **DMJ-An**, and **DMJ-An–tol** in toluene at 85 K exhibit a broad triplet

spectrum with a width of ~150 mT, having an ESP phase pattern which results from a SO-ISC

type mechanism, Figure 4.4.   No triplet spectrum is observed for **J-An** following

photoexcitation.   Density functional theory (DFT) calculations[126] using the B3LYP[149, 150]

functional and 6-31G* basis set have been used to determine values of θ_1 for **J-An**, **DMJ-An**,

and **DMJ-An–tol** and θ_2 (between the π system of the anthracene and the π system of a 9-

substituted phenyl group) in **DMJ-An-tol** and 9-phenylanthracene (9-PhAn), Table 4.1.
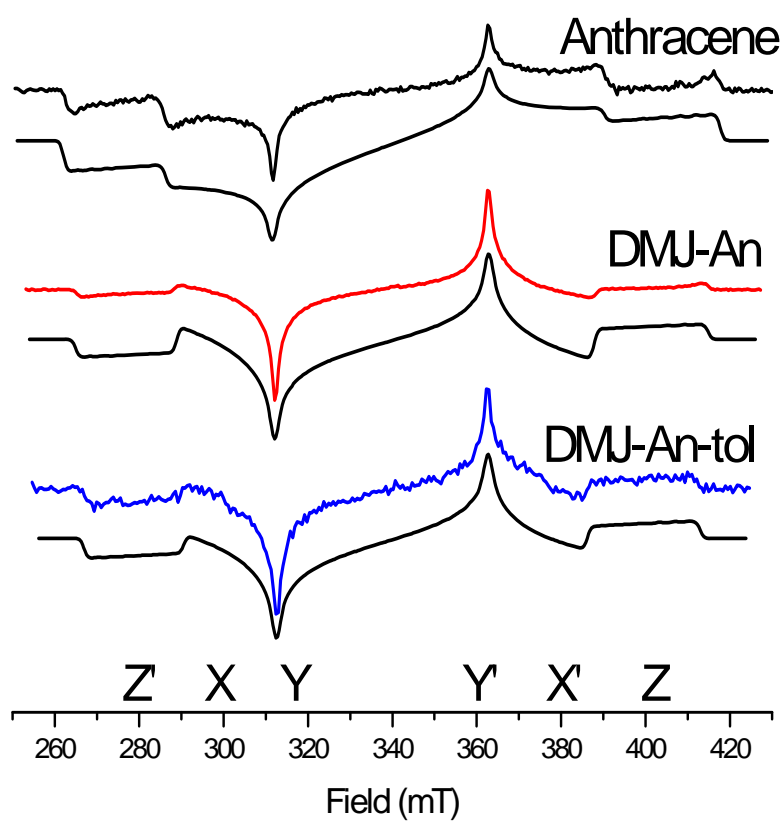
Figure 4.4. TREPR spectra of the indicated molecules in toluene at 85 K at 900 ns following a 416 nm, 1.5 mJ laser pulse. The canonical orientations of each transition are indicated. Smooth curves below the experimental spectra are computer simulations of spectra of the triplet spectra with parameters given in **Table 4.2**. Positive features are in enhanced absorption (*a*) and negative features are in emission (*e*).

Table 4.1. Calculated[a] torsional angles θ_1[b] and θ_2[c] in the ground state singlet and first excited triplet state.

molecule	Singlet θ_1	Singlet θ_2	Triplet θ_1	Triplet θ_2	%CT
J-An	75.1		56.9		60
DMJ-An	89.6		89.6		96
DMJ-An-tol	90.0	81.5	89.2	65.8	96
9-PhAn		86.9		67.5	

[a]Calculated using DFT, B3LYP functional, 6-31G* basis set
[b]θ_1 is the angle between julolidine and anthracene
[c]θ_2 is the angle between anthracene and the phenyl group (when present)

4.2.1 Triplet State TREPR Spectrum of Anthracene.

The ESP phase pattern for the ^{3*}An spectrum is (e,e,e,a,a,a), Figure 4.4. The complex photophysical behavior of anthracene and its derivatives following photoexcitation has been an active area of study for several decades.[11, 151, 181, 193-198] Experimental and theoretical[151] studies have shown the energetic order of anthracene's triplet sublevels to be $T_X > T_Y > T_Z$, such that the ZFS parameters $D > 0$ and $E < 0$, where the principal axis system is shown in Figure 4.1. These results have revealed that although unsubstituted anthracene is a planar aromatic system, it undergoes extremely efficient SO-ISC from ^{1*}An $\rightarrow$ ^{3*}An as a result of the energetic proximity of the S_1 and T_2 states (S_1-$T_2 \approx 500$ cm^{-1}).[174, 177, 182, 183] This SO-ISC process ($S_1 \rightarrow T_2 \rightarrow T_1$) is active in fluid solution at 295K as well as in a frozen solvent matrix at 77K. Symmetry arguments suggest that T_X should be preferentially populated, Figure 4.1; however, experimental evidence has shown that T_Y is also populated to a similar extent giving the (e,e,e,a,a,a) ESP phase pattern, Table 4.2.[11, 151, 192, 198] Computer simulations of the triplet spectra for ^{3*}An confirm that the (e,e,e,a,a,a) ESP phase pattern is the result of the SO-ISC coupling mechanism with preferential population of the T_Y and T_X sublevels, Figure 4.3A, for $D > 0$, $E < 0$.[99, 112]

Table 4.2. Zero-field splitting parameters (*D* and *E*) and relative population rates of the zero-field spin states obtained from simulations of the triplet-state TREPR spectra of the indicated molecules in a toluene matrix at 85 K.

molecule	*D* (mT)	*E* (mT)	A_X	A_Y	A_Z
Anthracene	77.81	-8.81	0.78	1.00	0.07
DMJ-An	74.96	-8.01	0.26	1.00	0.21
DMJ-An-tol	73.00	-7.56	0.45	1.00	0.32

4.2.2 Triplet State TREPR Spectra of DMJ-An and DMJ-An-tol.

In contrast to anthracene, the triplet spectra of **DMJ-^{3*}An** and **DMJ-^{3*}An-tol** both exhibit an (*e,a,e,a,e,a*) ESP phase pattern. The corresponding |*D*| and |*E*| values are only slightly smaller than those of unsubstituted anthracene, indicating that the triplet excitation is localized on the anthracene. The ZFS parameters and the relative population rates of the triplet sublevels were determined by computer simulation of the triplet line shape and are presented in Table 4.2. It has been suggested for similar D-A systems that ISC which results in population of D-^{3*}A occurs via the CT triplet state (^{3}CT).[152, 160] In this mechanism, the degree of charge separation must be sufficient so that the CT state is well described as a radical pair (D$^{+\bullet}$-A$^{\bullet}$ or $c_{CT} \rightarrow 1$). After photoexcitation and charge separation, the initially formed ^{1}CT will undergo electron-nuclear hyperfine coupling-induced RP-ISC to the nearly degenerate ^{3}CT state. This is followed by spin-selective recombination where ^{1}CT $\rightarrow$ D-A and ^{3}CT $\rightarrow$ D-^{3*}A. In such cases, population of D-^{3*}A following charge recombination is selective with respect to the high-field eigenfunctions and not the molecular zero-field eigenfunctions, as is the case for SO-ISC. Specifically, if the high-field T_0 triplet sublevel is overpopulated at all canonical orientations within **DMJ-^{3*}An** and **DMJ-^{3*}An-tol**, their triplet EPR spectra should exhibit the (*a,e,e,a,a,e*) polarization pattern, which is not the case, Figure 4.3B.[97-99] In order for RP-ISC to occur efficiently, the magnitude

of the singlet-triplet splitting between the ^{1}CT and ^{3}CT states, *2J*, must be comparable to or smaller than the hyperfine interactions between the two radicals. This is almost certainly not the case in **J-An**, **DMJ-An** and **DMJ-An-tol** because the presence of the optical CT absorption and emission bands indicates strong electronic coupling. Thus, we can definitively rule out RP-ISC as the mechanism of ISC in these systems.

We similarly conclude that any contribution from the *direct* SO-ISC contribution operative in ^{1*}An → ^{3*}An is also negligible because the ESP phase patterns do not match. However, an alternative spin-orbit mechanism which couples the CT state and the triplet LE state has been suggested by several groups studying molecular CT complexes.[173, 199-203] Iwata et al.[199] analyzed complexes between a 1,2,4,5-tetracyanobenzene acceptor and mesitylene, durene, and hexamethylbenzene donors at 77 K and found that the CT lifetime decreased as the donor ability increased. They concluded that CT complex formation created additional singlet-triplet mixing processes which resulted in faster decay of the CT complex. Similarly, Gould et al.[66] determined that rapid SO-ISC from the singlet exciplex results in direct population of the excited cyanoanthracene triplet in a series of exciplexes between cyanoanthracene acceptors and alkylbenzene donors. In these intermolecular CT complexes, the orientation and distances between D and A are not well defined, so that a detailed mechanistic understanding is difficult to determine.

In comparison, intramolecular D-A molecules provide relatively well-defined conformations and fixed distances. In these systems, if the orientation between the relevant orbitals of D and A is such that charge transfer between them is coupled with a significant change in orbital angular momentum, recombination of ^{1}(D$^{+•}$-A$^{•}$) may be accompanied by a spin flip to directly yield D-^{3*}A.[63, 65, 66] Okada et al.[63] discovered that the ISC rate was strongly

dependent upon the relative orientation of the donor and acceptor groups in a covalently-linked pyrene-*N*-methylaniline derivative. RP-ISC, which usually occurs on a timescale of a few nanoseconds, could not explain formation of a pyrene triplet state within 30 ps following photoexcitation of pyrene to its lowest excited singlet state. They concluded that when the electron donating and accepting molecular orbitals are approximately perpendicular to each other, the rate of $D^{+\bullet}-A^{-\bullet} \rightarrow D^{-3*}A$ is increased. In this case the spin-orbit interaction does not result in $^{1}(D^{+\bullet}-A^{-\bullet}) \rightarrow {}^{3}(D^{+\bullet}-A^{-\bullet})$ because $\langle {}^{1}(D^{+\bullet}-A^{-\bullet}) | \mathcal{H}_{SO} | {}^{3}(D^{+\bullet}-A^{-\bullet}) \rangle = 0$, due to the fact that there is no change in the spatial orbital for this process.[103] This mechanism is formally similar to rapid SO-ISC that occurs in an n-π^{*} electronic transition within a single chromophore. However, because it requires the ^{1}CT precursor, we will refer to it as spin-orbit, charge transfer intersystem crossing (SOCT-ISC) for the remainder of this paper. The matrix element which describes this interaction is $\langle {}^{1}(D^{+\bullet}-A^{-\bullet}) | \mathcal{H}_{SOCT} | D^{-3*}A \rangle$.

Using TREPR, van Willigen et al.[65] studied 10-methylacridinium systems having arene electron donors attached to their 9-position. Although the ZFS parameters remained essentially constant, the relative population rates, A_X, A_Y, and A_Z, and thus the ESP phase pattern, were found to be a sensitive function of the orientation of the donor and acceptor ring systems. They found that the SOCT-ISC rate was enhanced with an approximately perpendicular orientation between the donor and acceptor, $\theta_1 \approx 90°$. In another example, Wasielewski et al.[64] compared triplet formation between a zinc porphyrin both isolated and serving as an electron donor to which a tetracyano-naphthoquinodimethane acceptor was rigidly attached so that the π systems of the donor and acceptor were oriented approximately 60° relative to one another. Following photoexcitation at 10 K, TREPR of the isolated zinc porphyrin revealed a porphyrin triplet state

where SO-ISC exclusively populates the out-of-plane sublevel, T_Z, whereas in the D-A system, the porphyrin triplet state displayed an ESP pattern indicative of SOCT-ISC to the in-plane sublevels, T_X and T_Y. More recently, Dance et al.[13] showed that in addition to the dependence on orientation between the orbitals relevant to charge transfer, the magnitude of the electronic coupling between D and A strongly influences the contribution from the SOCT-ISC process. While studying a series of D-B-A molecules where D = phenothiazine, B = a series of p-phenylene (Ph_n) oligomers, with n = 1-5, and A = perylene-3,4:9,10-bis(dicarboximide)[47], they found that with shorter bridge lengths the increased electronic coupling leads to a larger SOCT-ISC contribution in the recombinant triplet state, D-B-^{3*}A.

In anthracene, the triplet axis system coincides with the lowest electronic transitions and is clearly dictated by the molecular structure, Figure 4.1.[104, 107, 108] Computer simulations of the triplet spectra for **DMJ-^{3*}An** and **DMJ-^{3*}An-tol** indicate that the (e,a,e,a,e,a) ESP phase pattern is the result of the SOCT-ISC coupling mechanism with preferential population of the T_Y sublevel, Figure 4.3A, for $D > 0$, $E < 0$.[99, 112] Thus, charge transfer from **DMJ** to **An** involves moving an electron between two orbitals having a geometry change in the x-z plane as defined in Figure 4.5. Using the right hand rule, this implies that the angular momentum change is along the y direction, so that the SOCT interaction which couples ^{1}(D$^{+\bullet}$-A$^{-\bullet}$) and D-^{3*}A preferentially populates T_Y (i.e., $A_Y > A_{X,Z}$) of D-^{3*}A as is observed in the TREPR spectra of the triplet states of **DMJ-^{3*}An** and **DMJ-^{3*}An-tol**, Table 4.2.[113, 204] Although T_Y is preferentially populated in both cases, there is an increase of the A_X and A_Z population rates in **DMJ-^{3*}An-tol** relative to **DMJ-^{3*}An**. This suggests that conjugation between the anthracene and the phenyl group alters the sublevels in such a way as to relax symmetry restrictions, and further modeling is needed to clarify this result.
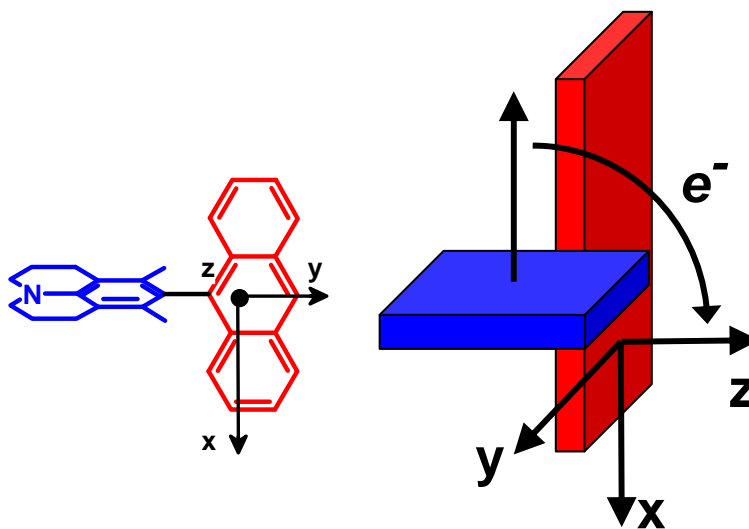
Figure 4.5. Charge transfer from **DMJ** to **An** in **DMJ-An** between orbitals oriented in the x-z plane results in an angular momentum component along y. This angular momentum component coincides with SO-ISC to the corresponding spin sub-levels of ^{3*}An.

4.2.3 Absence of a Triplet State TREPR Spectrum in J-An.

It is particularly surprising that **J-An** does not display a measurable triplet spectrum following photoexcitation despite its obvious similarity to **DMJ-An**. As has been established, SOCT-ISC is the mechanism of triplet formation in **DMJ-^{3*}An** and **DMJ-^{3*}An-tol**. This mechanism requires the ^{1}CT precursor and depends strongly on the orientation of the molecular orbitals involved in the charge transfer as well as the magnitude of the electronic coupling.[64, 66, 67, 104-106] In fact, all of these criteria vary in a clear manner as a function of the difference in θ_1 between **J-An** and **DMJ-An**.

For example, as $\theta_1 \rightarrow 90°$, the degree of charge separation in ^{1}CT increases, Table 4.1. The reported excited-state dipole moment (μ_e) of **J-An** is 16.2 D using an Onsager radius of 6.5 Å.[152] Using the same choice of radius as Herbich[152], μ_e for **DMJ-An** is 25.7 D, nearly a full 10 D larger than the non-methylated species. We estimate the degree of charge separation in the CT state as 26 D/4.8 D esu^{-1} Å^{-1} = 5.4 esu-Å. Using the centers of the spin density distributions in

$DMJ^{+\bullet}$ and $An^{-\bullet}$, $r_{DMJ\text{-}An}$ for a full charge transferred to yield $DMJ^{+\bullet}\text{-}An^{-\bullet}$ is 5.6 Å. Thus, the estimated percentage of charge separation in the CT state is (5.4 esu-Å /5.6 esu-Å) x 100 = 96%. Similarly, the excited state dipole moment in **J-An** measured by Herbich corresponds to ~60% charge separation, Table 4.1. In addition, as θ_1 deviates from 90°, the change in orbital angular momentum which is coupled with this mechanism and critical to the magnitude of the interaction will decrease. Furthermore, even when $\theta_1 \approx 90°$ as in **DMJ-An** and **DMJ-An-tol**, the electronic coupling is sufficient to enable the SOCT-ISC mechanism. This criteria will remain fulfilled even as θ_1 becomes smaller in **J-An**. We conclude that as θ_1 deviates from 90° upon comparing **DMJ-An** to **J-An**, both the degree of charge transfe, and the orientation requirements are affected in a way that decreases the magnitude of the SOCT-ISC interaction, resulting in a negligible amount of **J-^{3*}An** formation.

4.2.4 Participation of the Anthracene LE states in ISC.

The energy levels of CT states depend strongly on both solvent polarity and temperature.[131, 132] As solvent polarity increases, the CT state is stabilized because the solvent dipoles reorient in such a way as to decrease the Coulombic contribution to the CT energy. Alternatively, in non-polar media, solvent reorganization provides minimal stabilization of the CT state and, consequently, the energy gap between ^1CT and ^1LE is decreased. Thus, in order to account for the solvent and temperature dependence of the ^1CT emission of ADMA and its derivatives, it is necessary to include mixing with an energetically proximate, symmetry-allowed ^1LE state (c_{1*A}).[118, 159, 167, 169, 186-188] In addition, because ISC is the process of interest in this study, we must also consider contributions from energetically relevant triplet ^3LE states (c_{3*A}).

The ISC behavior of anthracene and its derivatives has been found to be strongly dependent on substitution of the aromatic core, and this sensitivity is derived from changes in the relative energy ordering of the ^{1}LE (S_1) and ^{3}LE (T_2) energy levels. As discussed earlier, the high yield of ISC in unsubstituted anthracene is a consequence of the fact that the S_1 state is slightly above the T_2 state ($S_1 \rightarrow T_2 \rightarrow T_1$). Generally, this ordering remains the same for all substitutions except at the 9- and 10-positions where there is a reversal in energy ordering as the S_1 state is lowered relative to the T_2 state.[174, 177, 182, 183] Furthermore, the S_1 state decreases in energy as the conjugation between the substituents and the anthracene increases (S_1 of diphenyl- < phenyl- < methyl-). It is this energy level reversal that is responsible for the dramatic decrease in the ISC rate between anthracene and 9,10-diphenylanthracene.[174, 178] If we consider the julolidine moiety as a 9-position substitution to the anthracene, the ^{1}LE (S_1) is expected to be slightly below ^{3}LE (T_2) and will vary as a function of conjugation, i.e., θ_1 will effectively modulate the contribution from c_{1*A} and c_{3*A} to Ψ_{CT} by varying the degree of electronic delocalization between the donor cation and the acceptor anion groups. For example, as $\theta_1 \rightarrow 0°$, delocalization is maximized and the wave functions of the pure LE states become poor representations of the system. Consequently, their respective contributions to Ψ_{CT} are minimized. Thus, mixing with the pure LE states of anthracene is expected to decrease in **J-An** and **DMJ-An-tol** relative to **DMJ-An** as a result of stabilization by conjugation with the 9- or 9,10-substitutions.

In this work, photoexcitation at 416 nm directly excites the ^{1}CT transition which, at room temperature (2.89 eV), is ~0.35 eV below the pure LE S_1 (3.28 eV) or T_2 (3.22 eV) states of anthracene.[183, 193] Under these conditions SOCT-ISC via T_2 (similar to anthracene) becomes a strongly activated process. However, our results were obtained at 85 K in a frozen toluene

matrix where the solvent reorganization is inhibited and the ^{1}CT energy is higher because it is no longer stabilized. CT emission measurements indicate an increase of ~0.15-0.2 eV in the ^{1}CT energy levels upon cooling from 297 K to 77 K in MTHF, Figure 4.6. Although the destabilization energy resulting from freezing out solvent reorganization is not enough to raise the ^{1}CT energy level above the T_2 energy level of anthracene, it does serve to decrease the energy gap which weights the coupling between the ^{1}CT and ^{3}LE states. This will increase the contribution from c_{3*A} in Eq. 1 and because of the energetic proximity of the T_2 triplet state, the magnitude of the $\langle ^1(D^{+\bullet}\text{-}A^{\bullet}) \, | \, \mathcal{H}_{SOCT} \, | \, D\text{-}^{3*}A \rangle$ interaction should also be increased. In addition, direct mixing with the ^{3}LE(T_1) state may also be present; however, its contribution is likely small since the $|D|$ and $|E|$ values for **DMJ-^{3*}A** are only weakly perturbed from those of unsubstituted **^{3*}An**, Table 4.2.[153]
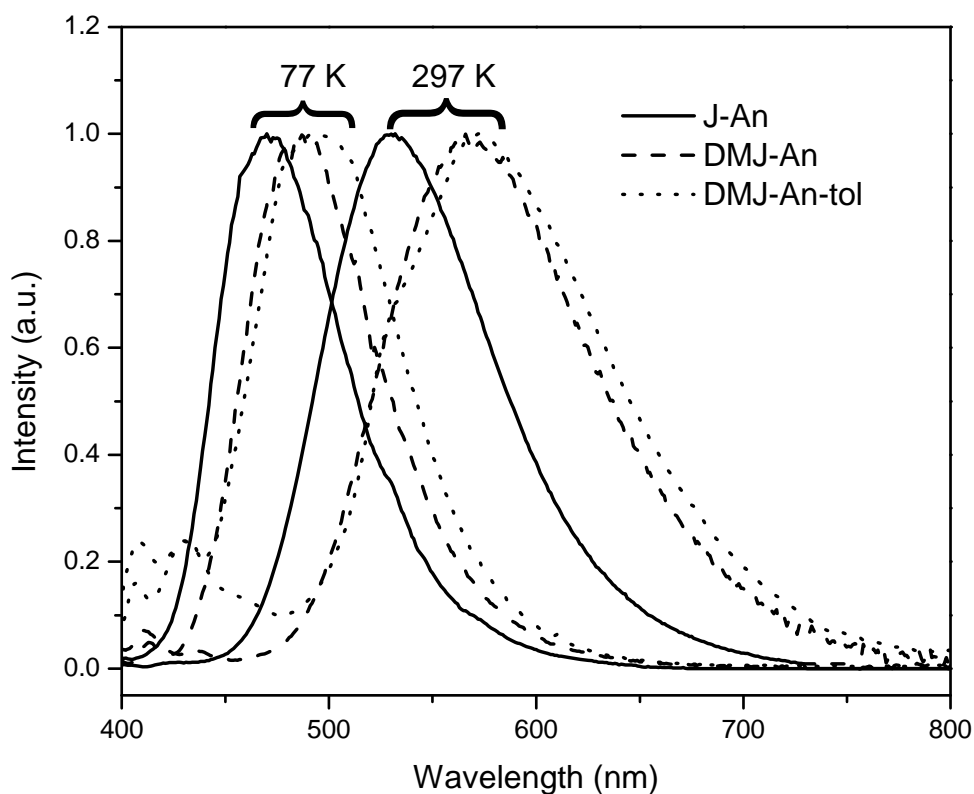
Figure 4.6. Emission spectra of **J-An** (solid), **DMJ-An** (dashed), and **DMJ-An-tol** (dotted) in MTHF at 297 and 77 K.

4.3 Conclusions

TREPR studies show that the primary mechanism of triplet formation in **DMJ-An** and **DMJ-An-tol** following photoexcitation is a spin-orbit coupling mechanism which is similar to an n-π^* electronic transition within a single chromophore. The SOCT-ISC mechanism is characterized by the (e,a,e,a,e,a) ESP phase pattern of the **DMJ-^{3*}An** and **DMJ-^{3*}An-tol** TREPR spectra and depends on the degree of charge separation, the relative orientation of the orbitals involved in the charge transfer, and the magnitude of the electronic coupling between the

donor and acceptor. In **J-An**, **DMJ-An** and **DMJ-An-tol**, where the donor and acceptor are formally linked by a single bond, the torsional angle (θ_1) between the π system of the anthracene and the nitrogen lone pair of the julolidine determines all of these parameters.

Despite its similar structure, **J-An** does not display a measurable triplet spectrum following photoexcitation. This result is a function of a decrease in θ_1 due to the absence of the 3 and 5 methyl groups on julolidine. Although the change in θ_1 between **J-An** and **DMJ-An** is not very large (~15°-20°), this difference serves to decrease the SOCT-ISC contribution in two distinct ways. As θ_1 deviates from 90°, 1) the degree of charge transfer decreases and 2) the change in orbital angular momentum which drives SOCT-ISC decreases. Furthermore, it is also likely that mixing with the pure LE states of anthracene is decreased in **J-An** and **DMJ-An-tol** as a result of conjugation with the 9- or 9,10-substituents. Despite this, the presence of a spin-polarized triplet state in **DMJ-An-tol** (and the absence of a triplet in **J-An**) indicates that this mixing does not play as significant a role in the ISC as the degree of charge transfer and the orientational requirements. Although TREPR can give quantitative information with respect to many properties such as relative sublevel populations and unpaired spin distribution, it is difficult to quantify the overall triplet yield with this technique. Work is in progress to clarify the temperature dependent and solvent dependent spin dynamics on both the anisotropic ISC behavior as well as the triplet yields in these systems.

Chapter 5

Experimental Methods

5.1 Time-Resolved EPR Spectroscopy

TREPR measurements were made using a Bruker Elexsys E580 X-Band EPR spectrometer. The temperature was controlled by an Oxford Instruments CF935 continuous flow cryostat using liquid nitrogen or helium. Samples were photoexcited at 532 nm or 416 nm using the output from a frequency doubled or frequency tripled, H_2-Raman shifted, respectively, Nd:YAG laser (1-2 mJ/pulse, 7 ns, 10 Hz, QuantaRay DCR-2). The polarization of the laser was set to 54.7° relative to the direction of the static magnetic field to avoid magnetophotoselection effects on the spectra. Microwave signals in emission (*e*) and/or enhanced absorption (*a*) were detected in both the real and the imaginary channels (quadrature detection). Sweeping the magnetic field gave 2D complex spectra versus time and magnetic field. The spectra were subsequently phased into a Lorentzian part and a dispersive part, and the former, also known as the imaginary magnetic susceptibility χ'', is presented.

Simulation of the powder-pattern spectra of the spin-polarized RP signals and the triplet states resulting from CR was performed using a home-written MATLAB™ program[205] following published procedures.[81, 206]

5.1.1 Transient Continuous Wave

TREPR measurements using continuous wave (CW) microwaves and direct detection were made using a Bruker Elexsys E580 X-Band EPR spectrometer outfitted with a variable Q dielectric resonator (ER-4118X-MD5-W1). Following photoexcitation, kinetic traces of transient magnetization were accumulated under CW microwave irradiation (typically 6-20 mW). The field modulation was disabled to achieve a time response of $Q/\pi\nu \approx 40$ ns, where Q is

the quality factor of the resonator and ν is the resonant frequency, while microwave signals in emission (*e*) and/or enhanced absorption (*a*) were detected in both the real and the imaginary channels (quadrature detection). Sweeping the magnetic field gave 2D complex spectra versus time and magnetic field. For each kinetic trace, the signal acquired prior to the laser pulse was subtracted from the data. Kinetic traces recorded at magnetic field values off-resonance were considered background signals, whose average was subtracted from all kinetic traces.

5.1.2 Electron Spin Echo

TREPR field-swept electron spin echo (ESE) measurements of the triplet EPR spectra were made using a Bruker Elexsys E580 X-Band EPR spectrometer outfitted with a variable Q dielectric resonator (ER-4118X-MD4-W1). High power microwave pulses were generated by a 1-kW TWT amplifier (Applied Systems Engineering 117X). The typical length of a $\pi/2$ pulse was 8 ns. The resonator was fully over-coupled to achieve $Q < 200$ and a dead time of ~68 ns.

In the basic Hahn-echo technique,[9] the FID signal generated with the first 8-ns $\pi/2$ pulse is refocused by a second 16-ns π pulse. The time between the two microwave pulses was 68 ns, so that the spin echo appears 68 ns following the second microwave pulse. The microwave pulse sequence begins after the triplet state is created by the laser pulse. Following photoexcitation, the integral of the echo intensity at a given delay time at each magnetic field value gives the spectrum of the spin-polarized triplets. Microwave signals in emission (e) and/or enhanced absorption (a) were detected in both the real and the imaginary channels (quadrature detection). Four-step phase cycling was performed in order to suppress artifacts due to imbalances in the quadrature detection. Sweeping the magnetic field gave 2D complex spectra versus time and

magnetic field. The spectra were subsequently phased into a Lorentzian part and a dispersive part, and the former, also known as the imaginary magnetic susceptibility χ'', is presented.

5.2 Steady State Spectroscopy

Ground state absorption measurements were made on a Shimadzu UV-1601 spectrophotometer. The room temperature optical density of all samples was maintained between 0.8 and 1.5 at 532 nm ($\varepsilon_{PDI,532\ nm} = 30500\ M^{-1}\ cm^{-1}$) for PTZ-Ph$_n$-PDI compounds and 416 nm for DMJ-An-Ph$_n$-NI and compounds.[29]

5.3 Time Resolved Fluorescence Anisotropy Spectroscopy

Time-resolved fluorescence data were collected using a home-built cavity-dumped Ti:sapphire oscillator[207] coupled to a streak camera detection system (Hamamatsu C4334 Streakscope). The produced 24-µJ laser pulses at 791 nm with an 825-kHz repetition rate and ~30-fs pulse-duration. The laser pulses were frequency doubled in a nonlinear crystal (0.3 mm BBO) to produce 395 nm excitation pulses that were attenuated with a half-wave plate and polarizer to 60-600 pJ/pulse before the sample. Synchronization between the laser pulse train and the streak camera was provided by the acousto-optic cavity dumper (NEOS N13389, N64389-SYN) and a photodiode-discriminator combination that detected the intracavity repetition rate of the laser (82 MHz). The illumination and collection optics were in a standard 90° geometry with the polarization of the excitation pulses and the detected fluorescence controlled by broadband polarizers.[90] The anisotropy, r, was calculated according to:

$$r = \frac{I_{\parallel} - I_{\perp}}{I_{\parallel} + 2I_{\perp}} = \frac{I_{VV} - CI_{VH}}{I_{VV} + 2CI_{VH}}$$

where I_{VV} (I_{VH}) is the time-dependent intensity of the vertically (horizontally) polarized emission excited with vertically polarized light and C is the relative sensitivity of the detection system to vertically and horizontally polarized emission.[90] C is calculated using the unpolarized emission that occurs with horizontal excitation: $C = I_{HV} / I_{HH}$. Fluorescence lifetimes and anisotropy decay times were determined by nonlinear least-squares fitting including deconvolution of the instrument response of the streak camera (0.043 ns for a 2-ns time window, and 0.40 ns for a 20-ns time window). Room temperature measurements were performed on dilute samples (A_{547} < 0.08) in a 10-mm cuvette. Low-temperature measurements were performed in a cryostat (see below) with front-face illumination of the concentrated sample of **5** (A_{547} = 1.0, A_{391} = 0.19). The concentrated sample was chosen in order to reproduce the conditions of the EPR and low-temperature absorption samples. At room temperature, the concentrated sample of **5** in the cryostat cell exhibited identical kinetics to the dilute sample in the cuvette.

5.4 Temperature Dependent Optical Spectroscopy

For variable temperature UV-vis and time-resolved fluorescence experiments, a liquid nitrogen-cooled optical dewar (Janis Research VPS-100) was utilized. Each sample was loaded into a sealed optical cell with ~2-3 mm path length constructed from two transparent quartz windows and a Viton O-ring spacer. The sample holder was seated in the dewar, which was then evacuated to ~10^{-5} Torr. Sample temperature was maintained to within ± 0.5 K by a Lake Shore Cryotronics model DRC-82C temperature controller.[30] The sample was allowed to equilibrate for 30 minutes at each temperature prior to photolysis.

5.5 Computational Methods

DFT geometry optimizations of individual chromophores and Ph_n (n = 2-4) in both their singlet and triplet states were performed in the Gaussian 98 program package[208] employing Becke's three-parameter hybrid functional using the Lee, Yang, and Parr correlation functional (B3LYP)[149, 150] and the 6-31G* basis set. No symmetry constraints were enforced and all open-shell calculations were performed using unrestricted methods.   The spin contamination (deviation from true $<S^2>$) in the triplet species was found to deviate from the expected value by less than 3%.

5.6 Nanosecond Transient Absorption Spectroscopy

All samples were subjected to five freeze-pump-thaw degassing cycles and kept in an airtight cuvette for the duration of the experiment. The samples were excited with 5 ns, 0.5 - 2 mJ laser pulses focused to a 5 mm diameter spot.   The pulses were produced using the frequency-tripled output of a Continuum 8000 Nd-YAG laser to pump a Continuum Panther OPO. The probe light was generated using a xenon flashlamp (EG&G Electro-Optics FX-200) and detected using a photomultiplier tube (Hamamatsu R928) after dispersion by a monochromator with high voltage applied to only 4 dynodes. The total instrument response time is 7 ns and is determined primarily by the laser pulse duration. Between 50 and 100 shots were averaged per kinetic trace with a LeCroy 9384 digital oscilloscope and sent to a microcomputer, which calculated the ΔA. Kinetic analyses were performed using a nonlinear least squares fit to a general sum-of-exponentials using the Levenberg-Marquardt algorithm accounting for the presence of the finite instrument response.

5.7 Femtosecond Transient Absorption Spectroscopy

Femtosecond transient absorption measurements were performed with the following apparatus: A Spectra-Physics Millenium V frequency-doubled CW Nd:YVO$_4$ laser was used to pump a Coherent MIRA Ti:sapphire oscillator. The 110 fs, 828-nm pulses from the oscillator were stretched to ~200 ps using a four-pass, reflective, single-grating pulse stretcher and were used to seed a homemade regenerative amplifier, which includes a Medox two-step Pockels cell and driver. The amplifier was pumped at a 2 kHz repetition rate by a Quantronix 527DP frequency-doubled Nd:YLF laser (4.1 mJ/pulse). The amplified Ti:sapphire pulse (0.5 mJ/pulse) was recompressed to approximately 120 fs by a four-pass, reflective, single grating compressor. The pulse energy after compression was 320 μJ/pulse. Two 5% reflective beam splitters were placed in the output path to generate two 828-nm beams for white light generation. The remaining 828-nm light was frequency doubled by using a 1-mm-type I LBO crystal to give 414-nm 120-fs, 75-μJ pulses.[209] The 828-nm light from the first 5% beam splitter was passed through a waveplate-polarizer pair to control its intensity, and a few microjoules were focused into a 1-mm sapphire disk to generate white light continuum pulses. All reflective optics were used both to focus the 828-nm pulse into the sapphire and recollimate the white light output, thus limiting the chirp on the white light pulse to <200 fs from 450 to 750 nm. The 828-nm light from the second 5% beam splitter was used to create a second white light continuum by focusing the 828-nm pulse into a 2-mm sapphire disk, using a 100 mm focal length (f.l.) lens. This white light was used to seed the first stage of a two-stage optical parametric amplifier, which has been described previously.[210] The first stage contains a Type II BBO crystal, which was pumped with about 20 μJ of 414-nm light focused into the crystal with a 300 mm f.l. lens. After removal the IR idler beam and residual 414-nm pump light, the first stage produced transform-limited pulses

having ~1.0 μJ/pulse from 460 to 750 nm. This light was then focused into the Type I BBO

of the second stage of the OPA with a 75 mm f.l. lens. The second stage amplifies the first stage

light upon overlap with the remaining 55 μJ/pulse of 414 nm pump light. The final amplified

pulse energy was ~7.5 μJ/pulse after filtering out the residual 414-nm and IR idler light. The

optical path for the probe beam and the chopping scheme used in the pump-probe experiments

were described by Lukas et al.[209], and the polarization of the pump and probe beams was set to

differ by 54.7° before reaching the sample. The instrument was outfitted with a CCD array

detector (Ocean Optics PC2000) for simultaneous collection of spectral and kinetic data.[88]

Kinetic analyses were performed at several wavelengths using a Levenberg-Marquardt nonlinear

least squares fit to a general sum-of-exponentials function with an added Gaussian to account for

the finite instrument response.

5.8 Magnetic Field Effect Experiment

For the magnetic field effect experiment, the sample holder or the cryostat was placed

between the poles of a Walker Scientific HV-4W electromagnet powered by a Walker Magnion

HS-735 power supply. The field strength was measured by a Lakeshore 450 gaussmeter with a

Hall effect probe. Both the electromagnet and the gaussmeter were interfaced with the data

collection computer, allowing measurement and control of the magnetic field to 1x10-5 T during

data acquisition. Due to the length of the sample runs (> 3 hr) a small amount of sample

degradation was observed, resulting in a variation in the triplet yield/radical pair

population/recombination rate at zero field, A(B=0), over the course of the experiments. To

compensate for this, the magnetic field was reset to B = 0 mT every three kinetic traces and

A(B=0) was plotted and fit with a polynomial or series of polynomials. These functions were used to calculate the relative yield/population/rate as a function of applied field strength:

$$\frac{T}{T_0} = \frac{\Delta A(B)}{\Delta A(B = 0)}$$

The results presented are an average of three or more experiments conducted on separate days with freshly prepared samples in spectrophotometric or freshly distilled ACS grade solvent.

Due to the copper casing of the sample cell within the cryostat setup, the sample experiences a magnetic field ~19% less than it would outside the cell. Therefore the value of 2J obtained at room temperature within the cryostat setup (Chapter 6) is greater than that obtained in the original MFE experiment (Chapter 5). The same is true for the temperature controlled cell used for the MFEs in Chapter 10, except here the sample experiences a magnetic field ~26% less than it would outside the cell. In this case, the 2J values presented are scaled to match that measured at room temperature outside the cell.

References

1.   Wigley, T. M. L.; Richels, R.; Edmonds, J. A., *Nature (London)* **1996,** 379, (6562), 240-243.

2.   Lewis, N. S.; Nocera, D. G., *Proc. Natl. Acad. Sci. U. S. A.* **2006,** 103, (43), 15729-15735.

3.   *Energy Information Administration (2005) Annual Energy Outlook. (US Dept of Energy, Washington, DC).*

4.   Shaheen, S. E.; Ginley, D. S.; Jabbour, G. E., *Mater. Res. Bull.* **2005,** 30, (1), 10-19.

5.   Aviram, A.; Ratner, M. A., *Chem. Phys. Lett.* **1974,** 29, 277-283.

6.   Joachim, C.; Ratner, M. A., *Proc. Natl. Acad. Sci. U. S. A.* **2005,** 102, (25), 8800-8800.

7.   Davis, W. B.; Svec, W. A.; Ratner, M. A.; Wasielewski, M. R., *Nature* **1998,** 396, (6706), 60-63.

8.   Miller, S. E.; Lukas, A. S.; Marsh, E.; Bushard, P.; Wasielewski*, M. R., *Journal of the American Chemical Society* **2000,** 122, 7802-7810.

9.   Lin, T. S., *Chem. Rev.* **1984,** 84, (1), 1-15.

10.   Yagi, M.; Shirai, H.; Ohta, J.; Higuchi, J., *Chem. Phys. Lett.* **1989,** 160, (1), 13-16.

11.   Kamata, Y.; Akiyama, K.; Tero-Kubota, S., *J. Phys. Chem. A* **1999,** 103, (12), 1714-1718.

12.   Levanon, H.; Galili, T.; Regev, A.; Wiederrecht, G. P.; Svec, W.; Wasielewski, M. R., *Journal of the American Chemical Society* **1998,** 120, 6366-6373.

13.   Dance, Z. E. X.; Mi, Q. X.; McCamant, D. W.; Ahrens, M. J.; Ratner, M. A.; Wasielewski, M. R., *J. Phys. Chem. B* **2006,** 110, (50), 25163-25173.

14.   Wiederrecht, G. P.; Svec, W. A.; Wasielewski, M. R., *J. Am. Chem. Soc.* **1999,** 121, (33), 7726-7727.

15.   Kawai, A.; Okutsu, T.; Obi, K., *Chem. Phys. Lett.* **1995,** 235, (5-6), 450-455.

16.   Parson, W. W.; Scherz, A.; Warshel, A., *Springer Series in Chemical Physics (1985), 42 (Antennas React. Cent. Photosynth. Bact.)* **1985,** 42, 122-130.

17.   Jortner, J.; Ratner, M. A., Blackwell: London, 1997.

18.   Bixon, M.; Jortner, J., *Adv. Chem. Phys.* **1999,** 106, (Electron Transfer: From Isolated Molecules to Biomolecules, Pt. 1), 35-202.

19.   Jortner, J.; Bixon, M.; Langenbacher, T.; Michel-Beyerle, M. E., *Proc. Natl. Acad. Sci. USA* **1998,** 95, 12759-12765.

20.   Berlin, Y. A.; Burin, A. L.; Ratner, M. A., *Chem. Phys.* **2002,** 275, 61-74.

21.   Berlin, Y. A.; Burin, A. L.; Ratner, M. A., *J. Phys. Chem. A* **2000,** 104, (3), 443-445.

22.   Berlin, Y. A.; Hutchison, G. R.; Rempala, P.; Ratner, M. A.; Michl, J., *J. Phys. Chem A* **2003,** 107, (19), 3970-3980.

23.   Troisi, A.; Ratner, M. A., *Molecular Nanoelectronics* **2003**, 1-18.

24.   Segal, D.; Nitzan, A.; Davis, W. B.; Wasielewski, M. R.; Ratner, M. A., *J. Phys. Chem. B* **2000,** 104, (16), 3817-3829.

25.   Segal, D.; Nitzan, A.; Ratner, M. A.; Davis, W. B., *J. Phys. Chem. B* **2000,** 104, 2790-2793.

26.   Paulson, B. P.; Miller, J. R.; Gan, W.-X.; Closs, G. L., *J. Am. Chem. Soc.* **2005,** 127, 4860-4868.

27.   De la Torre, G.; Giacalone, F.; Segura, J. L.; Martin, N.; Guldi, D. M., *Chem.--Eur. J.* **2005,** 11, (4), 1267-1280.

28.   Giacalone, F.; Segura, J. L.; Martin, N.; Guldi, D. M., *J. Am. Chem. Soc.* **2004,** 126, (17), 5340-5341.

29.   Weiss, E. A.; Ahrens, M. J.; Sinks, L. E.; Gusev, A. V.; Ratner, M. A.; Wasielewski, M. R., *J. Am. Chem. Soc.* **2004,** 126, 5577-5584.

30.   Weiss, E. A.; Tauber, M. J.; Kelley, R. F.; Ahrens, M. J.; Ratner, M. A.; Wasielewski, M. R., *J. Am. Chem. Soc.* **2005,** 127, (33), 11842-11850.

31.   Weiss, E. A.; Tauber, M. J.; Ratner, M. A.; Wasielewski, M. R., *J. Am. Chem. Soc.* **2005,** 127, (16), 6052-6061.

32.   Anderson, P. W., *Phys. Rev.* **1959,** 115, (1), 2-13.

33.   Anderson, P. W., *Phys. Rev.* **1950,** 79, (2), 350-356.

34.   Kramers, H. A., *Physica* **1934,** 1, 182-192.

35.   Marcus, R. A., *J. Chem. Phys.* **1965,** 43, 679-701.

36.   Jortner, J., *J. Chem. Phys.* **1976,** 64, (12), 4860-4867.

37.   Kobori, Y.; Sekiguchi, S.; Akiyama, K.; Tero-Kubota, S., *J. Phys. Chem. A* **1999,** 103, 5416-5424.

38.   Paddon-Row, M. N.; Shephard, M. J., *J. Phys. Chem. A* **2002,** 106, (12), 2935-2944.

39.   Volk, M.; Haberle, T.; Feick, R.; Ogrodnik, A.; Michel-Beyerle, M. E., *J. Phys. Chem.* **1993,** 97, (38), 9831-9836.

40.   Closs, G. L.; Miller, J. R., *Science* **1988,** 240, (4851), 440-447.

41.   Yamashita, J.; Kondo, J., *Phys. Rev.* **1958,** 109, (3), 730-741.

42.   Feher, G.; Okamura, M. In *Tunneling In Biological Systems*, Tunneling Conference, New York, 1979; Chance, B.; Devault, D.; Frauenfelder, H.; Marcus, R. A.; Schreiffer, J. R.; Sutin, N., Eds. Academic Press: New York, 1979; pp 729-743.

43.   Lukas, A. S.; Bushard, P. J.; Weiss, E. A.; Wasielewski, M. R., *J. Am. Chem. Soc.* **2003,** 125, 3921-3930.

44.   Weiss, E. A.; Ratner, M. A.; Wasielewski, M. R., *J. Phys. Chem. A* **2003,** 107, (19), 3639-3647.

45.   Goldsmith, R. H.; Sinks, L. E.; Kelley, R. F.; Betzen, L. J.; Liu, W. H.; Weiss, E. A.; Ratner, M. A.; Wasielewski, M. R., *Proc. Natl. Acad. Sci. U. S. A.* **2005,** 102, (10), 3540-3545.

46.   Weiss, E. A.; Tauber, M. J.; Ratner, M. A.; Wasielewski, M. R., *J. Am. Chem. Soc.* **2005,** 127, (16), 6052-6061.

47.   van der Boom, T.; Hayes, R. T.; Zhao, Y.; Bushard, P. J.; Weiss, E. A.; Wasielewski, M. R., *J. Am. Chem. Soc.* **2002,** 124, 9582-9590.

48.   Weller, A.; Staerk, H.; Treichel, R., *Faraday Discuss. Chem. Soc.* **1984,** 78, 271-278.

49.   Hoff, A. J.; Gast, P.; van der Vos, R.; Franken, E. M.; Lous, E. J., *Z. Phys. Chem.* **1993,** 180, 175-192.

50.   Till, U.; Hore, P. J., *Molec. Phys.* **1997,** 90, (2), 289-296.

51.   Steiner, U. E.; Ulrich, T., *Chem. Rev.* **1989,** 89, 51-147.

52.   Schulten, K.; Staerk, H.; Weller, A.; Werner, H.-J.; Nickel, B., *Z. Phys. Chem.* **1976,** 101, 371-390.

53.   Tanimoto, Y.; Okada, N.; Itoh, M.; Iwai, K.; Sugioka, K.; Takemura, F.; Nakagaki, R.; Nagakura, S., *Chem. Phys. Lett.* **1987,** 136, (1), 42-46.

54.   Sakaguchi, Y.; Hayashi, H., *J. Phys. Chem. A* **1997,** 101, 549-555.

55.   Werner, U.; Kuhnle, W.; Staerk, H., *J. Phys. Chem.* **1993,** 97, 9280-9287.

56.   Tadjikov, B.; Smirnov, S., *Phys. Chem. Chem. Phys.* **2001,** 3, (2), 204-212.

57.   Tsentalovich, Y. P.; Morozova, O., B.; Avdievich, N. I.; Ananchenko, G. S.; Yurkovskaya, A. V.; Ball, J. D.; Forbes, M. D. E., *J. Phys. Chem. A* **1997,** 101, (47), 8809-8816.

58.   Blankenship, R. E.; Schaafsma, T. J.; Parson, W. W., *Biochim. Biophys. Acta* **1977,** 461, 297-305.

59.   Plato, M.; Moebius, K.; Michel-Beyerle, M. E.; Bixon, M.; Jortner, J., *J. Am. Chem. Soc.* **1988,** 110, (22), 7279-7285.

60.   Werner, H.-J.; Schulten, K.; Weller, A., *Biochim. Biophys. Acta* **1978,** 502, 255-268.

61.   Norris, J. R.; Bowman, M. K.; Budil, D. E.; Tang, J.; Wraight, C. A.; Closs, G. L., *Proc. Natl. Acad. Sci. USA* **1982,** 79, 5532-5536.

62.   Shultz, D. A.; Fico, R. M., Jr.; Bodnar, S. H.; Kumar, R. K.; Vostrikova, K. E.; Kampf, J. W.; Boyle, P. D., *J. Am. Chem. Soc.* **2003,** 125, (38), 11761-11771.

63.   Okada, T.; Karaki, I.; Matsuzawa, E.; Mataga, N.; Sakata, Y.; Misumi, S., *J. Phys. Chem.* **1981,** 85, (26), 3957-3960.

64.   Wasielewski, M. R.; Johnson, D. G.; Svec, W. A.; Kersey, K. M.; Minsek, D. W., *J. Am. Chem. Soc.* **1988,** 110, (21), 7219-7221.

65.   van Willigen, H.; Jones, G., II; Farahat, M. S., *J. Phys. Chem.* **1996,** 100, (9), 3312-3316.

66.   Gould, I. R.; Boiani, J. A.; Gaillard, E. B.; Goodman, J. L.; Farid, S., *J. Phys. Chem. A* **2003,** 107, (18), 3515-3524.

67.   Khudyakov, I. V.; Serebrennikov, Y. A.; Turro, N. J., *Chem. Rev. (Washington, DC, U. S.)* **1993,** 93, (1), 537-570.

68.   Hasharoni, K.; Levanon, H.; Greenfield, S. R.; Gosztola, D. J.; Svec, W. A.; Wasielewski, M. R., *J. Am. Chem. Soc.* **1995,** 117, (30), 8055-8056.

69.   Schweiger, A.; Jeschke, G., Oxford: Oxford, 2001.

70.   Hore, P. J.; Hunter, D. A.; McKie, C. D.; Hoff, A. J., *Chem. Phys. Lett.* **1987,** 137, 495-500.

71.   Closs, G. L.; Forbes, M. D. E.; James R. Norris, J., *J. Phys. Chem.* **1987,** 91, (13), 3592-3599.

72.   Norris, J. R.; Morris, A. L.; Thurnauer, M. C.; Tang, J., *J. Chem. Phys.* **1990,** 92, 4239-4249.

73.   Hasharoni, K.; Levanon, H.; Gersdorff, J. v.; Kurreck, H.; Möbius, K., *J. Chem. Phys.* **1993,** 98, (4), 2916-2926.

74.   Hasharoni, K.; Levanon, H.; Greenfield, S. R.; Gosztola, D. J.; Svec, W. A.; Wasielewski, M. R., *J. Am. Chem. Soc.* **1996,** 118, 10228-10235.

75.   Carbonera, D.; DiValentin, M.; Corvaja, C.; Agostini, G.; Giacometti, G.; Liddell, P. A.; Kuciauskas, D.; Moore, A. L.; Moore, T. A.; Gust, D., *J. Am. Chem. Soc.* **1998,** 120, (18), 4398-4405.

76.   Levanon, H.; Galili, T.; Regev, A.; Wiederrecht, G. P.; Svec, W. A.; Wasielewski, M. R., *J. Am. Chem. Soc.* **1998,** 120, (25), 6366-6373.

77.   Shaakov, S.; Galili, T.; Stavitski, E.; Levanon, H.; Lukas, A.; Wasielewski, M. R., *J. Am. Chem. Soc.* **2003,** 125, (21), 6563-6572.

78.   Levanon, H.; Norris, J. R., *Chem. Rev.* **1978,** 78, 185-198.

79.   Hutchinson, C. A.; Mangum, B. W., *J. Chem. Phys.* **1958,** 29, (4), 952-953.

80.   Hutchinson, C. A.; Mangum, B. W., *J. Chem. Phys.* **1961,** 34, (3), 908-922.

81.   Wasserman, E.; Snyder, L. C.; Yager, W. A., *J. Chem. Phys.* **1964,** 41, (6), 1763-1772.

82.   Blank, A.; Levanon, H., *Concepts in Magnetic Resonance Part A* **2005,** 25A, (1), 18-39.

83.   Tauber, M. J.; Giaimo, J. M.; Kelley, R. F.; Rybtchinski, B.; Wasielewski, M. R., *J. Am. Chem. Soc.* **2006,** 128, 1782-1783.

84.   Clarke, D.; Gilbert, B. C.; Hanson, P., *Journal of the Chemical Society, Perkin Transactions 2: Physical Organic Chemistry (1972-1999)* **1976**, (1), 114-124.

85.   Adrian, F. J., *J. Chem. Phys.* **1972,** 57, (12), 5107-5113.

86.   Atherton, N. M., Time-resolved ESR: spin polarization. In *Principles of Electron Spin Resonance*, Horwood, E., Ed. Ellis Horwood Limited: Chichester, West Sussex, 1993.

87.   Gonen, O.; Levanon, H., *J. Phys. Chem.* **1985,** 89, 1637-1643.

88.   Giaimo, J. M.; Gusev, A. V.; Wasielewski, M. R., *J. Am. Chem. Soc.* **2002,** 124, 8530-8531.

89.   Myers-Kelley, A., *J. Chem. Phys.* **2003,** 119, (6), 3320-3331.

90.   Lakowicz, J. R., Kluwer: Dordrecht, 1999.

91.   Assael, M. J.; Dalaouti, N. K.; Dymond, J. H., *Int. J. Thermophys.* **2000,** 21, (2), 291-299.

92.   Barlow, A. J.; Lamb, J.; Matheson, A. J., *Proc. R. Soc. London, A* **1966,** 292, (1430), 322-342.

93.   Hayashi, H., World Scientific: Singapore, 2004; p 250 pp.

94.   Marcus, R. A., *J. Chem. Phys.* **1956,** 24, 966-978.

95.   Ford, W. E.; Kamat, P. V., *J. Phys. Chem.* **1987,** 91, 6373-6380.

96.   Kasha, M.; Rawles, H. R.; El-Bayoumi, M. L., *Pure Appl. Chem* **1965,** 11, 371-392.

97.   Dutton, P. L.; Leigh, J. S.; Reed, D. W., *Biochim. Biophys. Acta* **1973,** 292, (3), 654-664.

98.   Dutton, P. L.; Leigh, J. S.; Seibert, M., *Biochem. Biophys. Res. Commun.* **1972,** 46, (2), 406-413.

99.   Thurnauer, M. C., *Reviews of Chemical Intermediates* **1979,** 3, 197-230.

100.   Weissman, S. I., *Acc. Chem. Res.* **1973,** 6, 233-238.

101.   Yamauchi, S., *Bull. Chem. Soc. Jpn.* **2004,** 77, (7), 1255-1268.

102.   Yamauchi, S.; Takahashi, A.; Iwasaki, Y.; Unno, M.; Ohba, Y.; Higuchi, J.; Blank, A.; Levanon, H., *J. Phys. Chem. A* **2003,** 107, (10), 1478-1485.

103.   Lim, B. T.; Okajima, S.; Chandra, A. K.; Lim, E. C., *Chem. Phys. Lett.* **1981,** 79, (1), 22-27.

104.   El-Sayed, M. A., *J. Chem. Phys.* **1974,** 60, (11), 4502-4507.

105.   Salem, L.; Rowland, C., *Angew. Chem., Int. Ed. Engl.* **1972,** 11, (2), 92-111.

106.   Morais, J.; Hung, R. R.; Grabowski, J. J.; Zimmt, M. B., *J. Phys. Chem.* **1993,** 97, (50), 13138-13144.

107.   Siegel, S.; Goldstein, L., *J. Chem. Phys.* **1965,** 43, 4185-4187.

108.   Siegel, S.; Judeikis, H. S., *J. Phys. Chem.* **1965,** 70, (7), 2205-2211.

109.   Hutchinson, C. A., Magnetic Resonance Spectra of Organic Molecules in Triplet States in Single Crystals. In *The Triplet State*, Zahlan, A. B., Ed. University Press: Cambridge, 1967; pp 63-100.

110.   Thurnauer, M. C.; Norris, J. R., *Chem. Phys. Lett.* **1977,** 47, (1), 100-105.

111.   Siegel, S.; Judeikis, H. S., *J. Phys. Chem.* **1966,** 70, (7), 2201-2204.

112.   Thurnauer, M. C.; Katz, J. J.; Norris, J. R., *Proc. Natl. Acad. Sci. U. S. A.* **1975,** 72, (9), 3270-3274.

113.   van der Waals, J. H.; de Groot, M. S., Magnetic interactions related to phosphorescence. In *The Triplet State*, Zahlan, A. B., Ed. University Press: Cambridge, 1967; pp 101-132.

114.   El-Sayed, M. A., Double resonance techniques and relaxation mechanisms involving the lowest triplet state of aromatic compounds. In *Excited States*, Lim, E. C., Ed. Academic Press: New York, 1974; Vol. 1, pp 35-77.

115.   Katsuki, A.; Kobori, Y.; Tero-Kubota, S.; Milikisyants, S.; Paul, H.; Steiner, U. E., *Mol. Phys.* **2002,** 100, 1245-1259.

116.   Santos, F. J. V.; Nieto de Castro, C. A.; Dymond, J. H.; Dalaouti, N. K.; Assael, M. J.; Nagashima, A., *J. Phys. Chem. Ref. Data* **2006,** 35, (1), 1-8.

117.   Weiss, E. A.; Ahrens, M. J.; Sinks, L. E.; Gusev, A. V.; Ratner, M. A.; Wasielewski, M. R., *J. Am. Chem. Soc.* **2004,** 126, 5577-5584.

118.   Herbich, J.; Kapturkiewicz, A., *Chem. Phys. Lett.* **1997,** 273, 9-17.

119.   Kobori, Y.; Yamauchi, S.; Akiyama, K.; Tero-Kubota, S.; Imahori, H.; Fukuzumi, S.; Norris, J. R., Jr., *Proc. Natl. Acad. Sci. U. S. A.* **2005,** 102, (29), 10017-10022.

120.   Levanon, H.; Hasharoni, K., *Prog. Reac. Kinet.* **1995,** 20, 309-346.

121.   Hyperchem(TM) Hypercube Inc. 1115 NW 4th Street, G., Florida 32601, USA.

122.   Lide, D. R.; Kehiaian, H. V., CRC Press: Boca Raton, 1994; p x, 518.

123.   Meerholz, K.; Heinze, J., *Electrochim. Acta* **1996,** 41, (11-12), 1839-1854.

124.   Gosztola, D.; Niemczyk, M. P.; Svec, W. A.; Lukas, A. S.; Wasielewski, M. R., *J. Phys. Chem. A* **2000,** 104, (28), 6545-6551.

125.   Parker, V. D., *J. Am. Chem. Soc.* **1976,** 98, (1), 98-103.

126.   Frisch, M. J.; Trucks, G. W.; Schlegel, H. B.; Scuseria, G. E.; Robb, M. A.; Cheeseman, J. R.; Zakrzewski, V. G.; J. A. Montgomery, J.; Stratmann, R. E.; Burant, J. C.; Dapprich, S.; Millam, J. M.; Daniels, A. D.; Kudin, K. N.; Strain, M. C.; Farkas, O.; Tomasi, J.; Barone, V.; Cossi, M.; Cammi, R.; Mennucci, B.; Pomelli, C.; Adamo, C.; Clifford, S.; Ochterski, J.; Petersson, G. A.; Ayala, P. Y.; Cui, Q.; Morokuma, K.; Malick, D. K.; Rabuck, A. D.; Raghavachari, K.; Foresman, J. B.; Cioslowski, J.; Ortiz, J. V.; Baboul, A. G.; Stefanov, B. B.; Liu, G.; Liashenko, A.; Piskorz, P.; Komaromi, I.; Gomperts, R.; Martin, R. L.; Fox, D. J.; Keith, T.; Al-Laham, M. A.; Peng, C. Y.; Nanayakkara, A.; Gonzalez, C.; Challacombe, M.; Gill, P. M. W.; Johnson, B.; Chen, W.; Wong, M. W.; Andres, J. L.; Gonzalez, C.; Head-Gordon, M.; Replogle, E. S.; Pople, J. A. *Gaussian 98*, Revision A.7; Gaussian, Inc.: Pittsburgh, 1998.

127.   Barone, V., World Sci: 1996; Vol. 1.

128.   Langelaar, J.; Rettschnick, R. P. H.; Hoijtink, G. J., *J. Chem. Phys.* **1971,** 54, (1), 1-7.

129.   Wiederrecht, G. P.; Svec, W. A.; Wasielewski, M. R.; Galili, T.; Levanon, H., *J. Am. Chem. Soc.* **2000,** 122, (40), 9715-9722.

130.   Weiss, E. A.; Sinks, L. E.; Lukas, A. S.; Chernick, E. T.; Ratner, M. A.; Wasielewski, M. R., *J. Phys. Chem. B* **2004,** 108, 10309-10316.

131.   Gaines, G. L.; Oneil, M. P.; Svec, W. A.; Niemczyk, M. P.; Wasielewski, M. R., *J. Am. Chem. Soc.* **1991,** 113, (2), 719-721.

132.   Marcus, R. A., *J. Phys. Chem.* **1990,** 94, (12), 4963-4966.

133.   Ratner, M. A., *J. Phys. Chem.* **1990,** 94, (12), 4877-4883.

134.   Mcconnell, H. M., *J. Chem. Phys.* **1961,** 35, (2), 508-515.

135.   Pettersson, K.; Wiberg, J.; Ljungdahl, T.; Martensson, J.; Albinsson, B., *J. Phys. Chem. A* **2006,** 110, (1), 319-326.

136.   Dexter, D. L., *J. Chem. Phys.* **1953,** 21, (5), 836-850.

137.   Closs, G. L.; Johnson, M. D.; Miller, J. R.; Piotrowiak, P., *J. Am. Chem. Soc.* **1989,** 111, (10), 3751-3753.

138.   Andreasson, J.; Kajanus, J.; Martensson, J.; Albinsson, B., *J. Am. Chem. Soc.* **2000,** 122, (40), 9844-9845.

139.   Schlicke, B.; Belser, P.; De Cola, L.; Sabbioni, E.; Balzani, V., *J. Am. Chem. Soc.* **1999,** 121, (17), 4207-4214.

140.   Andreasson, J.; Kyrychenko, A.; Martensson, J.; Albinsson, B., *Photochem. Photobiol. Sci.* **2002,** 1, (2), 111-119.

141.   Indelli, M. T.; Chiorboli, C.; Flamigni, L.; Cola, L. D.; Scandola, F., *Inorg. Chem.* **2007,** 46, (14), 5630-5641.

142.   D'Aleo, A.; Welter, S.; Cecchetto, E.; De Cola, L., *Pure Appl. Chem.* **2005,** 77, (6), 1035-1050.

143.   Akiyama, K.; Kaneko, A.; Tero-Kubota, S.; Ikegami, Y., *J. Am. Chem. Soc.* **1990,** 112, (9), 3297-3301.

144.   El-Sayed, M. A.; Tinti, D. S.; Yee, E. M., *J. Chem. Phys.* **1969,** 51, (12), 5721-5723.

145.   Fujisawa, J.; Ohba, Y.; Yamauchi, S., *Chem. Phys. Lett.* **1998,** 282, (2), 181-186.

146.   Hoshino, S.; Ishii, K.; Kobayashi, N.; Kimura, M.; Shirai, H., *Chem. Phys. Lett.* **2004,** 386, (1-3), 149-152.

147.   Akiyama, K.; Tero-Kubota, S., *Molecular Physics* **1994,** 83, (6), 1091-1097.

148.   Akiyama, K.; Tero-Kubota, S.; Ikoma, T.; Ikegami, Y., *J. Am. Chem. Soc.* **1994,** 116, (12), 5324-5327.

149.   Becke, A. D., *J. Chem. Phys.* **1993,** 98, (2), 1372-1377.

150.   Lee, C. T.; Yang, W. T.; Parr, R. G., *Physical Review B* **1988,** 37, (2), 785-789.

151.   van der Waals, J. H.; ter Maten, G., *Mol. Phys.* **1964,** 8, (4), 301.

152.   Herbich, J.; Kapturkiewicz, A., *Chem. Phys.* **1991,** 158, 143-153.

153.   Kapturkiewicz, A., *Chem. Phys.* **1992,** 166, 259-273.

154.   Mataga, N.; Nishikawa, S.; Asahi, T.; Okada, T., *J. Phys. Chem.* **1990,** 94, 1443.

155.   Nagarajan, V.; Brearley, A. M.; Kang, T. J.; Barbara, P. F., *J. Chem. Phys.* **1987,** 86, (6), 3183-3196.

156.   Okada, T.; Fujita, T.; Kubota, M.; Masaki, S.; Mataga, N.; Ide, R.; Sakata, Y.; Misumi, S., *Chem. Phys. Lett.* **1972,** 14, (5), 563-568.

157.   Okada, T.; Fujita, T.; Mataga, N., *Z. Phys. Chem. N. F.* **1976,** 101, 57-66.

158.   Siemiarczuk, A., *Chem. Phys. Lett.* **1984,** 110, 437.

159.   Siemiarczuk, A.; Ware, W. R., *J. Phys. Chem.* **1987,** 91, (13), 3677-3682.

160.   Siemiarczuk, A.; Grabowski, Z. R.; Krowczynski, A.; Asher, M.; Ottolenghi, M., *Chem. Phys. Lett.* **1977,** 51, 315-320.

161.   Siemiarczuk, A.; Koput, J.; Pohorille, A., *Z. Naturforsch* **1982,** A37, 598.

162.   Tominaga, K.; Walker, G. C.; Jarzeba, W.; Barbara, P. F., *J. Phys. Chem.* **1991,** 95, (25), 10475-10485.

163.   Tominaga, K.; Walker, G. C.; Kang, T. J.; Barbara, P. F.; Fonseca, T., *J. Phys. Chem.* **1991,** 95, (25), 10485-10492.

164.   Menzel, R.; Windsor, M. W., *Chem. Phys. Lett.* **1991,** 184, 6-10.

165.   Okada, T.; Nakatani, K.; Hagihara, M.; Mataga, N., *Ultrafast Phenomena 6* **1988,** 48, 555-558.

166.   Okada, T.; Mataga, N.; Baumann, W.; Siemiarczuk, A., *J. Phys. Chem.* **1987,** 91, (17), 4490-4495.

167.   Herbich, J.; Kapturkiewicz, A., *J. Am. Chem. Soc.* **1998,** 120, (5), 1014-1029.

168.   Grabowski, Z. R.; Rotkiewicz, K.; Siemiarczuk, A.; Cowley, D. J.; Baumann, W., *Nouv. J. Chim.* **1979,** 3, (7), 443-454.

169.   Grabowski, Z. R.; Rotkiewicz, K.; Rettig, W., *Chemical Reviews* **2003,** 103, (10), 3899-4031.

170.   Lee, S.; Arita, K.; Kajimoto, O.; Tamao, K., *J. Phys. Chem. A* **1997,** 101, (29), 5228-5231.

171.   Lee, S.; Kajimoto, O., *J. Phys. Chem. A* **1997,** 101, (29), 5232-5240.

172.   Martin, M. M.; Plaza, P.; Changenet-Barret, P.; Siemiarczuk, A., *J. Phys. Chem. A* **2002,** 106, (10), 2351-2358.

173.   Goldschmidt, C. R.; Potashni, R.; Ottoleng, M., *J. Phys. Chem.* **1971,** 75, (8), 1025-&.

174.   Hirayama, S.; Lampert, R. A.; Phillips, D., *Journal of the Chemical Society-Faraday Transactions Ii* **1985,** 81, (Mar), 371-382.

175.   Lampert, R. A.; Phillips, D., *Journal of the Chemical Society-Faraday Transactions I* **1985,** 81, (Mar), 383-393.

176.   Tanaka, M.; Tanaka, I.; Tai, S.; Hamanoue, K.; Sumitani, M.; Yoshihara, K., *J. Phys. Chem.* **1983,** 87, (5), 813-816.

177.   Nijegorodov, N. I.; Downey, W. S., *Spectrochimica Acta Part a-Molecular and Biomolecular Spectroscopy* **1995,** 51, (13), 2335-2346.

178.   Nijegorodov, N. I.; Downey, W. S., *J. Phys. Chem.* **1994,** 98, (22), 5639-5643.

179.   Hamanoue, K.; Hirayama, S.; Nakayama, T.; Teranishi, H., *Chem. Lett.* **1980**, (4), 407-410.

180.   Wu, K. C.; Ware, W. R., *J. Am. Chem. Soc.* **1979,** 101, (20), 5906-5909.

181.   Lim, E. C.; Laposa, J. D.; Yu, J. M. H., *J. Mol. Spectrosc.* **1966,** 19, (4), 412-&.

182.   Tanaka, F.; Okamoto, M.; Hirayama, S., *J. Phys. Chem.* **1995,** 99, (2), 525-530.

183.   Fukumura, H.; Kikuchi, K.; Koike, K.; Kokubun, H., *Journal of Photochemistry and Photobiology a-Chemistry* **1988,** 42, (2-3), 283-291.

184.   Hirayama, S., *Journal of the Chemical Society-Faraday Transactions I* **1982,** 78, 2411-2421.

185.   Tsubomura, H.; Mulliken, R. S., *J. Am. Chem. Soc.* **1960,** 82, (23), 5966-5974.

186.   Murrell, J. N., *J. Am. Chem. Soc.* **1959,** 81, (19), 5037-5043.

187.   Mulliken, R. S., *J. Am. Chem. Soc.* **1950,** 72, 600-608.

188.   Bixon, M.; Jortner, J.; Verhoeven, J. W., *J. Am. Chem. Soc.* **1994,** 116, (16), 7349-7355.

189.   Krzystek, J., *Organic Magnetic Resonance* **1980,** 13, (2), 151-152.

190.   Hayashi, H.; Iwata, S.; Nagakura, S., *J. Chem. Phys.* **1969,** 50, (2), 993-&.

191.   Hayashi, H.; Nagakura, S.; Iwata, S., *Mol. Phys.* **1967,** 13, (5), 489-&.

192.   Mclauchlan, K. A.; Shkrob, I. A.; Yeung, M. T., *Chem. Phys. Lett.* **1994,** 217, (1-2), 157-162.

193.   Tanaka, F.; Osugi, J., *Chem. Phys. Lett.* **1974,** 27, (1), 133-137.

194.   Hunter, T. F.; Wyatt, R. F., *Chem. Phys. Lett.* **1970,** 6, (3), 221-224.

195.   Kellogg, R. E., *J. Chem. Phys.* **1966,** 44, (1), 411-&.

196.   Bohne, C.; Kennedy, S. R.; Boch, R.; Negri, F.; Orlandi, G.; Siebrand, W.; Scaiano, J. C., *J. Phys. Chem.* **1991,** 95, (25), 10300-10306.

197.   Hamanoue, K.; Hirayama, S.; Nakayama, T.; Teranishi, H., *J. Phys. Chem.* **1980,** 84, (16), 2074-2078.

198.   Antheunis, D. A.; Schmidt, J.; van der Waals, J. H., *Mol. Phys.* **1974,** 27, (6), 1521-1541.

199.   Iwata, S.; Tanaka, J.; Nagakura, S., *J. Chem. Phys.* **1967,** 47, (7), 2203-2209.

200.   Christodouleas, N.; Mcglynn, S. P., *J. Chem. Phys.* **1964,** 40, (1), 166-&.

201.   Webster, D.; Baugher, J. F.; Lim, B. T.; Lim, E. C., *Chem. Phys. Lett.* **1981,** 77, (2), 294-298.

202.   Chandra, A. K.; Lim, E. C., *Chem. Phys. Lett.* **1977,** 45, (1), 79-83.

203.   van der Auweraer, M.; Grabowski, Z. R.; Rettig, W., *J. Phys. Chem.* **1991,** 95, (5), 2083-2092.

204.   El-Sayed, M. A., Excited States. In Lim, E. C., Ed. Academic Press: New York, 1974; Vol. 1, pp 35-77.

205.   MATLAB *MATLAB*, The MathWorks, Inc.: Natick, MA, 2006.

206.   Kottis, P.; Lefebvre, R., *J. Chem. Phys.* **1963,** 39, 393-403.

207.   Pshenichnikov, M. S.; de Boerij, W. P.; Wiersma, D. A., *Opt. Lett.* **1994,** 19, 572-575.

208.   Frisch, M. J.; Trucks, G. W.; Schlegel, H. B.; G. E. Scuseria; Robb, M. A.; Cheeseman, J. R.; Zakrzewski, V. G.; J. A. Montgomery, J.; Burant, R. E. S. C.; Dapprich, S.; Millam, J. M.; Daniels, A. D.; Kudin, K. N.; Strain, M. C.; Farkas, O.; Tomasi, J.; Barone, V.; Cossi, M.; Cammi, R.; Mennucci, B.; Pomelli, C.; Adamo, C.; Clifford, S.; Ochterski, J.; Petersson, G. A.;

Ayala, P. Y.; Cui, Q.; Morokuma, K.; Rega, N.; Salvador, P.; Dannenberg, J. J.; Malick, D. K.; Rabuck, A. D.; Raghavachari, K.; Foresman, J. B.; Cioslowski, J.; Ortiz, J. V.; Baboul, A. G.; Stefanov, B. B.; Liu, G.; Liashenko, A.; Piskorz, P.; Komaromi, I.; Gomperts, R.; Martin, R. L.; Fox, D. J.; Keith, T.; Al-Laham, M. A.; Peng, C. Y.; Nanayakkara, A.; Challacombe, M.; Gill, P. M. W.; Johnson, B.; Chen, W.; Wong, M. W.; Andres, J. L.; Gonzalez, C.; Head-Gordon, M.; Replogle, E. S.; Pople, J. A. *Gaussian 98*, Gaussian, Inc., Pittsburgh, PA, 2001.

209.   Lukas, A. S.; Miller, S. E.; Wasielewski, M. R., *Journal of Physical Chemistry B* **2000,** 104, 931-940.

210.   Greenfield, S. R.; Wasielewski, M. R., *Opt. Lett.* **1995,** 20, 1394-1396.

Appendix A

Transient Continuous Wave EPR Instrument Control and Data

Acquisition:

LabVIEW Program Documentation

A-1 Introduction

This appendix outlines the most recent version (TCWn17) of software designed for instrument control and data acquisition using a Bruker ESP300e system interfaced with a windows OS computer operating LabVIEW hardware and software. The aim of this appendix is not to outline every single detail of the software. Instead, it will describe the basic steps involved with using the program and inform future users of the overall program design and principles that are employed in this application. This will enable the user to have (1) a practical understanding of how to collect data, (2) a functional understanding what is happening when data is being collected, and (3) how to appropriately resolve bugs that may arise in the future as well as make modifications to the code in the event of hardware changes.

The goal of **Section A-2.1** is to describe the steps a user must follow in order to collect a TREPR dataset using this software and to explain what happens "behind the scenes" as those steps are taken, **Section A-2.2**. As an example, it will walk through data collection of a radical pair (RP) signal at room temperature. The software is designed so that the "user experience" is very similar to that of the Bruker XEPR software. Specifically, the organization and the capabilities of the individual panels described in **Section A-4** are intended to make it easy for the user to switch between the two EPR systems (ESP300e vs. ESP580) without having to learn an entirely new software package.

A-2 Program Use

As stated in the introduction (**Section A-1**), this software is designed so that a user can switch between the two EPR systems (ESP300e & ESP580) without having to learn an entirely

new software program. The goal of this section is to describe the steps a user must follow in order to collect a TREPR dataset using this software.

As an example, in **Section A-2.1** we will walk through data collection of a radical pair (RP) signal at room temperature. MeOAn-ANI-s-NI (JACS – vol. 118 pp. 6767), commonly called "the Greenfield molecule" is an ideal system for a new user to start with because it has a large spin-polarized signal and has long-term photostability (years).

Section A-2.2 will then repeat the steps in **Section A-2.1** followed by a description of what is actually happening in the code.

A-2.1 Detailed Walk-Through

First, make sure that all of the hardware is on (ESP300e console, magnet, power supply, heat exchange, chilled water, computer, etc.). To perform an experiment, open the TCWn17 VI (there should be a shortcut on the desktop). To start execution of the TCWn17 press "play" (located in the upper left). There are two groups of parameters which must be set in order to collect a TCW dataset. Finding the EPR signal and determining these parameters require iteration between the "*acquisition parameters*" and "*scope parameters*" VIs.

Open the *acquisition parameters* panel by pressing the "Acquisition Parameters" button in the "Exp. Parameters" section of TCWn17, Figure A-4. In this VI, you specify the center field value, sweep width, and the number of points, which will be used during the acquisition. In general, you can get a very good "first guess" of where center field is by using the operating frequency (υ) value indicated on the ESP300e console computer and multiplying by ($h/(g \cdot \beta)$) with the assumption that $g \approx 2.0023$. An even simpler trick to use when $g \approx 2.0023$ is just to

multiply υ by 3400 / 9.5 (where ~3400 is the center field value for free radicals at an operating frequency of ~9.5 GHz).

At this point, open the *scope parameters* panel by pressing the "Scope Parameters" button, Figure A-4. This opens the digital oscilloscope panel where many of the default values should be reasonable for a scan, however make sure the signal channel and trigger source values are correct. The most likely value that will need to be changed is the "Vertical Range (V)". This is equivalent to changing the scale of the y-axis. This value will depend on sample concentration, laser power, microwave power, tuning, etc, however usually a "Vertical Range" value of 0.4 or 1 is a good starting point. Other values that will frequently be adjusted include the "number of records" (i.e., averages), the "record length" (# of points in the scan), and the "time base" (# of nanosecs. between points).

Now the user needs to iterate between the two VIs. Switch back to the *acquisition parameters* VI and start changing the current value until you see a signal in the *scope parameters* display. Once you see a signal, adjust the record length, and the number of averages to the desired value and press the "close" button on the *scope parameters* VI. Next, set the *acquisition parameters* values (center field, sweep width, number of points) to appropriate values, press "Load Params", and press the "close" button.

Finally, press "Run Exp." on the TCWn17 panel. The values that were set in the *acquisition parameters* and *scope parameters* VIs will be used for the data acquisition. Take note, you must manually close both the *acquisition parameters* and *scope parameters* VIs before TCWn17 will allow you to run the actual experiment. As data is acquired, the display on the TCWn17 panel will be dynamically updated with the new data.

When the scan is finished, the user has three options. The user can Save, Store, or Remove the dataset from memory. (Note: the most recent acquisition is always stored in the "Current/Most Recent Exp." selection from the drop down box on the front panel. This dataset cannot be removed). Storing a dataset stores it in memory but does not write it to disk. This is especially useful during the first exploratory acquisitions of a new system while the user is determining the best parameters to use for the final acquisition. After the dataset is collected, the user should optimize the *acquisition parameters* and *scope parameters* as outlined above.

When an adequate dataset is collected, press "save", and the data is saved in the Bruker BES3T® format so that post-collection analysis can be performed using the XEPR software.

A-2.2 A "Detailed Walk-Through" Explained

In this section, all the text that appears in black is identical to the previous section. *All text that appears in italics is a high level description of what happens in the code when the user performs some sort of action. For further details, the user is referred to the corresponding sections and figures. Additionally, LabVIEW can help the user follow along as the code is executed by using the "Highlight Execution" option on the block diagram. To enable this, open the block diagram, and press the little lightbulb icon in the upper left. Then proceed to use the program normally. As the code executes, the block diagram will animate how and where the data is moving. The caveat is that it is much more difficult to track what is happening in subVIs if the mainVI is highlighting execution. Occasionally there are synchronization issues when the mainVI is operating at the reduced speed necessary to show the animations, and the subVIs are not. This is unfortunate, but necessary for multi-VI applications.*

First, make sure that all of the hardware is on (ESP300e console, magnet, power supply, heat exchange, chilled water, computer, etc.). To perform an experiment, open the TCWn17 VI (there should be a shortcut on the desktop). To start execution of the TCWn17 press "play" (located in the upper left). *TCWn17 is initialized. All the default values are set in the "CTRL INIT." and "SHIFT INIT." VIs. The master queue which is responsible for passing all information back and forth between the main VI and sub VIs is created at this point. The event structure in the primary while loop waits in the "Timeout" event for user input.* There are two groups of parameters which must be set in order to collect a TCW dataset. Finding the EPR signal and determining these parameters require iteration between the "*acquisition parameters*" and "*scope parameters*" VIs.

Open the *acquisition parameters* panel by pressing the "Acquisition Parameters" button in the upper left, Figure A-4. *(note: See **Section A-4.3** for important concepts.) In TCWn17, the value of 'subVI cluster' changes in the "Timeout" event, Figure A-5, which signals the "run subVI #" event to fire. "run subVI #", Figure A-7, checks to see if the subVI is already open, if it is, nothing happens, if it is not, the subVI is opened, and a 'control reference' for the subVI is added to the "subVI ref array" wire. The "subVI ref array" wire maintains a running status of all subVIs which have been opened by TCWn17 (i.e., When a subVI is closed TCWn17 externally closes it and the corresponding control reference is removed from the "cntrl ref array", **Section A-4.3.1**, Figure A-6. In this VI, you specify the center field value, sweep width, and the number of points, which will be used during the acquisition. (note: See **Section A-4.4** for details and concepts) AcqPrm21n04 is a relatively simple VI. It uses numerical values that are set by the user, basic math operations, and arrays to pass values to the "ER032M" Instrument I/O Assistant. "ER032M" is responsible for communicating via GPIB commands with the ESP300e*

console, i.e., setting the field values. In general, you can get a good "first guess" of where

center field is by using the operating frequency (υ) value indicated on the ESP300e console

computer and multiplying by (h/(g•β)) with the assumption that g ≈ 2.0023. An even simpler

trick to use when g ≈ 2.0023 is just to multiply υ by 3400 / 9.5 (where ~3400 is the center field

value for free radicals at an operating frequency of ~9.5 GHz).

At this point, open the *scope parameters* panel by pressing the "Scope Parameters"

button, Figure A-4*. (note: See **Section A-4.5** for details and concepts) The Scope subVI is

opened in the exact same manner as the Acquisition Parameters subVI outlined above.* This

opens the digital oscilloscope panel where many of the default values should be reasonable for a

scan, however make sure the signal channel and trigger source values are correct. The most

likely value that will need to be changed is the "Vertical Range (V)". This is equivalent to

changing the scale of the y-axis. This value will depend on sample concentration, laser power,

microwave power, tuning, etc, however usually a "Vertical Range" value of 0.4 or 1 is a good

starting point. Other values that will frequently be adjusted include the "number of records"

(i.e., averages), the "record length" (# of points in the scan), and the "time base" (# of nanosecs.

between points).

Now the user needs to iterate between the two VIs. Switch back to the *acquisition*

parameters VI and start changing the current value until you see a signal in the *scope parameters*

display. Once you see a signal, adjust the record length, and the number of averages to the

desired value and press the "close" button on the *scope parameters* VI. Next, set the *acquisition*

parameters values (center field, sweep width, number of points) to appropriate values, press

"Load Params", and press the "close" button. *(note: The following explanation outlines how*

*TCWn17 receives and processes data which is its 2nd primary capability, **Section A-4.3,** Figure*

A-3.) When the "Load Params" button is pressed, the "sweep array", Figure A-19, is

created. The 'Sweep Array' variable defines the field points that will be used when performing

the TCW experiment. At this point, "zexdVI Event Monitor_04" (which is running in parallel

with AcqPrms21n04 – see the block diagram, Figure A-19) takes the "sweep array" variable

and enqueues it into the master queue. TCWn17 detects that the master queue has an item in it

and dequeues the item. When the item is dequeued, the "Cluster In" event is fired (Figure A-7,

Figure A-8, Figure A-9), and the variable is put into the proper wire and stored using the shift

registers until it is needed later. In this way (using the queue to pass data, and wires/shift

*registers to store data, see **Section A-4.3.2** for details), TCWn17, maintains values for the*

Acquisition Parameters and Scope Parameters which will then be used to collect the data.

Finally, press "Run Exp." on the TCWn17 panel. *(note: See Section A-4.3.1 for an*

outline of what happens when "Run Exp" is pressed, Figure A-13, Figure A-14.) Once all the

proper variables are set in the Acquisition Parameters and Scope Parameters VIs, the DAQ VI

*(daq13n01.vi) is run (**Section A-4.6**). The data that is collected is passed back to TCWn17 via*

the master queue, but this VI is hidden from the user because there is no need to interact with it

as it is entirely automatic. Also, the Acquisition Parameters and Scope Parameters VIs are

disabled so that the user cannot accidentally send conflicting commands to the hardware as the

TCW scan proceeds. The values that were set in the *acquisition parameters* and *scope*

parameters VIs will be used for the data acquisition. Take note, you must manually close both

the *acquisition parameters* and *scope parameters* VIs before TCWn17 will allow you to run the

actual experiment. As data is acquired, the display on the TCWn17 panel will be dynamically

updated with the new data. *As the DAQ VI runs, it passes each kinetic trace back via the master*

queue to TCWn17 until it finishes. As individual kinetic traces are dequeued by TCWn17, they

are assembled into the 2D dataset. This is done in a similar way to how the "Sweep Array"

*variable is processed (read **Section A-4.3.2**, Figure A-7, Figure A-8, Figure A-9). Which means*

that when it is dequeued, it is sorted according to type of data that it is and processed

accordingly. In the case of a kinetic trace (Figure A-8), it is added into the 2D dataset (as

compared to if it is the "Sweep Array", where it is put into a wire/shift register). When the DAQ

VI has finished collecting data, it passes back all of the parameters that were used in the data

*collection in a variable called "Final Data Package", **Section A-4.6.3**, Figure A-30 where the*

completed 2D dataset and its corresponding parameters are temporarily stored in the

"Current/Most Recent Exp." until the user saves/stores/removes, or collects a new scan.

If the "Track Progress" option is checked on the front panel of TCWn17, each time a

kinetic is returned from the DAQ VI, several GUI commands are run sequentially. First, the

"datasets" event is fired which changes the front panel of TCWn17 to display the current

dataset, Figure A-14. It does this by putting the full 2D dataset (or as much of it that currently

has been collected) into a wire called "data package template". When the dataset has been

loaded, the "projection" event is fired, Figure A-15. This checks the value of the projection

button on the front panel and changes the graph properties to show kinetic or spectral

information (x-axis, y-axis values, etc.). At the end of the "projection" event, the "slide" event

is fired. The "slide" event checks to see what value the slider on the graph is at, and then selects

and plots the corresponding spectral or kinetic data based on the value of the projection button

on the front panel.

When the scan is finished, the user has three options. The user can Save, Store, or

Remove the dataset from memory. (Note: the most recent acquisition is always stored in the

"Current/Most Recent Exp." selection from the drop down box on the front panel. This dataset

cannot be removed). Storing a dataset stores it in memory but does not write it to disk. This is especially useful during the first exploratory acquisitions of a new system while the user is determining the best parameters to use for the final acquisition. After the dataset is collected, the user should optimize the *acquisition parameters* and *scope parameters* as outlined above.

When an adequate dataset is collected, press "save", and the data is saved in the Bruker BES3T® format so that post-collection analysis can be performed using the XEPR software. *The Save, Store, and Remove commands are all controlled using the "command" event in TCWn17 (**Section A-4.3.2**, Figure A-10, Figure A-11, Figure A-12). The way the command is fired is very similar to how a subVI is opened. As TCWn17 waits for user input, the "timeout" event is run repeatedly, when a command button is pressed, the "rmt cntrl clstr" cluster value changes and the "command" event is triggered (similar to firing the "run SubVI#" event as has been described above). When the "command" event fires, the appropriate actions are performed based on which button was pressed. For example, when "save" is pressed, the "save" case is executed and the data is stored in the proper file formats (see the "save_file_dialog_08.vi" for details on how the data is saved).*

A-3 Program Conventions

This section covers the conventions used in naming VIs, icon design, and for generating figures used in **Section A-4**. This information is critical if the reader intends to alter the code in any way. However, this section may be skipped if the reader is only concerned with understanding how to use the program.

A-3.1 Naming Conventions

In order to maintain the long-term stability of the code, it is essential that ***any*** changes made are documented immediately. Here I will describe the naming scheme that is used for all VIs using 'TCWn17' as an example. The current version of the main VI is TCWn17. It is preceded by TCW1-47 and TCWn1-16. At TCW47 there was a major overhaul in which queuing was implemented as a means for passing data between subVIs and the main VI. At this point, TCWn1 was created. Each significant change is saved as a *new* version of TCWn*XX*. The reason for this is straightforward; In the event that a change to the code has unanticipated results, the previous *working* version of the software is still available and can be used as a recovery point. This convention is followed for *all* VIs which I have written.

When TCWn1 was created, the current working versions of the other three principal VIs were also relabeled as "*PreviousNameYYnXX*".

A-3.2 Icon Conventions

This Appendix focuses on the most important VIs that are necessary for explaining program design and data-flow, however, there are *many* subVIs that I also wrote which aid in the tasks of the primary VIs. Most of the home-written subVIs can be identified by their icon (which is shown in the upper right corner of the VI). In general, I have tried to include my initials "ZEXD" in the icons of all of the VIs which I coded. A representative example is shown in Figure A-1.

Figure A-1. "zexdVI Event Monitor_XX" Icon.

A-3.3 Figure Conventions

The figures in the **Section A-4** of this appendix were created from default documentation output capabilities provided by LabVIEW. This permits future users to generate similar documentation for any changes or additions to the code from its present state. These figures show all possible case and event structures in nested order. The final figure of each section shows all of the subVIs which are hard-coded into the block diagram. This encompasses the majority of subVIs used by a given VI, however it does not include soft-coded subVIs. This is particularly important for TCWn17 because the most important subVIs that it calls are soft-coded into an array on the front panel called 'subVI path array'. This will be discussed in greater detail later. Finally, there a yellow text boxes with black writing scattered throughout the code which contain information specific to the section in which they are found. Some instances have a comment about the function of that part of the code. At other times, they indicate desirable upgrades and/or potential bugs.

A-4 Program Design

A-4.1 General Information

It is important to briefly comment on the quality of the LabVIEW user community and default help documentation that is included with the software. Throughout the development of this code, those resources provided a constant source of feedback regarding program design decisions. If you are going to alter this code in any way, it is critical that you know (1) what you are changing, (2) why you need to change it, (3) how those changes should be incorporated into overall program design, and (4) what the ramifications of the changes will be on overall program design. These questions must be addressed before the code is altered, and the LabVIEW resources are invaluable in addressing them.

A-4.2 Introduction

At present there are four primary VIs which are responsible for the principal tasks of instrument control and data acquisition, Figure A-2. They are outlined loosely below, however not all capabilities of each VI are described.

1. Transient Continuous Wave VI (TCWn17) – This is the 'main' VI. It is responsible for controlling the behavior of the subVIs relative to one another, assembling and displaying the results of an acquisition, and saving the data.

2. Acquisition Parameters VI (AcqPrm21n04) – This VI controls the ESP300e system. It is responsible for selecting field values and step sizes which will define the sweep parameters during real-time visualization and during the data acquisition scan.

3. Scope Parameters VI - (niScope EX Configured Acquisition_new_12n02) – This VI is responsible for controlling and setting the NI-scope parameters which will be used during real-time visualization and during the data acquisition scan.

4. Data Acquisition VI – (daq13n01) – This VI uses the parameters set by the Acquisition Parameters VI and the Scope Parameters VI to collect individual kinetic records which are then passed back to the Transient Continuous Wave VI for assembly into a 2D dataset.

TCWn17 is the 'main' VI. It is responsible for controlling the behavior of the subVIs relative to one another. Loosely speaking, the red lines correspond with instrument control while the blue lines correspond with data acquisition. These two channels cannot be run simultaneously since they both use the same hardware resources. Information is passed back to the main VI using a unique, pseudo-randomly named queue that is created during program initialization. The name of this queue is passed to each subVI during it's initialization. In this way, multiple events can be stored in the queue without losing information while the main VI dequeues items sequentially and handles them accordingly. Importantly, *global variables are never used in this program, nor do they need to be.* Using global variables can lead to untraceable problems resulting from race conditions and synchronization issues. Instead, shift registers (which are extremely fast and memory efficient) are used extensively in this code in order to pass data from event to event. Additionally, when necessary, property nodes are used to access information that is only used infrequently where speed is less important. Lastly, "error handling" is used wherever possible (which is almost everywhere). By using error handling properly, it is easier to track bugs as well as direct program flow. The reader is directed towards the LabVIEW user forums and help documentation for extensive explanations regarding these

topics. The following sections will describe in further detail information that is specific to a
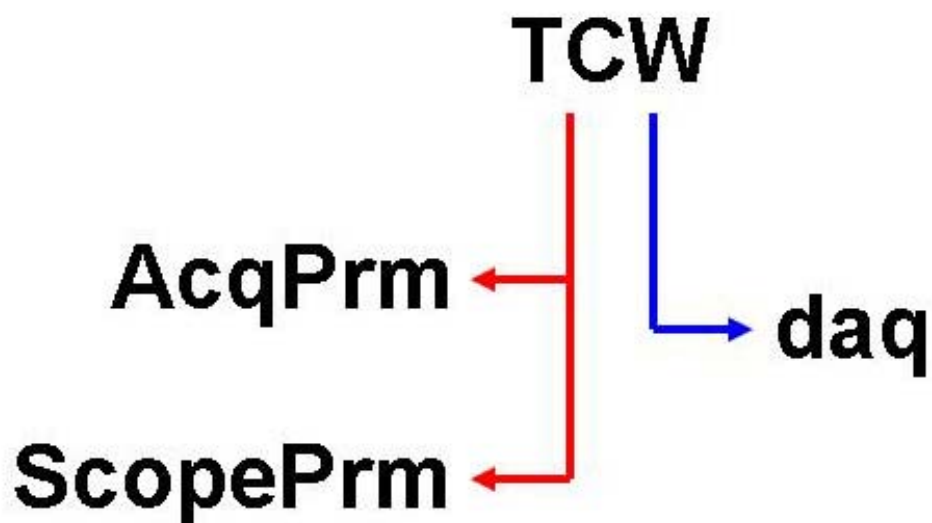
given VI.

Figure A-2. This diagram describes the interaction between the four primary VIs. The red lines correspond with instrument control while the blue lines correspond with data acquisition. These two channels cannot be run simultaneously.

A-4.3 Transient Continuous Wave VI - (TCWn17)

This is by far the most complicated individual VI, although the reason for this is somewhat counterintuitive. TCWn17 offloads most of the work to subVIs, however, the graphical user interface (GUI) requires a tremendous amount of code in order to look and function in an appealing manner, Figure A-4. The three primary tasks of TCWn17 are:

1. call subVIs as described in the previous section

2. receive data from the Data Acquisition VI, assemble it into a 2D data structure and store, save, or remove it

3. maintain a responsive GUI that allows the user to interact with the software/hardware in an intuitive fashion, Figure A-3.

As is expected, there is a moderate amount of overlap between these three tasks, however, for the sake of clarity, the following sections will attempt to explain these tasks as separately as possible.
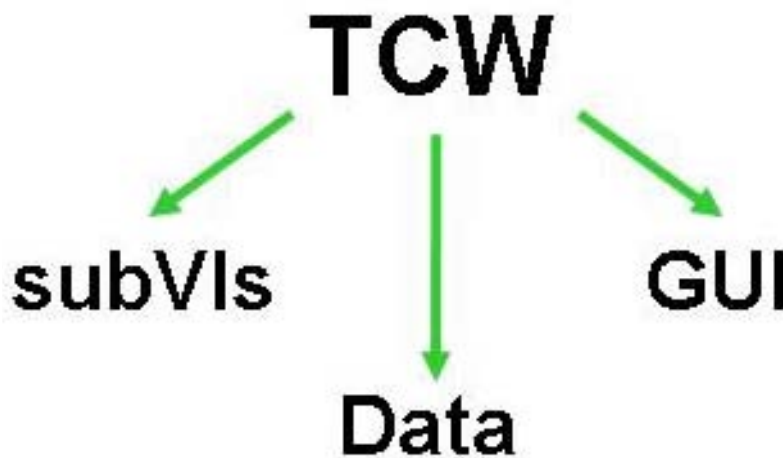
Figure A-3. This diagram shows the three primary tasks of TCWn17 which are outlined in the following sections.

TCWn17 contains two independent while loops and behaves in a variation on the producer/consumer design architecture (http://zone.ni.com/devzone/cda/tut/p/id/3023), Figure A-5. The primary while loop uses an 'event structure' to perform essentially every task. According to the LabVIEW documentation, an event structure "...*has one or more subdiagrams, or event cases, exactly one of which executes when the structure executes. The event structure waits until an event happens, then executes the appropriate case to handle that event*". An event can be anything which is defined by the event structure. For example, when a user presses a button on the GUI, or when a subVI returns information, the event structure responds accordingly. Events can also be fired programmatically using what is called a (Signaling) property node. In general, individual events require only a small bit of relatively simple code. One of the primary benefits of the event structure is that by properly sequencing multiple single events (i.e. – programmatically), a very rich variety of results can be achieved. Figure A-5 through Figure A-16 show every section of the event structure.

The secondary while loop, labeled the "queue retrieval loop" serves a single purpose. It waits until something is enqueued by a subVI and then dequeues it and sends it to the primary loop for processing. When the secondary loop dequeues the "terminate TCW" signal, the secondary while loop is terminated and the queue is released. This can only happen if the user has pressed the "close TCW" button on the front panel.

The 'timeout' event, Figure A-5, is responsible for monitoring user input via the buttons on the front panel. Each button on the front panel is put into one of two clusters ('rmt cntrl clstr' or 'subVI cluster'). When that button is pressed, the state of the cluster changes, and the

corresponding event is fired. This is not an the most simple way of doing this, however it allows the code to be very flexible as will be covered during the explanation of Figure A-7. in the next section.

A-4.3.1 Flexible Modular SubVI Control

Figure A-6 and Figure A-7 contain the events which are responsible for the powerful and flexible subVI control capabilities of TCWn17. This code is designed in order to allow for the addition of more modules besides the ones presently available. For example, this could include ENDOR capabilities in the future. These parts of the code can be thought of as similar to "plugins", and there are LabVIEW examples available which can be used to clarify this concept if the reader desires. In order for TCWn17 to have this flexibility and *at the same time* maintain control over all of the subVIs it has launched, an internal list (array) is maintained which contains LabVIEW references to each subVI that is currently under it's control. Using "TCW ZEXD – CREATE REFS", this running list is updated every time a new subVI is opened or closed to reflect the change, Figure A-6.

In brief, if the user wants to add a new subVI, he/she must

1. add the path to the new subVI to the 'subVI path array' found on the front panel, Figure A-4. This is called a 'soft-coded' subVI because only the *path* of the VI is coded and whatever that path points to is what is actually opened. If one wanted to alter the code in a soft-coded subVI , there would be no need to update the main VI because the subVI is compiled at runtime.

2. add the button to access the subVI to the 'subVI cluster' discussed above.

3. If the subVI requires initialization parameters, these can be handled on an individual case using the "TCW ZEXD – SUBVI OPEN" subVI contained in the "run subVI#" event.

4. take note – this means that the order of the controls in the 'subVI cluster' MUST match the order of the subVIs included in the 'subVI path array'

Finally, when the Data Acquisition VI is started or stopped (prematurely), the "Run Exp, Stop Exp" event is fired, Figure A-13. This is a special event because this subVI requires that all other subVIs are closed prior to and during execution. The "Run Exp" case also needs to create an empty 2D array that will be populated with the kinetic waveforms, reinitialize the slider and current data plot, and disable the other subVIs from running. When the Data Acquisition VI needs to be stopped prematurely, the "Stop Exp" case properly closes the subVI so that the scope is left in a known state, Figure A-14.

A-4.3.2 Data Processing

When objects are enqueued by subVIs (or even TCWn17 itself), they must be dequeued and processed by TCWn17. This occurs in the "Cluster In: Value Change" event (lower part of Figure A-7). When a queue is created, it can only contain a single type of data. In order to make a single queue work for all the different types of data that are created by the subVIs, the structure of the data is a cluster which contains (1) an identifier string, and (2) a VARIANT datatype (which can then be converted back to the proper datatype).

The "terminate" case is used any time that a subVI closes. The "Array 1DDBL" and "Scope Cluster" cases handle the Sweep Array defined by the Acquisition Parameters VI and the Scope parameters defined by Scope Parameters VI. The "Measure Data (waveform)" case

collects the incoming kinetic waveform acquired in the Data Acquisition VI and inserts it into the 2D data matrix. This case also handles the "Track Progress" option displayed on the front panel. Lastly, the "Final Data Package" case is executed when the Data Acquisition VI completes and enqueues all of the information that is relevant to the scan that just completed, such as record length, time base, etc.

In a similar fashion to the "plugin" approach of calling subVIs, TCWn17 allows the user to add multiple controls to the front panel which are all handled in a single multi-case structure contained in the "command" event, Figure A-10 through Figure A-12. The "command" event contains a multi-case structure which allows user commands to be executed according to the LABEL value of the control.

In brief, if the user wants to add a new control, he/she must

1. add the control button to the 'rmt cntrl clstr' found on the front panel, Figure A-4. The cluster is made invisible in order to make the GUI attractive, however it can be still accessed.

2. It is IMPERATIVE that the control LABEL has a unique name that is different from all other controls in the cluster

3. In order to add code that is specific to the new control, the user needs to go to the "command" event, and create a new case that labeled identically to the LABEL for the control. Figure A-10 through Figure A-12 show examples of how this is already done for storing, saving, and removing data.

As an example, consider the "save" case in the "command" event. This case calls the "SUBVI ZEXD – SAVE FILE" subVI. This subVI then saves the acquired data in the proper formats for data work-up in Bruker's Xepr software.

Finally, the <remote control cmd> event, Figure A-12, is a very powerful event which allows the user to control (via "SUBVI ZEXD – REMOTE CONTRL") *any* values of *any* remote VI that are passed to it using "control references". See the "close.ext" case to see how it is properly invoked. I believe that this event is probably on the edge of what would be considered "good" programming practice because it uses "control references" and the VI server to communicate between subVIs instead of through more conventional channels such as queues. This does leave the door open for a user to abuse this capability and change controls externally without knowing what the current state of the subVI that is being affectedis in. However, the only way that it is used presently is to externally close subVIs in such a way so that they are shut down properly (i.e. – leaving the scope in a known state).

A-4.3.3 Graphical User Interface

Figure A-14 and Figure A-15 show the remaining events which are responsible for updating the GUI according to user events (such as the slider or projection button). The "datasets" event, Figure A-14, is called when a user selects a specific dataset (that has be stored , saved , or just collected). It selects the correct dataset from the shift register running along the bottom of the event. That shift register contains an array of datasets, each of which has been added immediately after data acquisition occurs. Before finishing, this event programmatically fires the "projection" event to directly follow it so that the waveform graph on the front panel is updated with the new dataset using the current projection.

The "projection" event changes the current projection of the dataset in the waveform graph window, i.e. spectrum or kinetic. Finally, the "slide" event selects the appropriate waveform from the 2D dataset and plots either spectral or kinetic based on the value of the 'projection' control.
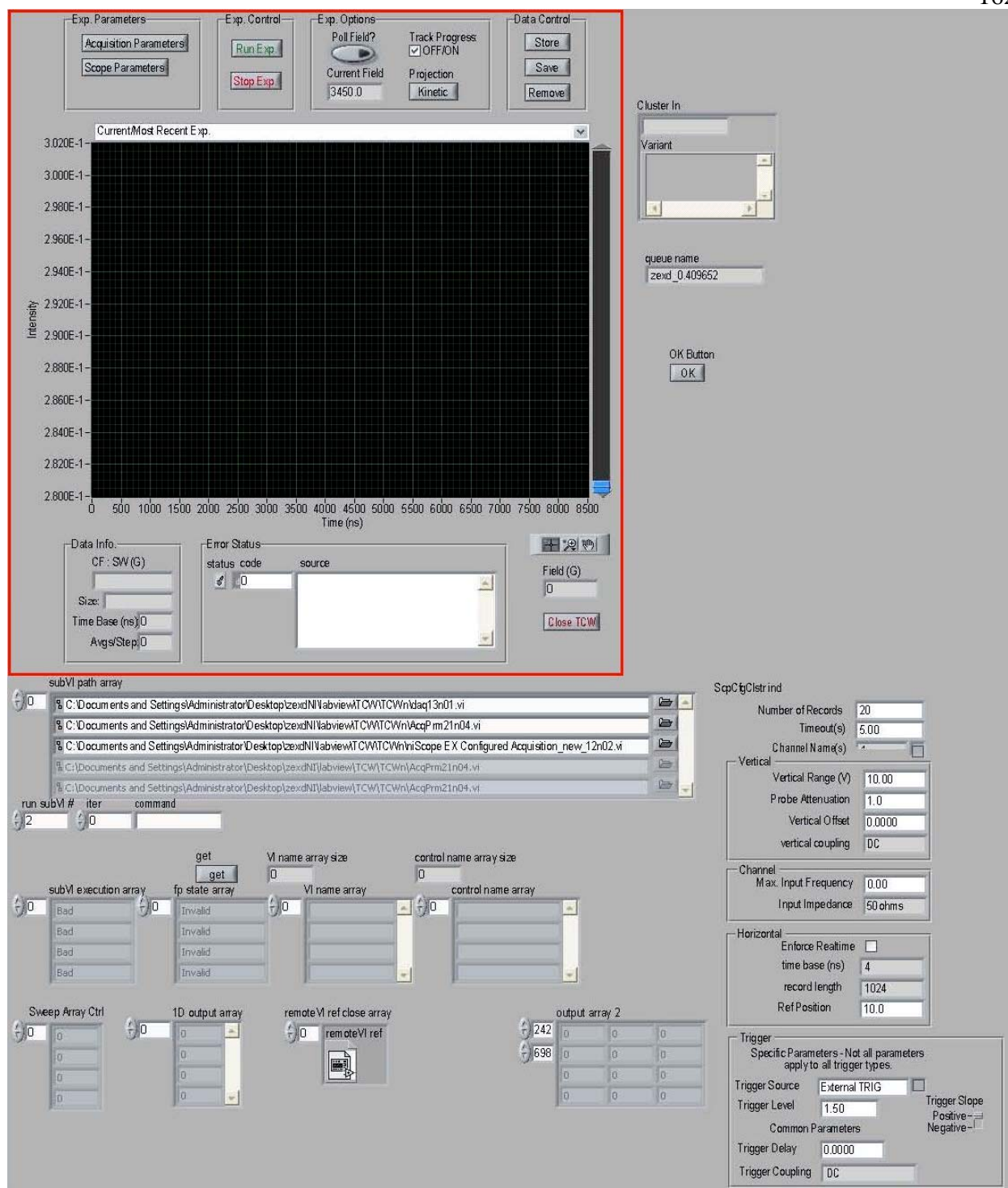
Figure A-4. Front Panel of TCWn17. The section enclosed by red in the upper left quadrant is what is actually viewable during execution. 'subVI path array' contains the paths of all other subVIs that can be called from within TCWn17. The remainder of the controls are aptly named.
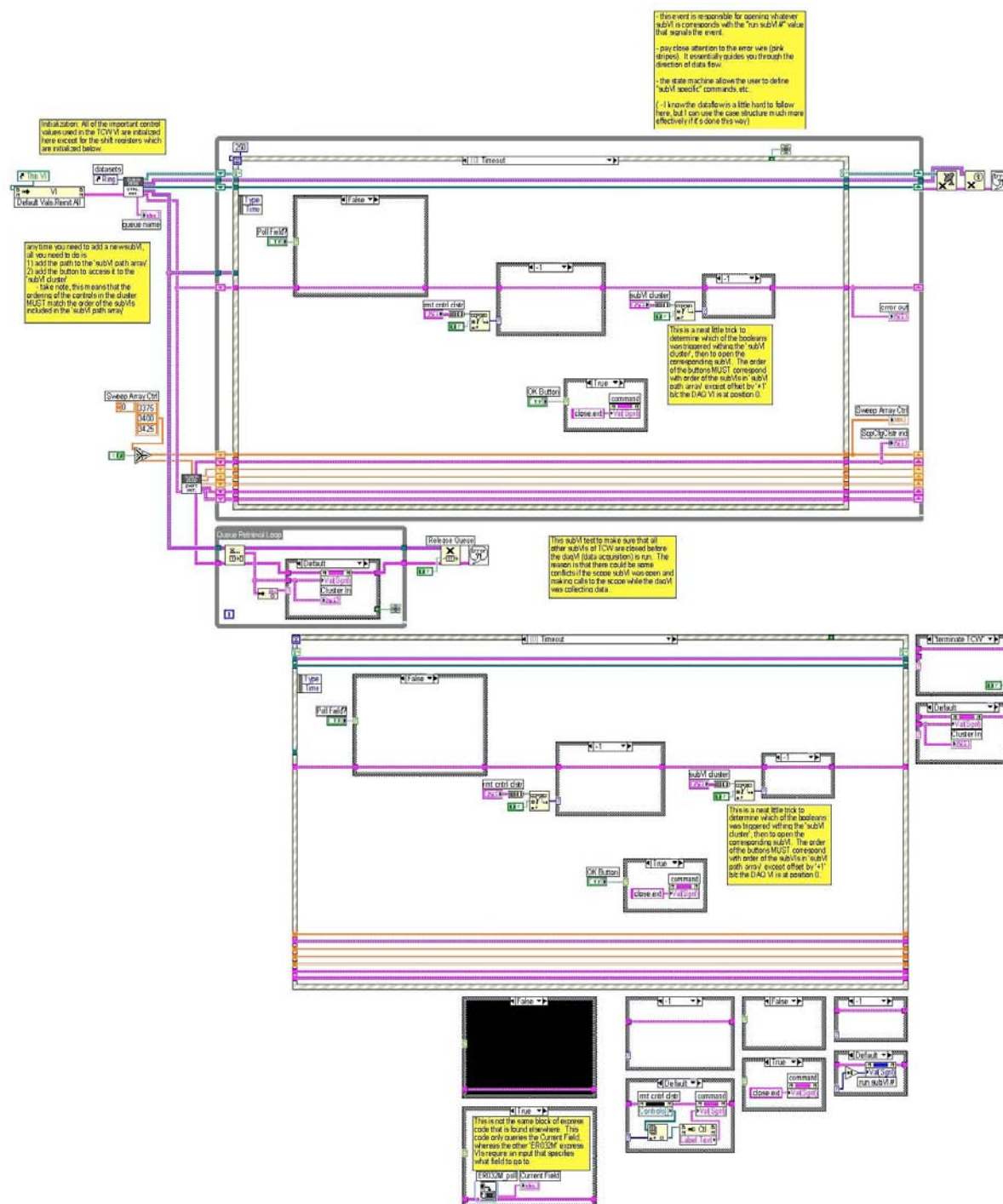
Figure A-5. The upper portion of the Block Diagram section displays the two primary while loops of TCWn17. The event structure is contained in the top while loop and the lower while loop is the "Queue Retrieval Loop".
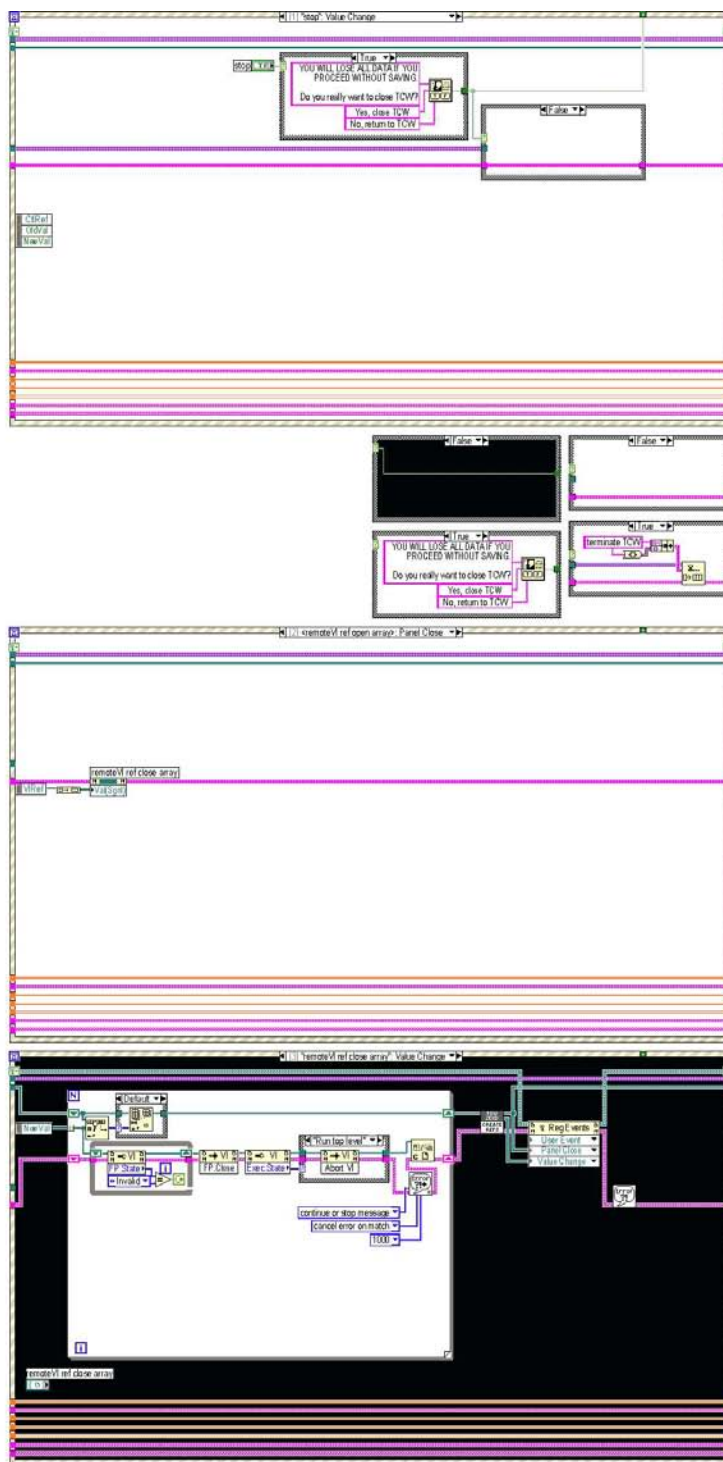
Figure A-6. <remoteVI ref open array>: Panel Close and "removeVI ref close array" are used to maintain a running list of all open subVIs that have been called from TCWn17.
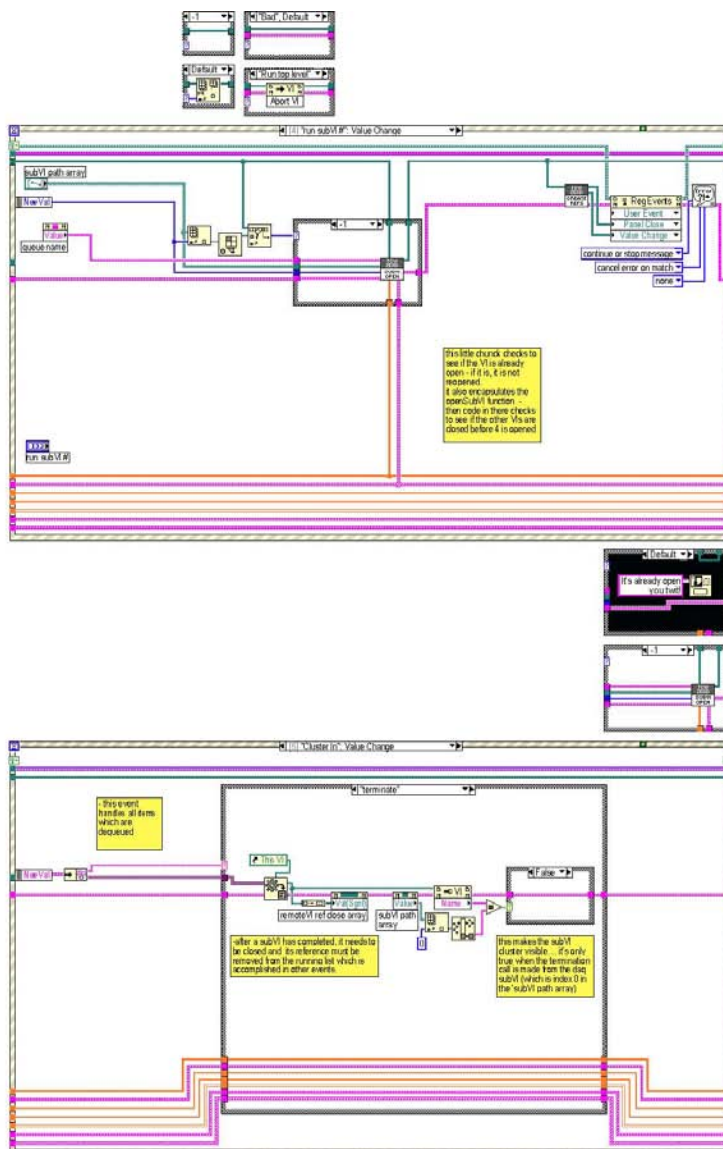
Figure A-7. Upper portion is "run subVI #" event which opens subVIs when fired. Lower portion is the "Cluster In" event which is responsible for processing all items that are dequeued.

166

Figure A-8. These are additional cases available within the "Cluster In" event which is responsible for processing all items that are dequeued. The "Array 1DDBL" and "Scope Cluster" cases handle the Sweep Array defined by the Acquisition Parameters VI and the Scope parameters defined by Scope Parameters VI. The "Measure Data (waveform)" case collects the incoming kinetic waveform collect in the Data Acquisition VI and inserts it into the 2D data matrix. This case also handles the "Track Progress" option displayed on the front panel.

167
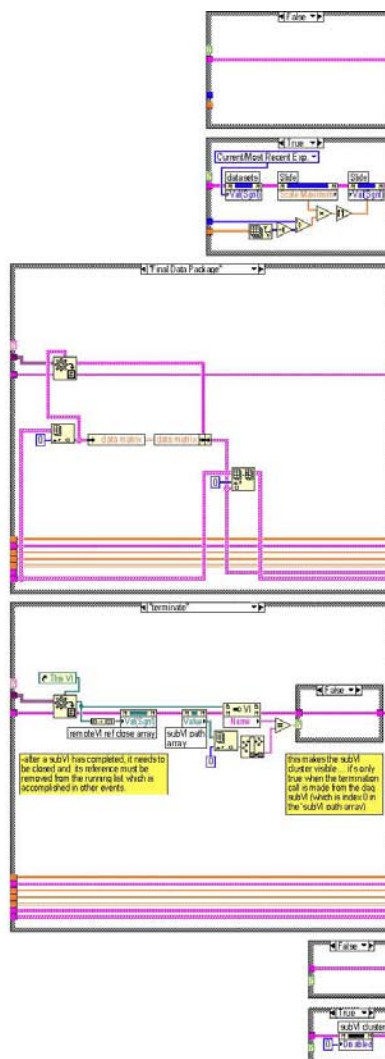
Figure A-9. The "Final Data Package" case is executed when the Data Acquisition VI completes and enqueues all of the information that is relevant to the scan that just completed, such as record length, time base, etc. The "terminate" case (lower) is used any time that a subVI closes.
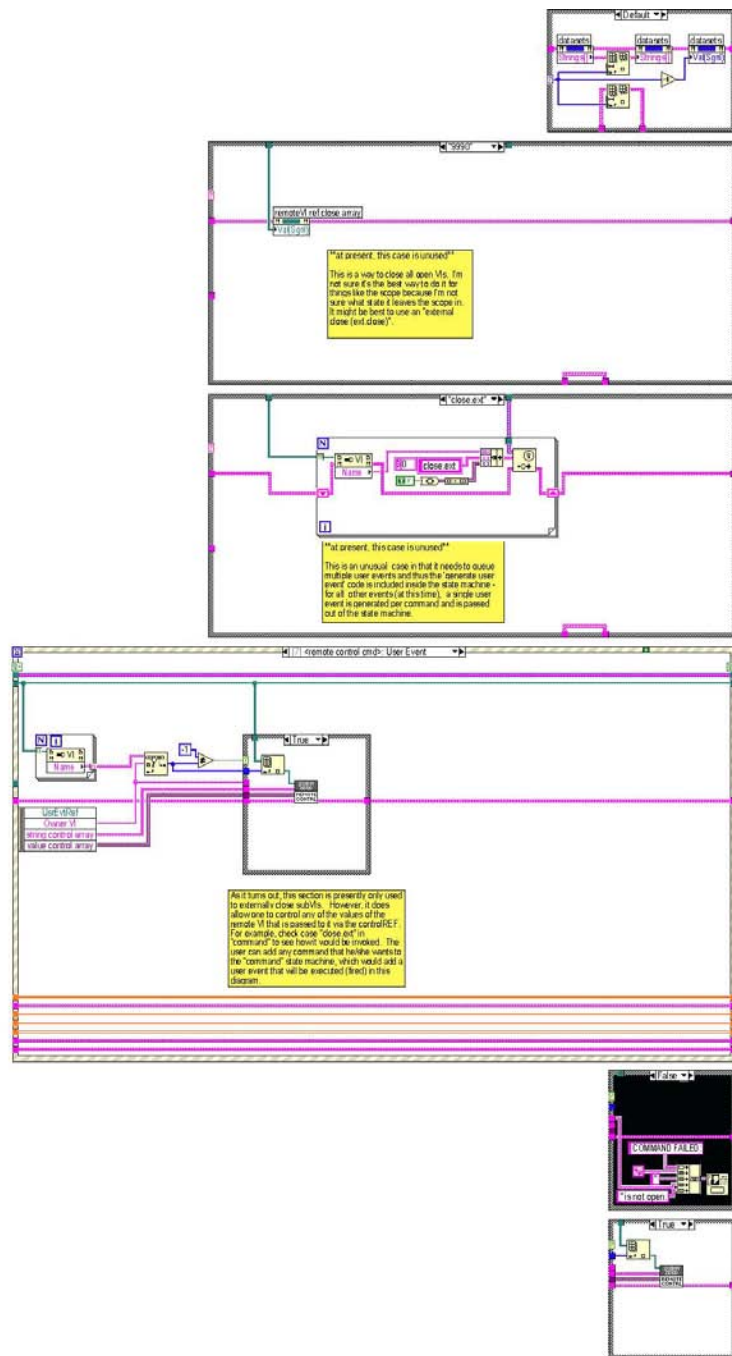
Figure A-10. The "command" event contains a multi-case structure which allows user commands to be executed according to the LABEL value of the control. Shown above is the "store" case.

Figure A-11. The "command" event contains a multi-case structure which allows user commands to be executed according to the LABEL value of the control. Shown above are the "save" and remove" cases.

Figure A-12. The "command" event contains a multi-case structure which allows user commands to be executed according to the LABEL value of the control. Shown above are the "9990" (which is unused) and "close.ext" cases. The <remote control cmd> event is a very powerful event which allows the user to control any values of any remote VI that are passed to it using a "control reference". See the "close.ext" case to see how it is properly invoked.

Figure A-14. The "Run Exp, Stop Exp" is a special event because the Data Acquisition VI requires that all other subVIs are closed prior to and during execution. When the Data Acquisition VI needs to be stopped prematurely, this case properly closes the subVI so that the scope is left in a known state. The "datasets" event is called when a user selects a specific dataset (that has be stored , saved , or just collected). It programmatically fires the "projection" event to directly follow it so that the waveform graph on the front panel is updated with the new dataset.
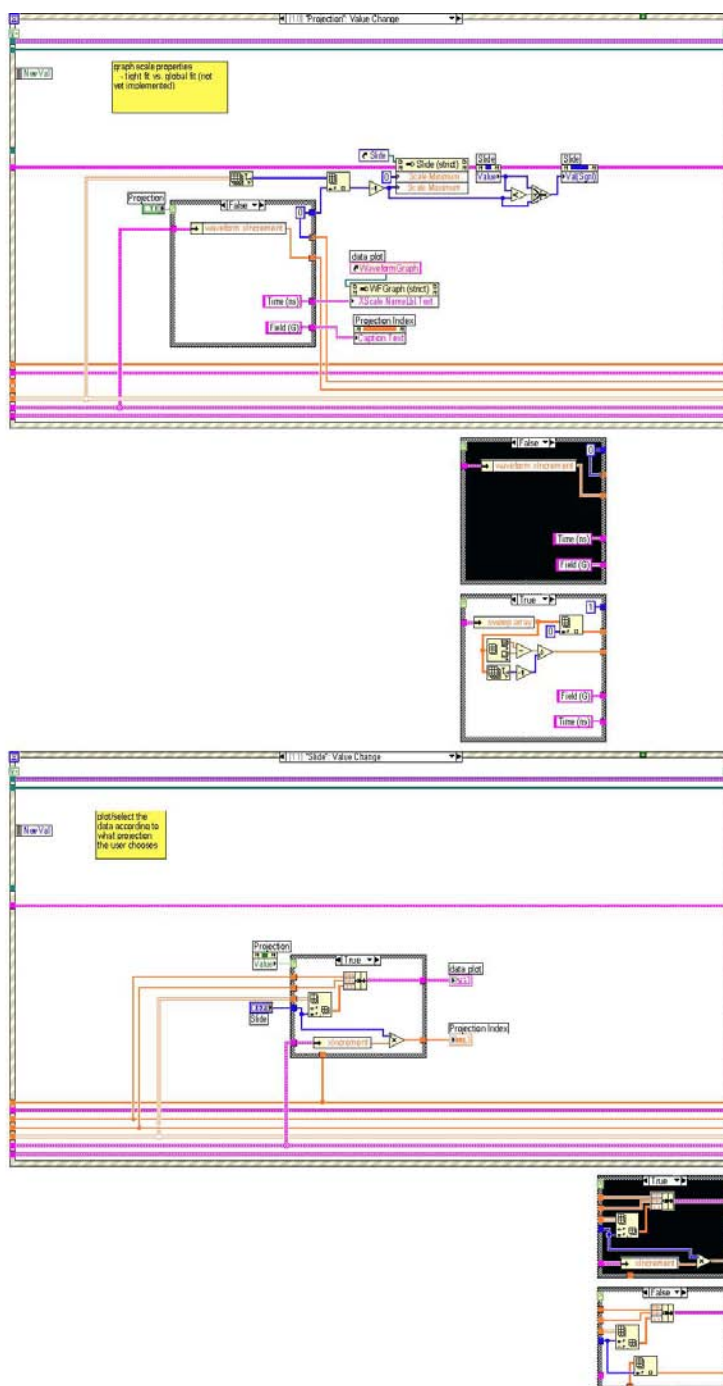
Figure A-15. The "projection" event changes the current projection of the dataset in the waveform graph window, i.e. spectrum or kinetic. The "slide" event selects the appropriate waveform from the 2D dataset and plots either spectral or kinetic based on the value of the 'projection' control.
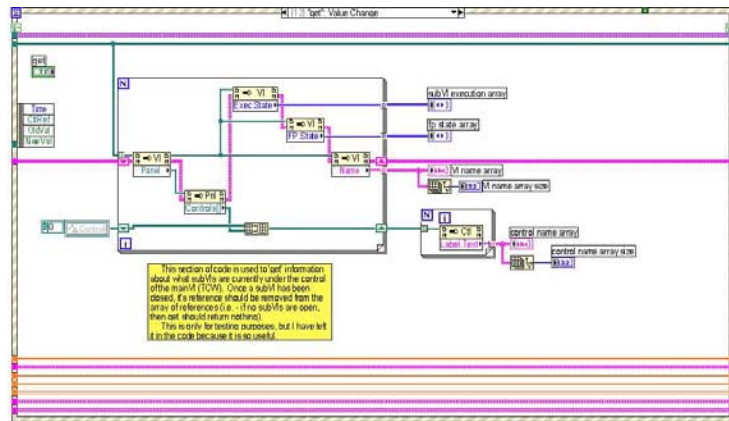
Figure A-16. "Get" value change event. This section of code is used to get information about what subVIs are currently under the control of the main VI. Once a subVI has been closed, it's reference should be removed from the array of references. This section is only for testing purposes but is kept in the code because it is so useful for debugging.

ConfigControls_01.ctl
C:\Documents and Settings\Administrator\Desktop\zexdNI\labview\TCW\scope\ConfigControls_01.ctl

niScope vertical coupling.ctl
D:\programs\NI\LabVIEW 8.0\instr.lib\NISCOPE\Controls\niScope vertical coupling.ctl

niScope trigger coupling.ctl
D:\programs\NI\LabVIEW 8.0\instr.lib\NISCOPE\Controls\niScope trigger coupling.ctl

niScope trigger slope.ctl
D:\programs\NI\LabVIEW 8.0\instr.lib\NISCOPE\Controls\niScope trigger slope.ctl

control_initialize_00.vi
C:\Documents and Settings\Administrator\Desktop\zexdNI\labview\TCW\TCWn\control_initialize_00.vi

initialize_01.vi
C:\Documents and Settings\Administrator\Desktop\zexdNI\labview\TCW\initialize_01.vi

Simple Error Handler.vi
D:\programs\NI\LabVIEW 8.0\vi.lib\Utility\error.llb\Simple Error Handler.vi

ER032M_poll
Instrument I/O Assistant

DialogType.ctl
D:\programs\NI\LabVIEW 8.0\vi.lib\Utility\error.llb\DialogType.ctl

General Error Handler.vi
D:\programs\NI\LabVIEW 8.0\vi.lib\Utility\error.llb\General Error Handler.vi

gen_subVI_control_ref_array_00.vi
C:\Documents and Settings\Administrator\Desktop\zexdNI\labview\TCW\gen_subVI_control_ref_array_00.vi

runsubVI_02.vi
C:\Documents and Settings\Administrator\Desktop\runsubVI_02.vi

Store
Prompt User for Input

save_file_dialog_08.vi
C:\Documents and Settings\Administrator\Desktop\zexdNI\labview\TCW\file\save_file_dialog_08.vi

dynamic_refnum_06.vi
C:\Documents and Settings\Administrator\Desktop\zexdNI\labview\TCW\forums\dynamic_refnum_06.vi

close_ext_00.vi
C:\Documents and Settings\Administrator\Desktop\zexdNI\labview\TCW\TCWn\close_ext_00.vi

BT - size
Build Text

BT - CFSW
Build Text

Figure A-17. List of hard-coded subVIs in TCWn17.

A-4.4 Acquisition Parameters VI - (AcqPrm21n04)

The Acquisition Parameters VI has a very simple purpose. Based on the values in the "Center Feld", "Sweep Width", and "# of points", a 'Sweep Array' variable is generated and returned as an output parameter. That variable defines the field points that will be used when performing the TCW experiment. This VI is intended to be used in conjunction with TCWn17, however the error handling allows it to be used independently without errors. When it is called from TCWn17, it is initialized using a "LV2 style global" variable. The reader is instructed to read the appropriate literature for further explanation.

Figure A-19 through Figure A-21 outline the individual events contained in this VI. The code is very simple, however, take note of the "VI-MON ZEXD" subVI which runs *in parallel* with the single while loop. It is covered in more detail in a later section.
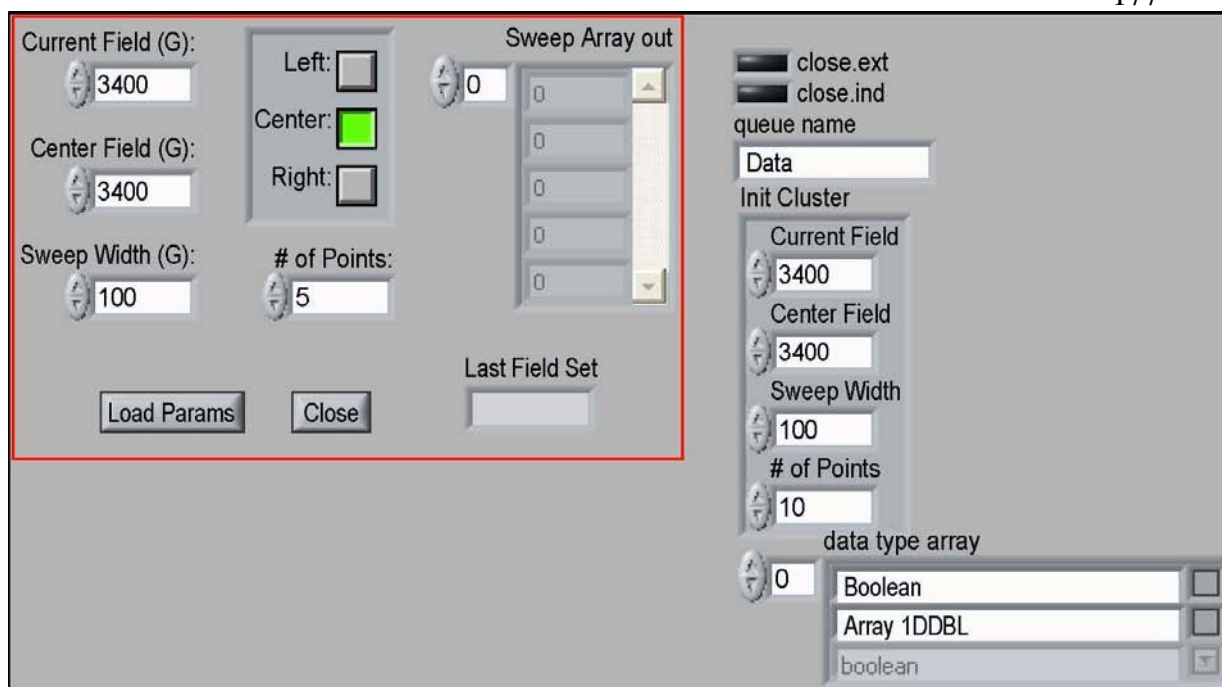
Figure A-18. Front Panel ofAcqPrm21n04. The section enclosed by red in the upper left quadrant is what is actually viewable during execution. "Sweep Array out" defines the field points that will be used when performeing the TCW experiment.
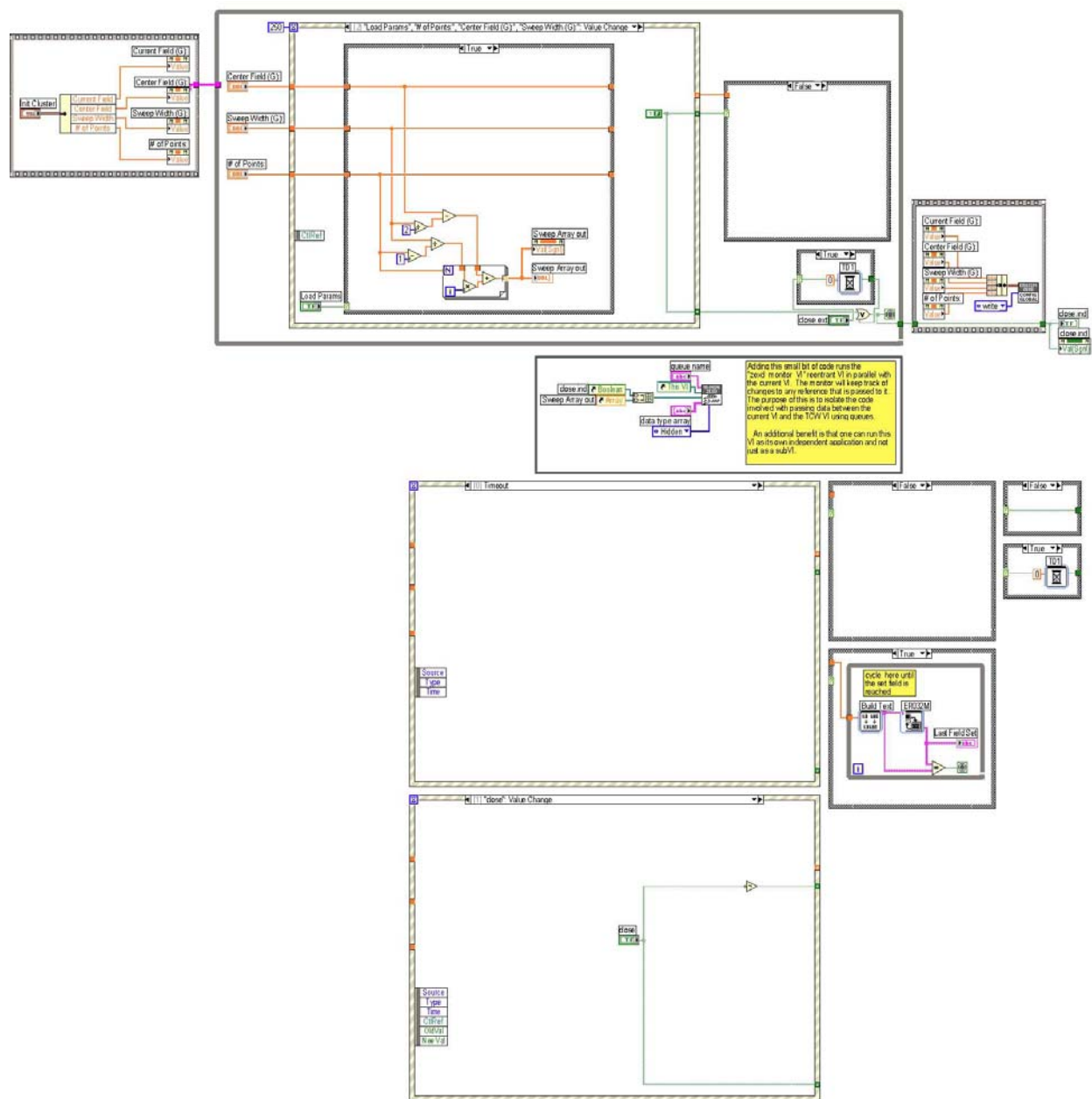
Figure A-19. The while loop contains an event structure which responds to user events. The "VI-MON ZEXD" subVI runs *in parallel* with the single while loop. It is covered in more detail in a later section.
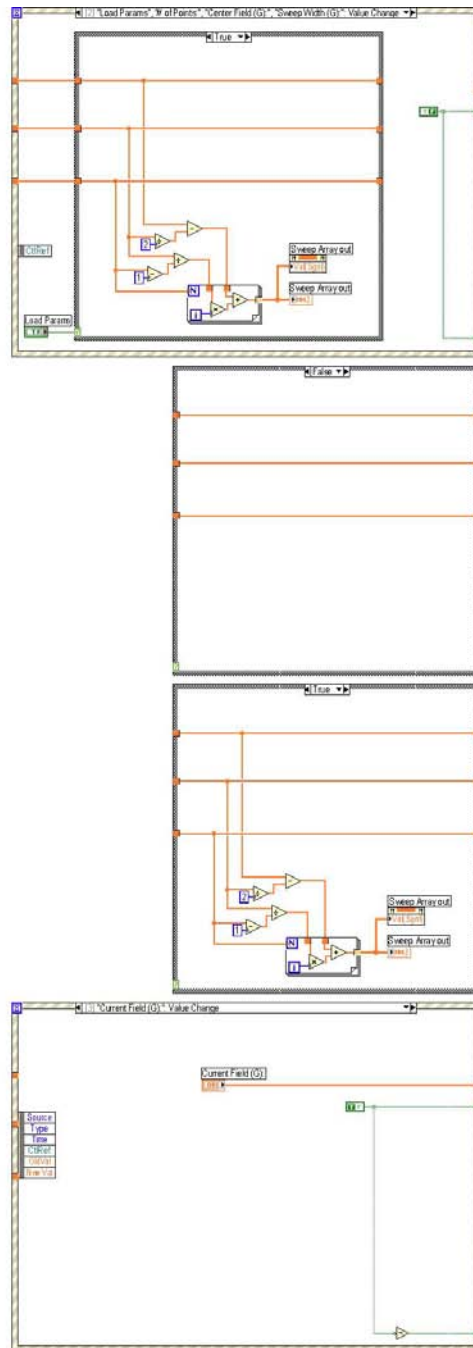
Figure A-20. The "Load Params" event is fired when the user presses the corresponding button on the front panel. This takes the current values and defines the "Sweep Array" variable. The "Current Field (G)" event is used in real-time analysis (such as pre-data acquisition) in order to check the current field value.
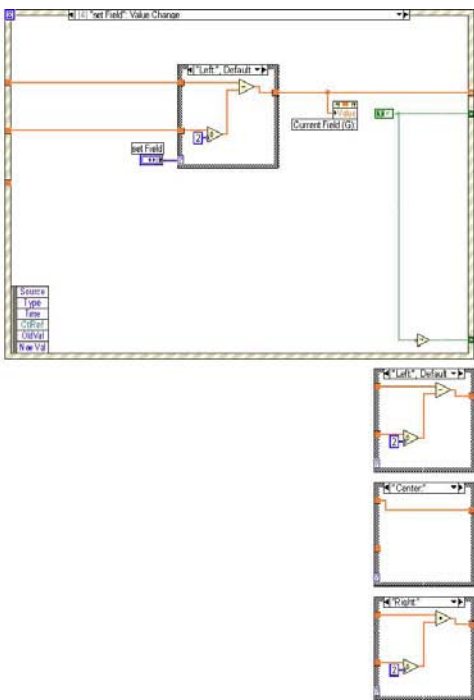
Figure A-21. The "set Field" event is named appropriately. It sets the field (left, right, or center) based on current values on the front panel.

Figure A-22. List of hard-coded subVIs in AcqPrm21n04.

A-4.5 Scope Parameters VI - (niScope EX Configured Acquisition_new_12n02)

In order to reuse as much pre-written code as possible, this VI is based directly off of "*niScope EX Configured Acquisition*" example code which is included with the NI-Scope software. "*This example configures all the digitizer's vertical, horizontal, and triggering properties before every acquisition. It allows you to experiment with numerous configurations, including acquisition types and triggering modes, since it support nearly the entire functionality of NI-SCOPE.*"(http:// zone.ni.com). The reader is directed to the large amount of scope-specific literature provided by LabVIEW which explains this VI as well as all of its subVIs in extreme detail.

The most significant change to the original code is that all of the controls have been collected into a cluster labeled "ScpCfgClstr" (Scope Configuration Cluster), Figure A-24. This allows all of the scope configuration settings to be passed between VIs using a single variable. Obviously, this is important because all of the scope configuration parameters that are set prior to an TCW acquisition are defined in a single variable in this VI.

It is important to be aware that this VI is used strictly as a pre-acquisition, real-time visualization VI. This means that it fairly simple code is all that is required to achieve this purpose. However, the manner in which the actual data is acquired by the Data Acquisition VI is extremely different and will be covered in more detail in the corresponding section.

Take note of the "VI-MON ZEXD" subVI which runs *in parallel* with the single while loop. This VI is covered in more detail in a later section.
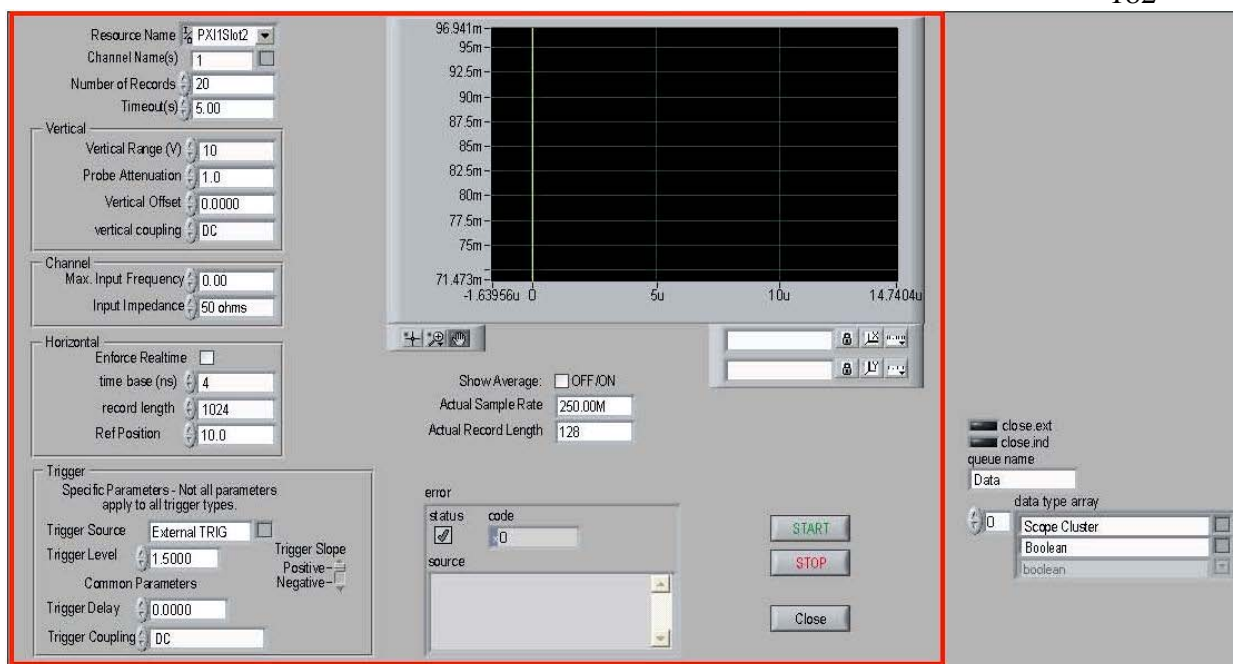
Figure A-23. Front Panel of niScope EX Configured Acquisition_new_12n02. The section enclosed by red is what is actually viewable during execution.
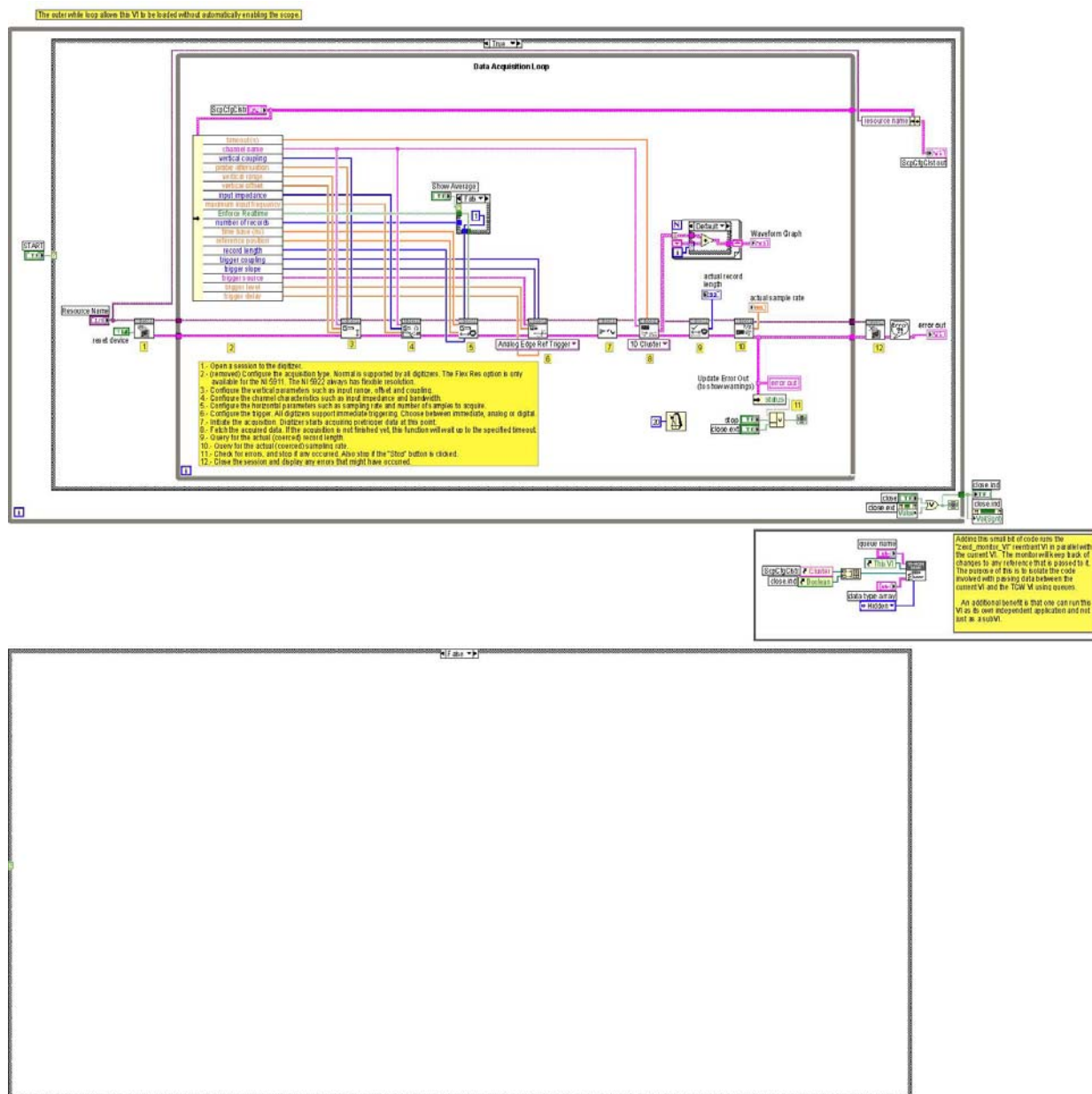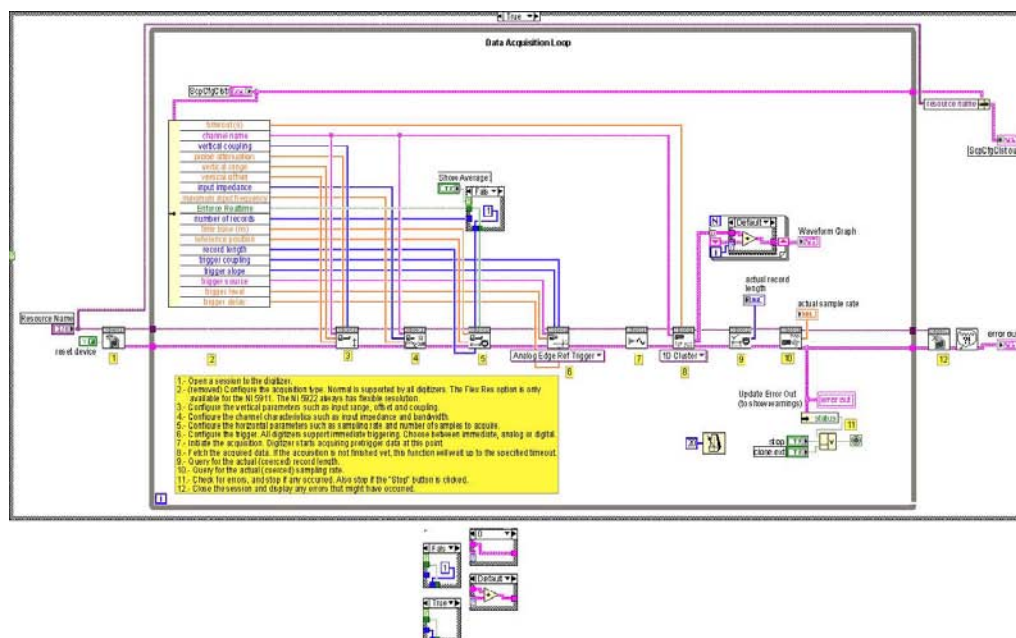
Figure A-24. The outer while loop contains single true/false conditional which starts the real-time acquisition. The leftmost yellow information box describes the role of each numbered portion of the block diagram. The "VI-MON ZEXD" subVI runs *in parallel* with the single while loop. It is covered in more detail in a later section.

Figure A-25. Shown below the outer while loop are the alternate cases used when averaging the waveform for display.

niScope vertical coupling.ctl
D:\programs\NI\LabVIEW 8.0\instr.lib\NISCOPE\Controls\niScope vertical coupling.ctl

niScope trigger coupling.ctl
D:\programs\NI\LabVIEW 8.0\instr.lib\NISCOPE\Controls\niScope trigger coupling.ctl

niScope trigger slope.ctl
D:\programs\NI\LabVIEW 8.0\instr.lib\NISCOPE\Controls\niScope trigger slope.ctl

ConfigControls_00.ctl
C:\Documents and Settings\Administrator\Desktop\zexdNI\labview\TCW\scope\ConfigControls_00.ctl

Data Type Control.ctl
C:\Documents and Settings\Administrator\Desktop\Data Type Control.ctl

niScope Initialize.vi
D:\programs\NI\LabVIEW 8.0\instr.lib\niScope\niScope Initialize.vi

niScope Configure Vertical.vi
D:\programs\NI\LabVIEW 8.0\instr.lib\niScope\Configure\Vertical\niScope Configure Vertical.vi

niScope Close.vi
D:\programs\NI\LabVIEW 8.0\instr.lib\niScope\niScope Close.vi

niScope Configure Chan Characteristics.vi
D:\programs\NI\LabVIEW 8.0\instr.lib\niScope\Configure\Vertical\niScope Configure Chan Characteristics.vi

niScope Configure Horizontal Timing.vi
D:\programs\NI\LabVIEW 8.0\instr.lib\niScope\Configure\Horizontal\niScope Configure Horizontal Timing.vi

niScope Initiate Acquisition.vi
D:\programs\NI\LabVIEW 8.0\instr.lib\niScope\Acquire\Fetch\niScope Initiate Acquisition.vi

Simple Error Handler.vi
D:\programs\NI\LabVIEW 8.0\vi.lib\Utility\error.llb\Simple Error Handler.vi

niScope Fetch (poly).vi
D:\programs\NI\LabVIEW 8.0\instr.lib\niScope\Acquire\Fetch\niScope Fetch (poly).vi

niScope Configure Trigger (poly).vi
D:\programs\NI\LabVIEW 8.0\instr.lib\niScope\Configure\Trigger\niScope Configure Trigger (poly).vi

niScope Sample Rate.vi
D:\programs\NI\LabVIEW 8.0\instr.lib\niScope\Configure\Horizontal\niScope Sample Rate.vi

niScope Actual Record Length.vi
D:\programs\NI\LabVIEW 8.0\instr.lib\NISCOPE\Configure\Horizontal\niScope Actual Record Length.vi

zexdVI Event Monitor_04.vi
C:\Documents and Settings\Administrator\Desktop\zexdVI Event Monitor_04.vi

niScope Configure Trigger Edge.vi
D:\programs\NI\LabVIEW 8.0\instr.lib\niScope\Configure\Trigger\niScope Configure Trigger Edge.vi

niScope Multi Fetch Cluster.vi
D:\programs\NI\LabVIEW 8.0\instr.lib\niScope\Acquire\Fetch\niScope Multi Fetch Cluster.vi

Figure A-26. List of hard-coded subVIs in "niScope EX Configured Acquisition_new_12n02". With the exception of "ConfigControls_00", "Data Type Control", and "zexdVI Event Monitor_04", all subVIs come packaged with the NI-Scope hardware.

A-4.6 Data Acquisition VI - (daq13n01)

This VI is responsible for the actual data acquisition and is conceptually straightforward. When initialized, it is passed the parameters defined in the Acquisition Parameters VI and the Scope Parameters VI and uses them to sweep the magnetic field and collect kinetic traces at each field value.

The design is a classic producer/consumer architecture (http://zone.ni.com/devzone/cda/tut/p/id/3023) with the corresponding while loops appropriately labeled in Figure A-30.

"The Producer/Consumer pattern gives you the ability to easily handle multiple processes at the same time while iterating at individual rates. What makes this pattern unique is its added benefit of buffered communication between application processes. When there are multiple processes running at different speeds, buffered communication between processes is extremely effective. With a large enough communication queue (buffer), the network process will have access to a large amount of the data that the data acquisition loop acquires. This ability to buffer data will minimize data loss.

The Producer/Consumer design consists of parallel loops which are broken down into two categories; producers, and consumers. Communication between producer and consumer loops is done by using data queues. LabVIEW has built in queue functionality in the form of VIs in the function palette. In the Producer/Consumer design pattern, queues can be initialized outside both the producer and consumer loops. Because queues are first-in/first-out, the data will always be analyzed by the consumer in the same order as they were placed into the queue by the producer."

Importantly, this VI uses its own *local queue* (separate from the queue that communicates with TCWn17) which allows communication between the producer and consumer loops. Take note of the "VI-MON ZEXD" subVI which runs *in parallel* with the producer/consumer while loops. This VI is covered in more detail in a later section.

A-4.6.1 Producer Loop

In this VI (Figure A-29), the producer loop steps through the values in the "Sweep Array" variable and collects an averaged transient kinetic (waveform) at each field value. The producer loop waits until the field value is reached (i.e. stable), then initiates a *FETCH* from the scope. The scope initialization and data acquisition is performed by "NISCOPE ZEXD – INIT. ACQ." and "NISCOPE ZEXD – MULTI > RAM", respectively. These two subVIs are based heavily on the "niScope EX Multi Record Fetch More Than Available Memory" VI whose LabVIEW description is:

"This VI demonstrates the multi-record and continuous acquisition capabilities of National Instruments digitizers. In a multi-record acquisition, each record is one waveform with at least "min record length" points as specified with the Configure Horizontal Timing VI. Furthermore, each record is triggered, so when the trigger arrives for the first record, the hardware quickly rearms for the next record. Refer the to Multi Record example for more information.

In this example, the Fetch VI is used with the Fetch Record Number and Fetch Number of Records properties to fetch each record individually. Using the Fetch VI with a positive timeout only waits for the requested waveform to be done - rather than waiting for all the records. In this example, the fetch VI only waits for the next record, and than it retrieves the record while it is acquiring other records.

The Allow More Records Than Memory property is a Boolean value that allows you to configure more records than fit in the onboard memory at one time. When this is enabled, you can specify any number of records. The records are treated circularly in the onboard memory, so you must fetch them before they are overwritten. If you attempt to fetch a record that has been overwritten in the digitizer's memory, an error is returned."

See the NI High Speed Digitizers Help for more information about continuous, multiple-record acquisitions."

This approach was used because it enables the user to collect highly averaged datasets without being concerned about running out of onboard memory. Once that acquisition of an waveform (Figure A-27) is completed, it is enqueued into the local queue to be handled by the consumer loop.
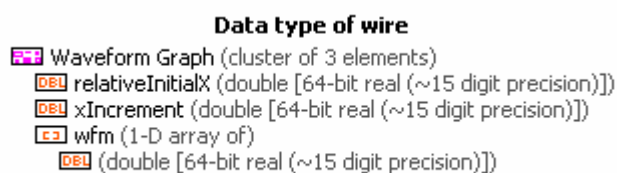
Data type of wire
Waveform Graph (cluster of 3 elements)
  relativeInitialX (double [64-bit real (~15 digit precision)])
  xIncrement (double [64-bit real (~15 digit precision)])
  wfm (1-D array of)
    (double [64-bit real (~15 digit precision)])

Figure A-27. This is the structure/contents of an individual waveform (transient kinetic). It contains the starting point, "relativeInitialX", the "xIncrement", and the 1D array of values, "wfm".

A-4.6.2 Consumer Loop

The consumer loop simply dequeues the individual waveforms (kinetics) and signals the "VI-MON ZEXD" subVI which then enqueues to the data into primary queue that communicates with TCWn17.

A-4.6.3 Final Data Package

After the final waveform (dataset) is collected, the "final data package" cluster is returned to TCWn17. Its contents and structure are shown in Figure A-28. It contains basic information that is used to properly save the data in the Bruker XEpr format.
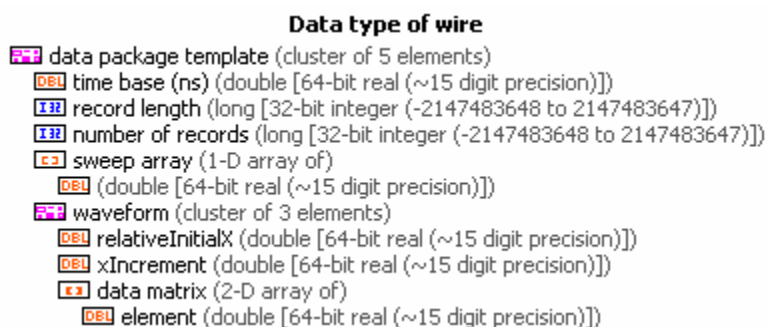
Data type of wire
data package template (cluster of 5 elements)
  time base (ns) (double [64-bit real (~15 digit precision)])
  record length (long [32-bit integer (-2147483648 to 2147483647)])
  number of records (long [32-bit integer (-2147483648 to 2147483647)])
  sweep array (1-D array of)
    (double [64-bit real (~15 digit precision)])
  waveform (cluster of 3 elements)
    relativeInitialX (double [64-bit real (~15 digit precision)])
    xIncrement (double [64-bit real (~15 digit precision)])
    data matrix (2-D array of)
      element (double [64-bit real (~15 digit precision)])

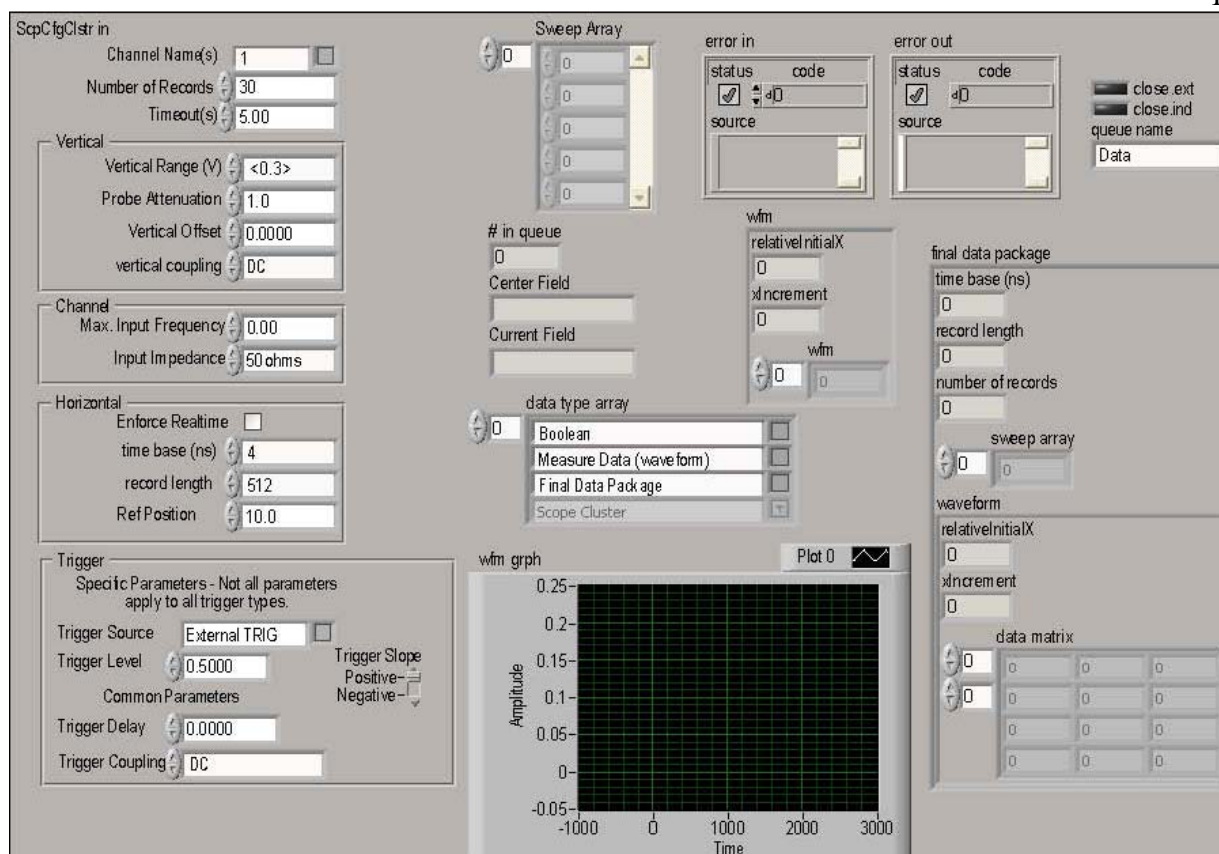**Figure A-28.** "final data package" structure/contents.

Figure A-29. Front Panel of daq13n01. This VI operates in hidden mode, so the user will never see the front panel. However, it is organized in such a way as to facilitate testing if changes are necessary.
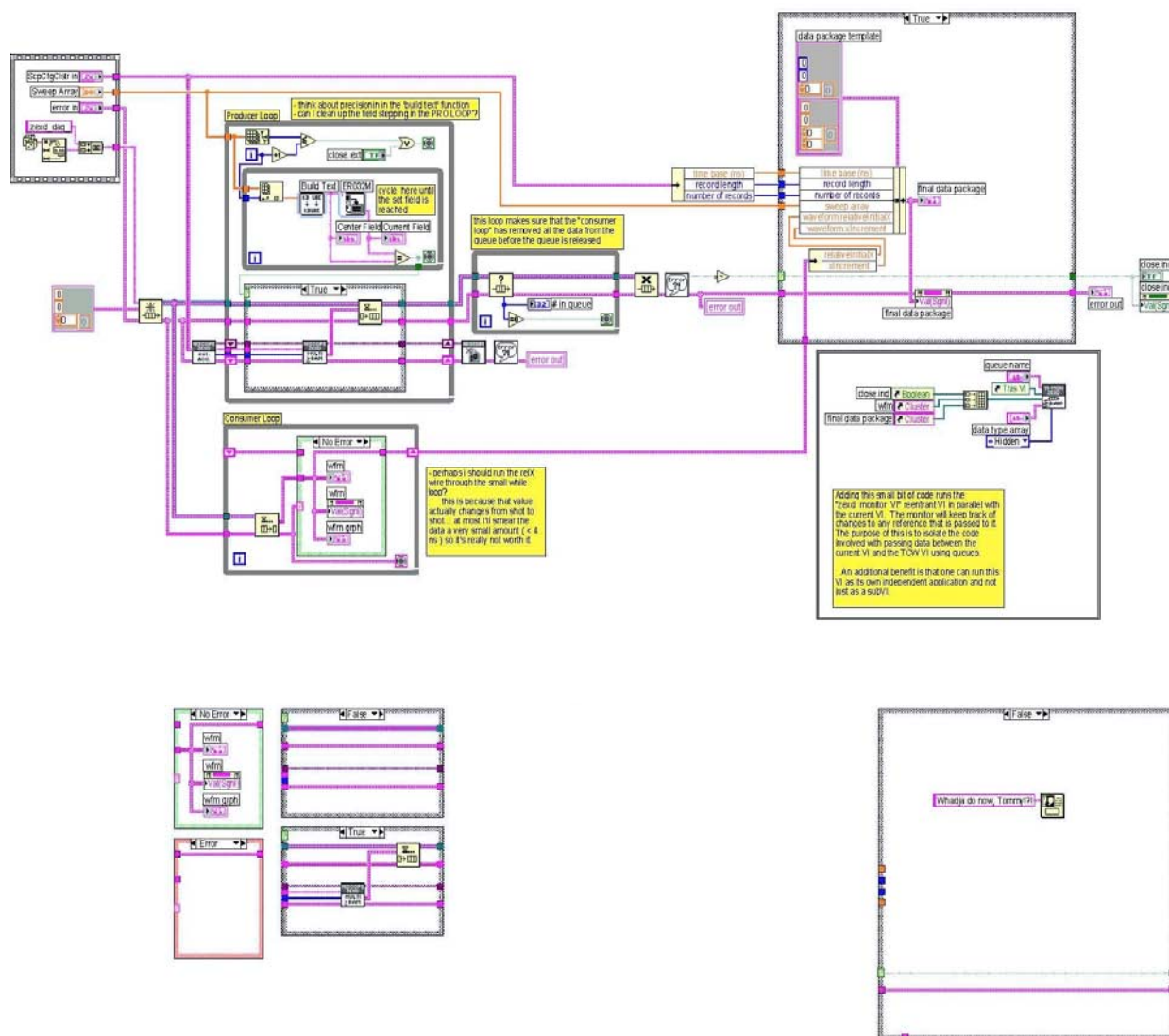
Figure A-30. Block Diagram for daq13n01. It uses a producer/consumer design pattern to collect individual waveforms (kinetics) and then pass them back to TCWn17 using a queue.

niScope vertical coupling.ctl
D:\programs\NI\LabVIEW 8.0\instr.lib\NISCOPE\Controls\niScope vertical coupling.ctl

niScope trigger coupling.ctl
D:\programs\NI\LabVIEW 8.0\instr.lib\NISCOPE\Controls\niScope trigger coupling.ctl

niScope trigger slope.ctl
D:\programs\NI\LabVIEW 8.0\instr.lib\NISCOPE\Controls\niScope trigger slope.ctl

ConfigControls_00.ctl
C:\Documents and Settings\Administrator\Desktop\zexdNI\labview\TCW\scope\ConfigControls_00.ctl

ER032M
Instrument I/O Assistant

Build Text
Build Text

Simple Error Handler.vi
D:\programs\NI\LabVIEW 8.0\vi.lib\Utility\error.llb\Simple Error Handler.vi

zexdVI Event Monitor_04.vi
C:\Documents and Settings\Administrator\Desktop\zexdVI Event Monitor_04.vi

niScope EX Multi Record Fetch More Than Available Memory_new_02_init_04.vi
C:\Documents and Settings\Administrator\Desktop\zexdNI\labview\TCW\scope\niScope EX Multi Record Fetch More Than Available Memory_new_02_init_04.vi

niScope EX Multi Record Fetch More Than Available Memory_new_02_acq_06.vi
C:\Documents and Settings\Administrator\Desktop\zexdNI\labview\TCW\scope\niScope EX Multi Record Fetch More Than Available Memory_new_02_acq_06.vi

niScope Close.vi
D:\programs\NI\LabVIEW 8.0\instr.lib\niScope\niScope Close.vi

Figure A-31. List of hard-coded subVIs in daq13n01.

A-4.7 ZEXD VI Event Monitor VI (zexdVI Event Monitor_04)

It is important to cover this VI because it appears in all subVIs that are opened by TCWn17. Although the minimal code is straightforward (Figure A-34), this VI is deceptively complicated. This VI is designed to run in parallel with all other VIs. It should be placed on the block diagram, and the input terminals, Figure A-32, should be defined accordingly. The monitor will keep track of changes to any reference that is passed to it. The purpose of this VI is to isolate the code involved with passing data between a subVI and the TCW VI using queues (i.e. to unobtrusively mediate data exchange). The alternative is to run wiring for the master queue throughout all subVI block diagrams, which is not a simple task, and generally makes understanding the code quite difficult.

This is a *reentrant* VI which means that multiple instances of the VI can be run *simultaneously*. This is in contrast to all other subVIs which have been covered in this Appendix.

"Under normal circumstances, the execution system cannot run multiple calls to the same subVI simultaneously. If you try to call a subVI that is not reentrant from more than one place, one call runs and the other call waits for the first to finish before running. In reentrant execution, calls to multiple instances of a subVI can execute in parallel with distinct and separate data storage. If the subVI is reentrant, the second call can start before the first call finishes running. In a reentrant VI, each instance of the call maintains its own state of information. Then, the execution system runs the same subVI simultaneously from multiple places."(http://zone.ni.com/reference/en-XX/help/371361B-01/lvconcepts/suggestions_for_exec/)

The input terminals, Figure A-32, include:

1. the master queue name (passed to the subVI from TCWn17)

2. a VI Server reference to the subVI that contains this VI.

3. an array which contains control references to each control which 'zexdVI Event Monitor_04' should be monitoring

4. a corresponding array that defines the type of control that is being monitored (this array must match the order of the control ref. array)

5. the front panel window state for this VI. By default it is hidden (and there is not really any good reason to change that other than testing.

When one of the control references being monitored fires a signal event, the event structure in this VI, Figure A-34, captures the event, and enqueues it into the master queue to be retrieved by TCWn17, Figure A-36.
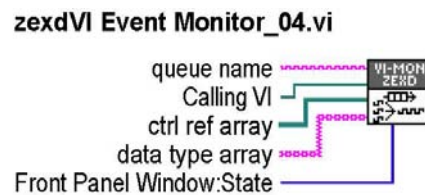

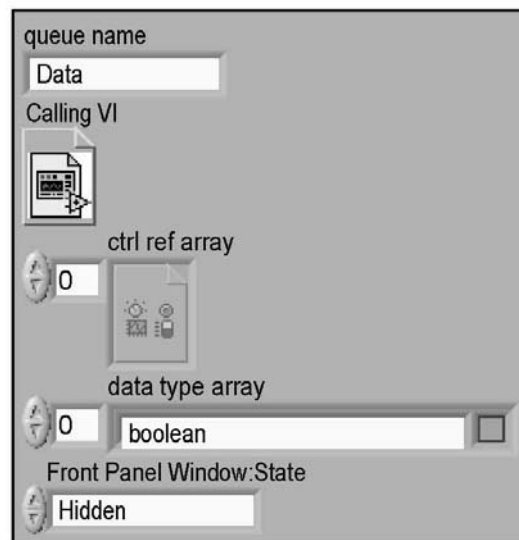**Figure A-32.** Input terminals for "zexdVI Event Monitor_04"

Figure A-33. Front Panel of "zexdVI Event Monitor_04". This VI operates in hidden mode, so the user will never see the front panel. However, it is organized in such a way as to facilitate testing if changes are necessary.
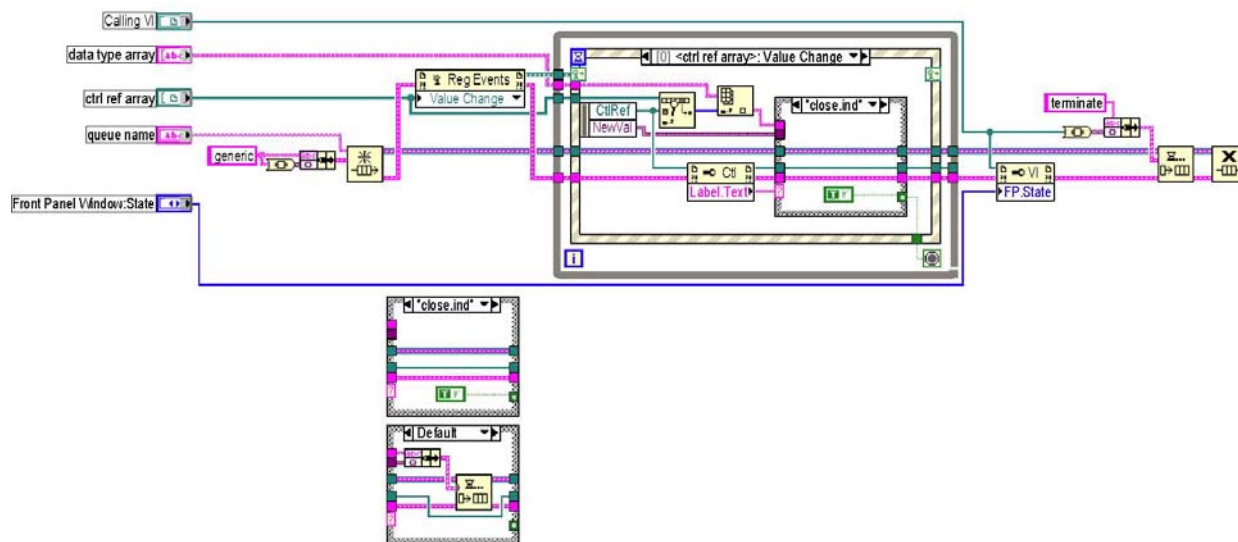
Figure A-34. Block Diagram of "zexdVI Event Monitor_04"

Data Type Control.ctl
C:\Documents and Settings\Administrator\Desktop\Data Type Control.ctl

Figure A-35. List of hard-coded subVIs in "zexdVI Event Monitor_04"

Figure A-36. This diagram describes the interaction between the four primary VIs. The red lines correspond with instrument control, the blue lines correspond with data acquisition, and the green lines correspond with the master queue that allows communication between subVIs and TCWn17. The red and blue channels cannot be run simultaneously

Curriculum Vitae

EDUCATION

Northwestern University, Evanston, IL   Anticipated Graduation: August 2007
- Doctorate of Philosophy Candidate in Chemistry   Cumulative GPA: 3.7/4.00
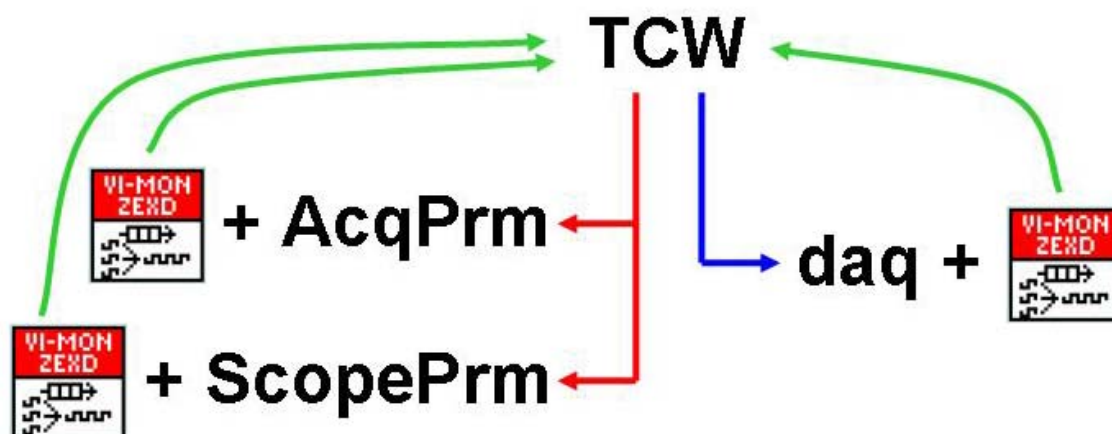- Division of Physical Organic Chemistry
- *Preceptors*: Mark A. Ratner, Ph.D. and Michael R. Wasielewski, Ph.D.

Colorado State University, Ft. Collins, CO   1997-2002
- Bachelor of Science in Chemistry   Cumulative GPA: 3.64/4.00
  - University Honors Scholar
  - American Chemical Society Certified
  - *Preceptor*: Bruce A. Parkinson, Ph.D.
- *Minors*: Mathematics and Music Performance

PROFESSIONAL EXPERIENCE

Northwestern University, Evanston, IL   09/2002-Present
Graduate Research Assistant
- Investigated and modeled charge, spin, and energy transfer dynamics in organic Donor-Bridge-Acceptor systems
- Synthesized organosilane Donor-Bridge-Acceptor molecules for use as Self-Assembled Monolayers
- Assembled new Time-Resolved Electron Paramagnetic Resonance instrument (~$100K) and was responsible for data collection and maintenance on ~$1,000,000 of related equipment
- Developed and programmed computer applications to analyze multi-component datasets, run instrumentation, and control data acquisition
- Collaborated with synthetic organic chemists and directed design of novel organic molecular systems
- Trained and mentored graduate students in data interpretation and instrumentation

Northwestern University, Evanston, IL   09/2002-03/2004
Assistant Course Instructor – Quantum chemistry
Graduate Teaching Assistant – General chemistry
- Taught graduate students essential concepts in basic quantum chemistry
- Instructed undergraduate students in general chemistry concepts and experimental laboratory techniques

Colorado State University, Ft. Collins, CO   2001-04/2002
Undergraduate Research Assistant
- Fabricated perylene tetracarboxylic acid "molecular antenna" thin films on tin oxide and determined that solutions of perylene tetracarboxylic acid systems in dimethylsulfoxide display strong pH dependence using UV-Visible and steady state fluorescence spectroscopy

TECHNICAL SKILLS
- Instrumentation
  - Time resolved electron paramagnetic resonance (TR-EPR) spectroscopy – continuous wave (CW) and Fourier transform (FT) techniques
  - Nanosecond transient absorption spectroscopy, time resolved fluorescence spectroscopy, UV-Visible spectroscopy, steady state fluorescence spectroscopy, magnetic field effect (MFE) experiments
  - X-ray photoelectron spectroscopy (XPS), secondary ion mass spectrometry (SIMS), atomic force microscopy (AFM)
- Analytical Chemistry - Chemometric analysis of multivariate datasets
- Data Analysis Software experience in *MatLab, Labview, Origin, Maple*

- Programming experience in *Labview, MatLab, Java,Origin: LabTalk, Maple, C, C++, Fortran, Visual Basic*
- Computational modeling experience with *GAMESS, Jaguar, Hyperchem, Gaussian, Molden, etc.*

HONORS AND AWARDS RECEIVED
- University Honors Scholar Graduate (2002)
  - successfully completed a selection of interdisciplinary honors seminars and courses in conjunction with major-specific honors courses
- University Eddy Scholar (2001)
  - two students awarded per year for outstanding academic achievement, intellectual curiosity, and breadth of academic pursuits
- Rueben G. Gustavson Senior Chemistry Award (2001)
- Distinguished Scholar Scholarship (1997-2001)
- Creative and Performing Arts Award - Music performance (1998-2001)
- College of Liberal Arts Dean's List (1998)

HONORARY AND PROFESSIONAL AFFILIATIONS
- Phi Beta Kappa Honor Society (2000-present)
- Phi Lambda Upsilon Chemistry Honor Society (2004-present)
- American Chemical Society (2002-present)
- Sigma Xi Scientific Research Honor Society (2001-present)
- Golden Key National Honor Society (1999-present)

PUBLICATIONS
- **Dance, Zachary E. X.**; Mickley, S. M.; Wilson, T. M.; Ahrens, M. J.; Butler, A.; Ratner, M. A..; Wasielewski, M. R. "*Intersystem Crossing Mediated by Photoinduced Intramolecular Charge Transfer in Julolidine-Anthracene Donor-Acceptor Molecules*" (in preparation)
- **Dance, Zachary E. X.**; Ahrens, M. J.; Vega, A. M.; Butler, A.; McCamant, D. W.; Ratner, M. A..; Wasielewski, M. R. "*Direct Observation of the Preference of Hole Transfer over Electron Transfer for Radical Ion Pair Recombination in Donor-Bridge-Acceptor Molecules*" (submitted to JACS)
- **Dance, Zachary E. X.**; Vega, A. M.; Butler, A.; Ahrens, M. J.; McCamant, D. W.; Ratner, M. A..; Wasielewski, M. R. "*Direct Observation of Bridge Mediated Hole Transfer: Time-resolved EPR Studies of Radical Pair Spin Dynamics and Intramolecular Triplet-Triplet Energy Transfer in Donor-Bridge-Acceptor Molecules*" (in preparation)
- **Dance, Zachary E. X.**; Mi, Q.; McCamant, D. W.; Ahrens, M. J.; Ratner, M. A.; Wasielewski, M. R. "*Time-Resolved EPR Studies of Photogenerated Ion Pairs separated by p-Phenylene Oligomers and Triplet States Resulting from Charge Recombination*" (Journal of Physical Chemistry B, **2006**, 110, 25163-73)
- Ahrens, M. J.; Kelly, R. F.; **Dance, Zachary E. X.**; Wasielewski, M. R. *"Photoinduced Charge Separation in Self-Assembled Cofacial Pentamers of Zinc-5,10,15,20-tetrakis(perylenediimide)porphyrin"* (Physical Chemistry Chemical Physics, **2007**, 9, 1469-78)
- Vega, A. M .; **Dance, Zachary E. X.**; Butler, A; Ratner, M. A.; Wasielewski, M. R. *"Development of a High-potential Reductant, Julolidine-Anthracene and Utilization in a Donor-Bridge-Acceptor Series"* (in preparation)

PRESENTATIONS
- **Dance, Zachary E. X.**; Ratner, M. A.; Wasielewski, M. R. *"Time-Resolved EPR studies of charge, Spin, and Energy Transfer in a Series of Donor-Bridge-Acceptor p-Phenylene Oligomers"* American Chemical Society 233rd National Meeting and Exposition, March 2007
- **Dance, Zachary E. X.**; Ratner, M. A.; Wasielewski, M. R. "*Time-Resolved EPR Studies of Photogenerated Ion Pairs separated by p-Phenylene Oligomers and Triplet States Resulting from Charge Recombination*" American Chemical Society 232nd National Meeting and Exposition, September 2006
- **Dance, Zachary E. X.**; Ratner, M. A.; Wasielewski, M. R. "*Effects of Molecular Structure on Charge, Spin, and Energy Transport in p-Phenylene Oligomers*" Gordon Research Conference, August 2006
- **Dance, Zachary E. X.**; Ratner, M. A.; Wasielewski, M. R. "*Self-Assembly of Siloxane-Based Donor-Bridge-Acceptor Systems for Use in Molecular Electronics*" Gordon Research Conference, August 2004

Personal References

- Prof. Mark A. Ratner – Thesis Advisor – Dept. of Chemistry, Northwestern University – (847) 491-5652
  ratner@northwestern.edu
- Prof. Michael R. Wasielewski – Thesis Advisor – Dept. of Chemistry, Northwestern University – (847) 467-1423
  m-wasielewski@northwestern.edu
- Prof. Tamar Seideman – Dept. of Chemistry, Northwestern University – (847) 467-4979
  t-seideman@northwestern.edu